UNIVERSITÉ DE TOURS

Faculté des Sciences & Techniques

ECOLE DOCTORALE EMSTU

N° 552

THESE

présentée pour obtenir le grade de

DOCTEUR D'UNIVERSITÉ

Spécialité : Géosciences

AHMAD AMIN

Master

Dynamique et sédimentation de suspensions liquide-solides

Soutenue publiquement le 27 Juin 2022, devant la commission d'examen :

Madame Florentina Moatar ..... Directeur de Thèse

Madame Laurence Girolami ..... Co-Directeur de Thèse

Monsieur Mohammed Boussafir ..... Président du Jury

Monsieur Renaud Deguen ..... Rapporteur

Monsieur Khalil Abou-Saleh ..... Rapporteur

Madame Sophie Roman ..... Examinateur

Monsieur Frédéric Risso ..... Examinateur

Laboratoire GéHCO

Campus Grandmont

20, Avenue Monge

37200 Tours

Résumé

Dans certains cours d'eau à faible débit moyen, le transfert de sédiments est périodiquement perturbé par l'occurrence d'événements extrêmes (inondations, crues éclair, rupture de digues ou de barrage) au cours desquels l'érosion intense et la mise en suspension de particules solides de taille variable peut entraîner la formation de coulées de débris ou de boue, de concentration variable, qui peuvent se transformer en courants de turbidité ou avalanches sous-marines lorsqu'elles se propagent dans les réservoirs d'eau douce ou en milieu marin profond. Le caractère imprévisible et dévastateur de ces événements empêche bien souvent leur étude directe (à partir de méthodes d'observation ou de surveillance), limitant ainsi la compréhension et la possibilité de modéliser ces phénomènes naturels de grande ampleur. L'objectif de ce travail de thèse consistait tout d'abord à pouvoir générer en laboratoire des suspensions homogènes de particules solides et de liquide, tout en étant capable de caractériser proprement la concentration en sédiments du mélange et de pouvoir la faire varier sur une large gamme de valeurs.

Dans un premier temps, des expériences classiques de fluidisation et de sédimentation impliquant différents types de matériaux (de taille, de densité, et de forme variable) et de fluide (liquide ou gaz) ont été réalisées dans le réservoir du dispositif. Les mesures obtenues nous ont permis de montrer que la vitesse moyenne de sédimentation des particules dans une suspension homogène peut être obtenue à partir de la vitesse théorique d'une particule isolée se déposant dans un fluide pur au repos, à laquelle on doit appliquer deux corrections : une sur la densité qui affecte la force de flottabilité agissant sur la particule et une autre sur la viscosité qui affecte à la fois la force de trainée agissant sur la particule et son agitation locale par rapport à celle du fluide. Des expériences supplémentaires consistant à relâcher une sphère macroscopique, de taille variable, dans ces suspensions, nous ont permis de comprendre que la force de trainée agissant sur la sphère plongeante est attribuée à une fine couche de mélange, coincée entre la paroi de la sphère et la particule la plus proche, fortement cisaillée, et caractérisée par la viscosité locale du mélange telle

que l'on peut la décrire à partir de la vitesse de sédimentation. Au-delà de cette couche, les particules de la suspension glissent par rapport à la sphère.

En relâchant ces suspensions dans le canal du dispositif expérimental, de type 'rupture de barrage', nous avons pu réaliser des expériences inédites de coulées de boue (écoulements à surface libre générés dans le canal rempli d'air) et de courants de turbidité (écoulements pleinement immergés réalisés dans le canal rempli d'eau) afin de mieux comprendre les processus de transport et de sédimentation des particules dans ces écoulements. Les résultats obtenus nous ont permis de montrer que la concentration en particules dans le mélange tend à diminuer sa mobilité (distance et temps de parcours, vitesse moyenne). Le dépôt laissé par les écoulements sont également d'autant plus épais et plus court que la concentration en particules dans le mélange est élevée, ce qui peut s'expliquer notamment par une sédimentation plus rapide des particules. Le temps de runout de la suspension est contrôlé par le temps de sédimentation décrit à partir d'une longueur de sédimentation caractéristique et la vitesse de sédimentation déterminée précédemment qui dépend uniquement des propriétés de la suspension, des matériaux et du fluide. Les écoulements immergés se distinguent des écoulements à surface libre par la formation d'une couche de mélange diluée formée en surface qui devient rapidement indépendante de l'écoulement sous-jacent. Son temps de propagation est contrôlé par le temps de chute des particules dans le fluide au repos.

Abstract

In some rivers characterized by a low mean flow rate, the sediments transfer is periodically disturbed by the occurrence of extreme events (floods, flash floods, dyke breaches or dam-break) during which the intense erosion of solid particles of variable size can lead to the formation of debris and mud flows, of various concentration, that can transform into turbidity currents or submarine avalanches as they propagate through freshwater reservoirs or deep-sea environments. The unpredictable and devastating nature of these events commonly prevents their direct study (through observation or monitoring methods), thus limiting the understanding and the possibility of modeling these large-scale natural phenomena. The objective of this PhD work first consisted in generating homogeneous suspensions of solid particles and liquid in the laboratory, while being able to properly characterize the concentration of sediments in the mixture and varying it on a wide range of values.

First, classical fluidization and sedimentation experiments involving different types of materials (of varying size, density, and shape) and fluid (liquid or gas) have been performed in the reservoir of the experimental device. The measurements obtained allowed us to highlight that the mean sedimentation velocity of the particles in a homogeneous suspension can be obtained from the theoretical expression of the velocity of an isolated particle settling in a pure fluid at rest, to which two corrections are applied : a first-one on the density that affects the buoyant force acting on the particle ; a second-one on the viscosity that affects both the drag force acting on the particle and its local agitation relatively to that of the fluid. Additional experiments consisting in releasing a macroscopic sphere, of variable size, in these suspensions, allowed us to highlight that the drag force acting on the falling sphere is attributed to a thin layer of mixture, strongly sheared, wedged between the sphere wall and the closest particle and characterized by the local mixture viscosity as previously described from the sedimentation velocity. Beyond this layer, the particles of the suspension slide relatively to the sphere.

By releasing such homogeneous suspensions in the dam-break flume, we performed novel experiments of mud flows (e.g. free-surface flows generated in the flume filled with air) and turbidity currents (e.g. fully immersed flows performed in the flume filled with water) in order to better understand the processes of transport and sedimentation of the particles within the flows. The results obtained allowed us to highlight that the concentration of particles in the mixture tends to reduce its mobility (distance and travel time, mean velocity). The deposit left by the flows is also thicker and shorter as the concentration of particles in the mixture is increased, which can be explained in particular by their faster sedimentation. The runout time of the suspension is controled by the sedimentation time described from a characteristic sedimentation length and the sedimentation velocity determined previously that only depends on the suspension, materials, and fluid properties. Immersed flows differ from the free surface ones by the formation of a dilute mixture layer formed at the surface of the suspension which rapidly becomes independent of the underlying flow. Its propagation time is controled by the time taken by a particle to fall in the pure fluid at rest.

Table des matières

Table des figures

Liste des tableaux

Introduction générale.

Le risque d'inondations et d'événements catastrophiques pouvant survenir dans les rivières aménagées représente à l'heure actuelle l'une des catastrophes naturelles les plus préoccupantes de France métropolitaine (Charlot et al., 1995). Au-delà des répercussions morphologiques majeures observées en tête de bassin versant ou à proximité des ouvrages fragilisés (débordement, érosion des berges et du fond de la rivière), le passage d'une onde de crue peut provoquer une érosion intense de sédiments à l'origine de coulées de débris ou de boue fortement dévastatrices qui peuvent se propager sous forme de courants de turbidité dans les réservoirs d'eau douce ou jusque dans les milieux marins profonds. En France, le dernier exemple le plus marquant est celui de la tempête Alex, survenu le 2 octobre 2020, au cours duquel les épisodes de crues, initiés à la suite de pluies torrentielles, ont entraîné la formation de coulées de débris et de boues qui se sont propagées dans les vallées de la Vésubie et de la Roya (Alpes-Maritimes) emportant la plupart des aménagements (routes, ponts, logements) situés sur leur passage (Figure 1). Plusieurs milliers de mètres cube de sédiments ont été transportés sur plusieurs dizaines de kilomètres sur terre ou en mer provoquant la mort d'une dizaine de personnes et un bilan économique (associé à la reconstruction des ouvrages) de l'ordre du milliard d'euros. Quelques dizaines d'années auparavant, c'est la rupture du barrage de Malpasset, survenue le 2 Décembre 1959 après plusieurs épisodes de pluies diluviennes, qui était à l'origine d'une onde de crue de 50 m de haut se propageant à environ 70 $km.h^{-1}$, dans la gorge du Reyran, où aucun système d'alerte n'avait été mis en place pour prévenir les populations de Fréjus et autres villages situés en aval, en cas de risque d'inondation. Après avoir rapidement atteint le chantier de construction du pont de l'autoroute situé à proximité, l'onde de crue fortement érosive s'était progressivement transformée en coulée de boue d'une dizaine de mètres d'épaisseur. À Fréjus, la coulée avait alors détruit de nombreuses infrastructures (immeubles, routes, ponts) et terminé sa course sur la base aéronavale, emportant plusieurs dizaines d'appareils, avant de se jeter en mer Méditerranée. Ces coulées de boue avaient alors sinistré plus de 1350 hectars d'espaces agricoles, détruit plus de 150 immeubles, et surtout coûté la vie à 413 personnes (Figure 1).

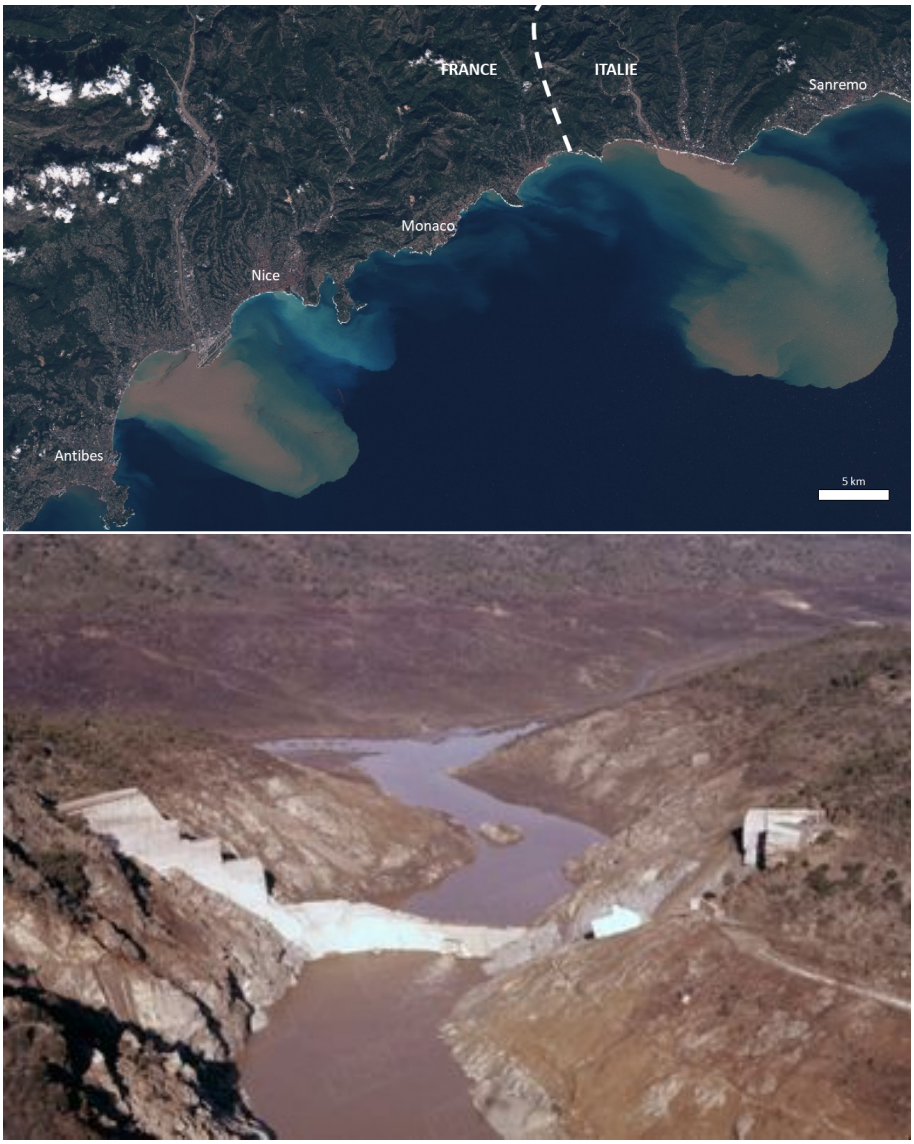

Figure 1

En haut : image satellite réalisée le 3 Octobre 2020 sur laquelle on peut observer les courants de turbidité formés dans la Baie des Anges (au large de Nice) à la suite de la tempête Alex. En bas : rupture du barrage Malpasset à Fréjus survenu le 2 Décembre 1959.

Cependant, le danger présent autour de ces épisodes catastrophiques empêche bien souvent leur étude directe (à partir d'enregistrements vidéo ou de méthodes d'observation basées sur un système d'instrumentation), ce qui limite la compréhension et la possibilité

de modéliser convenablement ces phénomènes de grande ampleur, ainsi que leur mode de mise en place. Il est alors important de reproduire ces processus en laboratoire afin d'accéder à la physique de ces écoulements pour mieux appréhender ces phénomènes naturels. Ce travail de thèse a été mis en place dans cet objectif. Il s'agissait d'une part de pouvoir générer des suspensions de particules (réalisées avec des matériaux synthétiques et naturels) dont on peut caractériser la concentration et la faire varier sur une large gamme de valeurs ; et d'autre part de décrire et analyser l'influence de ce paramètre sur leur capacité de transport et de sédimentation. Dans la littérature, la plupart des modèles développés dans le cadre d'applications géophysiques (situées à l'échelle du tronçon de rivière ou à celle du bassin versant) prennent en compte un grand nombre de variables (débit liquide, débit de particules en suspension, débit de particules charriées, frottement exercé à la base, épaisseur du dépôt, hauteur d'eau, concentration en sédiments ; Rahuel et al., 1989 ; Holly and Rahuel, 1990 ; Holly et al., 1993 ; Singh et al., 2004), ce qui ne permet pas d'identifier les ingrédients nécessaires à la compréhension des mécanismes physiques mis en jeu dans ces écoulements. C'est pourquoi, il est important de développer en parallèle des modèles simplifiés qui permettent d'identifier ces paramètres et de décrire en détail leur influence sur la dynamique du système.

Notre approche consiste alors à étudier la fluidisation/sédimentation et viscosité de suspensions liquide-solides (à concentration variable) à travers deux études préliminaires réalisées dans un réservoir ; puis d'en étudier la dynamique de transport et de mise en place à travers deux études réalisées en canal. Sur le plan de la physique, la plupart des études menées à l'heure actuelle concerne la rhéologie de suspensions non browniennes cisaillées, généralement réalisées avec des particules de mêmes densité que celle du liquide (Guazzelli & Pouliquen ; 2018 et références associées) mais ne traite pas le cas des suspensions non cisaillées (statiques ou en écoulement) dominées par les processus de sédimentation. L'une des spécificités de ce travail est alors d'importer les techniques de fluidisation, communément utilisées dans l'industrie pour générer des lits fluidisés gaz-solides, pour reproduire ici des suspensions liquide-solides pouvant être décrites comme

des mélanges homogènes à concentration variable. Ces processus de fluidisation sont très bien connus dans les communautés d'ingénierie dans lesquelles ils sont fréquemment utilisés pour l'optimisation des procédés agro-alimentaires, pharmaceutiques, métallurgiques, pétroliers, ou encore nucléaires.

Les expériences présentées dans ce manuscrit ont été réalisées dans un dispositif de type 'rupture de barrage', c'est-à-dire doté d'un réservoir hermétique et d'un canal imperméable en PMMA conçus et construits au préalable. L'utilisation de matériaux synthétiques (billes de verre de différentes tailles et billes de PMMA de différente densité), caractérisés par de fortes capacités d'expansion et comparés à des matériaux naturels (sable fin caractérisé par une distribution granulométrique plus étendue et une forme de particules aléatoire) nous ont permis de reproduire des suspensions homogènes dans tout le régime de Stokes. Ces suspensions ont ensuite été relâchées dans un canal horizontal, sur fond lisse et imperméable, afin d'en étudier la dynamique de transport et de sédimentation. La structure de cette thèse est définie de la manière suivante :

- Le chapitre 1 présente le dispositif expérimental et les matériaux utilisés. Il décrit les processus de fluidisation (ainsi que les différents régimes existants) et la façon dont on procède pour générer les suspensions. Enfin, il présente les expériences réalisées en canal et les méthodes de visualisation utilisées.

- Le chapitre 2 présente des expériences classiques de fluidisation et de sédimentation, réalisées avec différents types de matériaux et de fluides, qui nous ont permis d'établir une loi universelle valable dans le régime de fluidisation stable et homogène lorsque l'inertie du fluide est négligeable.

- Le chapitre 3 présente des expériences simplifiées de chute de sphères macroscopiques dans ces différentes suspensions et nous permettent d'exprimer la contrainte cisaillante exercée sur la sphère.

- Le chapitre 4 présente des expériences inédites de coulées de boues réalisées

en canal et décrit en détail les mesures réalisées et les résultats obtenus.

• Le chapitre 5 présente des expériences originales de courants de turbidité réalisées en canal et décrit de la même manière les mesures réalisées et les résultats obtenus.

• La conclusion générale résume dans les grandes lignes le fil conducteur du travail réalisé ainsi que les résultats majeurs obtenus et présentés à travers les différents chapitres.

Bibliographie

Charlot, F., B. Falourd, N. Vivier, T. Xouillot (1995) Historique des protections contre les crues de la Loire, Rapport de la Direction Régionale de l'Environnement, de l'Aménagement et du Logement, Section Orléans-Angers.

Guazzelli E., O. Pouliquen (2018) Rheology of dense granular suspensions, J. Fluid Mech. 852, 35.

Holly F. M. and J.L. Rahuel (1990a) New numerical physical framework for mobile-bed modelling, Part I : numerical and physical principles, J. Hydraulic Res., 28(4), 401-416.

Holly, F.M., J.C. Yang, P. Schwarz, J. Schaefer, S.H. Hsu and R. Einhellig (1993) Numerical Simulation of Unsteady Water and Sediment Movement in Multiply Connected Networks of Mobile-Bed Channels, IIHR Report, 43, Iowa Institute of Hydraulic Research, The University of Iowa, United-States.

Malavoi J.R., C.C. Garnier, N. Landon, A. Recking and P. Baran (2007) Eléments de connaissance pour la gestion du transport solide en rivière, Rapport de l'ONEMA.

Rahuel J.L., F.M. Holly, J.P. Chollet, P. Belludy and G. Yang (1989) Modelling of river bed evolution for bed load Sediment mixtures, J. Hydraulic Res., 115(11), 1521-1542.

Singh A.K., U.C. Kothyari and K.G. Ranga Raju (2004) Rapidly varying transient flows in alluvial rivers, J. Hydraulic Res., 42(5), 473-486.

Chapitre 1

Experimental procedures

1.1 Experimental device

The experimental device (Figure 1.1), used in this study, consists in a rectangular dam-break flume that includes two main parts :

- a fluidization rig in which the particulate suspensions are generated ;
- a rectangular flume in which the suspensions are released and travel until running out of mass.

These two parts are separated by a sliding gate that is controled by a hydraulic cylinder supplied by an air compressor. Such a system can ensure a lock-exchange reservoir, with no leakage of water during the fluidization step, as well as a rapid aperture of the gate, at constant velocity, during the release step.

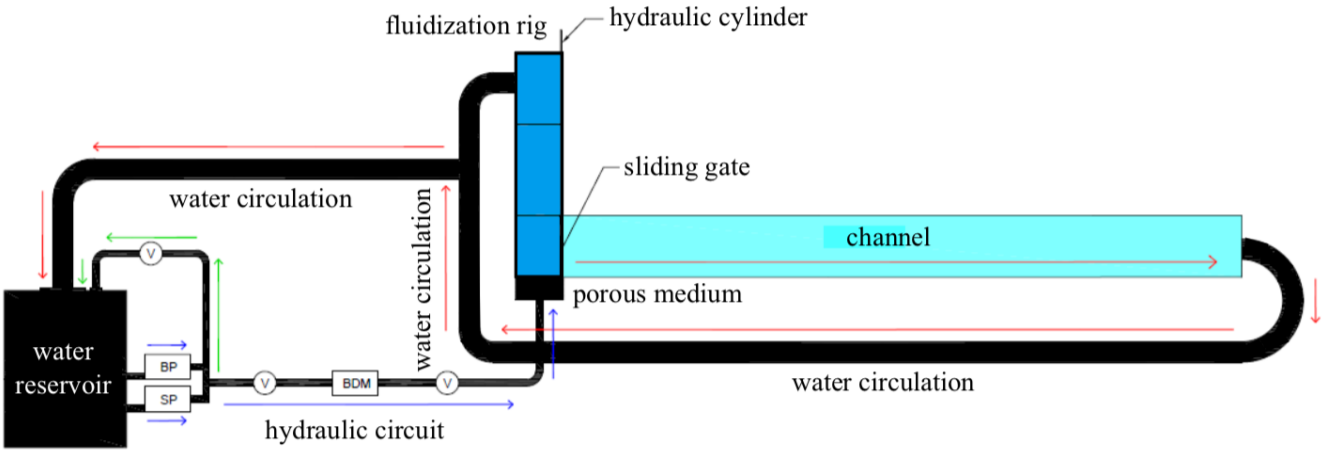

Figure 1.1

Scheme of the experimental device used in this study.

The construction of this flume (Figure 1.1) was made in order to reproduce both free-surface flows and immersed flows (depending on the boundary conditions) that can be observed through the transparent side-walls.

The fluidization rig is supplied by water in aid of an external tank that enables

the storage of a large volume of water, while its injection is ensured by two centrifugal pumps connected in parallel and used independently of each other. The first pump ensures the water injection, through small flow rates, typically ranged between 0 and $12L.min^{-1}$, whilst the second one ensures the injection of higher flow rates, ranged from $12L.min^{-1}$ to $32L.min^{-1}$. Before measurements, the flow rate is stabilized thanks to a discharge circuit that pours the excess of water into the external tank. The discharge flow rate is controled by a valve, that can simultaneously regulate both the injected and the discharge flow rates. After passing the pumps, the injected water passes through a magnetic flowmeter (which gives measurements with an accuracy of $0.01L.min^{-1}$), before being injected through the porous medium located at the base of the fluidization rig. This porous medium, represented in Figure 1.2, is made with a first layer of straws ; overlyed by a second thicker layer made with a superposition of gravels, glass beads, and stainless steel beads ; and overlyed by a third layer of moss.

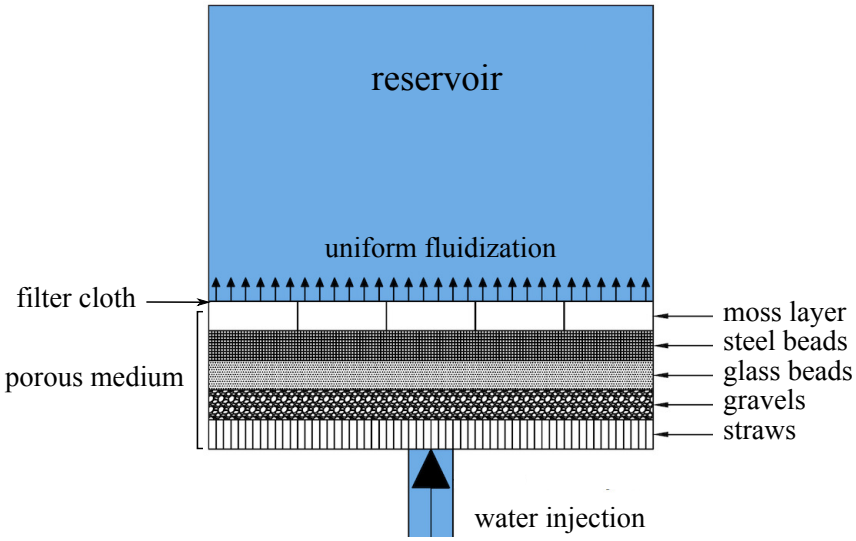

Figure 1.2

Scheme of the porous medium located at the base of the fluidization rig.

This compartment aims at tranquilizing the flow in order to provide a homogeneous fluidization of the particles located in the above reservoir. In order to prevent any mixing

or mass exchanges between the sediments and the porous medium, a stainless steel filter cloth, characterized by a mesh with pores size of $125\mu m$, allows to ensure the separation of the two compartments. Once poured in the principal reservoir, the particles are uniformly fluidized under controled conditions and expanded at a given rate. When the fluidization is stabilized, *e.g.* when the given solid volume fraction is reached, the aperture of the sliding gate is made thanks to a hydraulic cylinder and simultaneously to the stop of fluidization. Furthermore, in order to not disturb the collapse of the suspension, the speed of the sliding gate opening requires to be greater than $\sim 2m.s^{-1}$.

In this thesis, two principal types of studies have been performed :

- (1) The sedimentation behavior of the suspensions. Once the material is fully fluidized and the mixture forms a homogeneous suspension characterized by a given expansion rate, the water supply is stopped in order to study the sedimentation behavior of suspensions of various concentrations.

- (2) The dynamics behavior of the suspensions. Once the material is fully fluidized and the mixture forms a homogeneous suspension characterized by a given expansion rate, the water supply is stopped simultaneously to the sliding gate aperture in order to study the propagation and the dynamics of such sedimenting suspensions. At the end of these experiments, the morphology of the deposits let by the flows are measured precisely (every $5cm$).

1.2 Fluidization concepts

The fluidization processes, that are largely developed in both natural flows and industrial processes, can be easily reproduced in the laboratory by injecting uniformly a vertical fluid stream (passing through a porous plate or a porous medium) at the base of a static bed of particles.

When the fluid velocity U_f is weak, the fluid passes through the interstitial voids let

by the particles, without modifying the state of the bed, as in a porous medium. In this state, the bed remains static (without expansion), whilst the pressure drop ΔP across it increases linearly with U_f since the drag exerted on particles is dominated by viscous stresses that are proportional to the fluid flow, as exposed in Figure 1.3 (Girolami & Risso, 2018). If the fluid stream is increased further, the velocity of minimum fluidization, termed U_{mf}, is reached. At this point, the driving forces counterbalance the gravitational ones such as the total weight of particles is entirely supported by the fluid flow such that the mixture forms a uniform suspension whose friction is significantly reduced and which may be easily sheared and superficially behaves as a fluid (Eames & Gilbertson, 2000). If particles are fine and light enough, the mixture expands uniformly with U_f such as the bed height increases linearly whilst the pressure drop becomes independant of the fluid flow (Figure 1.3).

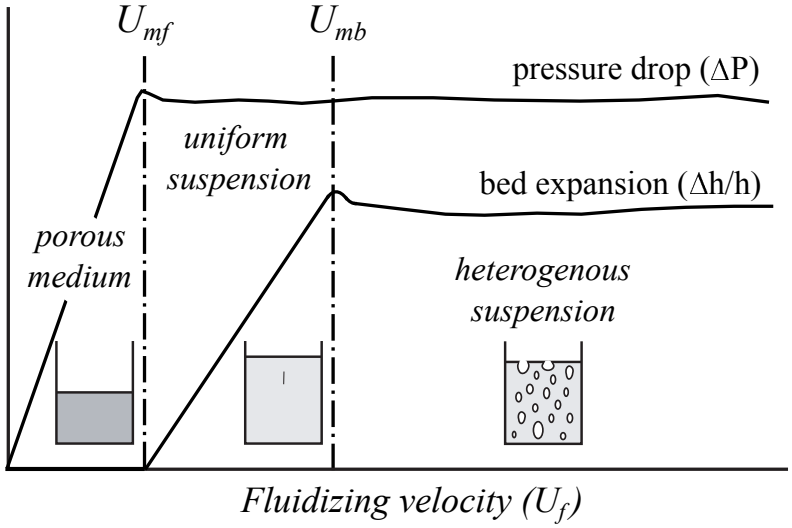

Figure 1.3

Pressure drop ΔP across the bed and mixture expansion $\Delta h/h$ as a function of the fluidizing velocity U_f.

This state is observed until a second critical velocity (termed velocity of minimum bubbling, U_{mb}) above which cavities or heterogeneities develop in the mixture and coalesce

as they rise, thus disturbing the fluidization and making it unstable, associated with a vigorous mixing and turbulence. In this state, the bed expansion remains approximately constant and closed to its maximum value. Above this point, the bed height as well as the pressure drop across the bed are independent of the fluid stream (Figure 1.3). However, these different regimes of fluidization depend on the type of material used and on the conditions of operation. For example, with coarse and/ or dense materials, the uniform (particulate) regime of fluidization (usually developed between U_{mf} and U_{mb} with fine powders) is not observed such that the bubbling regime directly follows the packing state. Otherwise, when the material is fine and dominated by cohesive forces at room temperature, the fluidization is impeded since the fluid solely flows through channels developed within the most permeable regions of the bed such as the bed weight can not be fully supported and the bed expansion remains quasi-inexistent (Girolami & Risso, 2018).

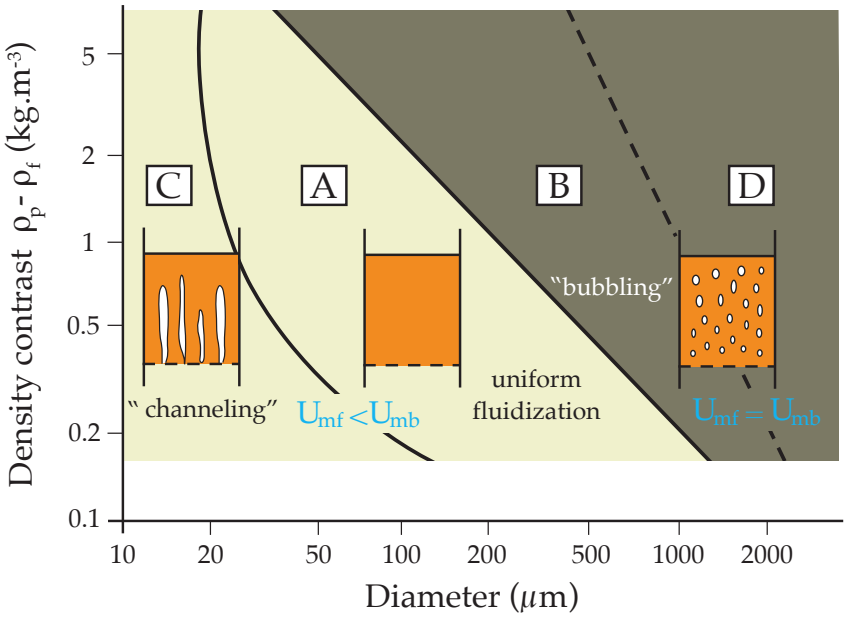

Figure 1.4

Classification of Geldart (1973) distinguishing the fluidization behavior of fluid-solid systems subjected to ambient conditions (extracted from Girolami, 2008).

Geldart (1973) proposed an empirical classification to distinguish the different types of fluidization behavior according to the grain size and the density difference between the fluid and the particles involved in experiments. This classification allowed to characterize four different regimes of fluidization for different fluid-solids systems (subjected to ambient conditions) that were associated with four different groups of particles termed as group A, B, C and D (Figure 1.4).

Group C materials are the finest powders. Their characteristic diameter implies significant cohesive forces in air at room temperature (Baerns, 1966). Their fluidization is made difficult to obtain in these conditions, such as the fluid cannot easily move the particles away by breaking the contact bonds and tends to be channeled exclusively through the most permeable regions of the bed. This "channeling" effect leads to a heterogeneous fluidization associated with a poor particles mixing (Figure 1.4). However, this fluidization can be improved by using a mechanical stirrer capable of breaking the channels and homogenizing the fluidization. Once the group C powders are fluidized, their expansion can be significant (Girolami, 2008).

Group A powders are fine and slightly cohesive in air at room temperature. Their behavior is different from the other groups of powders, especially thanks to the presence of a stable particulate regime of fluidization obtained between U_{mf} and U_{mb} and associated with a uniform expansion of the material (Figure 1.4). The end of this stable regime is marked by the presence of hydrodynamic instabilities leading to the nucleation of cavities or bubbles.

Groups B and D materials are made of coarser particles that are large enough to discard from any interparticles forces in air at room temperature. These powders are characterized by a "bubbling fluidization" directly observed at the point of minimum fluidization such that there is no particulate regime for these materials ($U_{mf} = U_{mb}$).

After fluidization, if the fluid supply is abruptly cut, the bed will defluidize progressively by expelling the interstitial fluid from above and forming a loose deposit that progressively aggrades from the base.

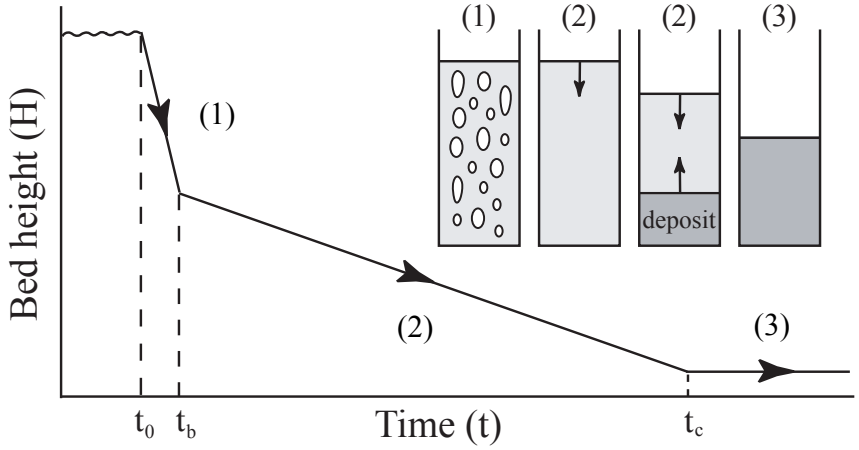

Figure 1.5

Fluid escape and sedimentation of the bed surface during a collapse-test performed after stopping the fluidization. t_0 represents the time at which the fluid supply is abruptly cut, t_b represents the time of bubbles expulsion, t_c represents the time of uniform defluidization that ultimately forms a loosely packed bed at the end of experiment.

This process is termed a bed collapse-test and allows to measure easily the sedimentation velocity of the bed surface (Geldart & Wong, 1985 ; Lettieri et al., 2000 ; Bruni et al., 2006 ; Girolami et al., 2008). In this study, we focus on the uniform fluidization regime obtained between U_{mf} and U_{mb} that allowed us to gain quantitative measurements of both fluidization and sedimentation velocities.

1.3 Material used

In the studies presented in this manuscript, different types of particles were used, in terms of size and density, all belonging to the Group A of the Geldart classification (Geldart, 1973). The selection of such particles was motivated by obtaining a large expansion rate of the mixtures which allowed us to explore in details the uniform particulate regime observed between U_{mf} and U_{mb}. This regime is characterized by the formation of a uniform suspension whose solid volume fraction is given by the inverse of the expansion

rate E. This latter is defined as the height ratio between the expanded suspension h_s and the packing bed (before fluidization) h_0 and was ranged from $E = 1.58$ to $E = 16.71$ for these materials. The mixture expansion rate was observed to be controled by the Stokes number as exposed in Chapter 2.

In experiments, three categories of glass beads were used, as well as PMMA beads and natural sand whose features are summarized in Table 1.1. The particles shape was observed using a scanning electron microscope (named 'MEB') available in the Medicine Faculty of the University of Tours. As exposed in Figure 1.6, all synthetical materials have a quasi-spherical shape, whilst the natural sand material is characterized by angular grains.

Features	ρ $(kg.m^{-3})$	$\Delta\rho$ $(kg.m^{-3})$	d_{50} (μm)	Δd_{50} (μm)	*Shape*
GB^1	2496	$\pm 0.32\%$	163	$\pm 2.27\%$	*Quasi-spherical*
GB^2	2496	$\pm 0.32\%$	240	$\pm 1.75\%$	*Quasi-spherical*
GB^3	2496	$\pm 0.32\%$	337	$\pm 4.18\%$	*Quasi-spherical*
$PMMA$	1200	$\leq 0.1\%$	200	$\leq 0.1\%$	*Spherical*
Sand	2655	$\pm 0.75\%$	312	$\pm 0.97\%$	*Angular*

Table 1.1

Mean features of the materials used in the physical modeling.

With the aim of ensuring the formation of uniform particulate suspensions in experiments, the materials involved were sieved in order to reduce their granulometric distribution and prevent the development of segregation. A first sieving was first performed to discard the finest particles, characterized as dusts. A second sieving was then performed to discard the coarsest particles, characterized as particles clusters. In this way, no size-segregation was develop in experiments involving such well-sorted materials in which each subset of particles is characterized by a value of minimum fluidization velocity U_{mf} that does not differ significantly from that of the others, as observed here and previously

described by Chen & Keairns (1975).

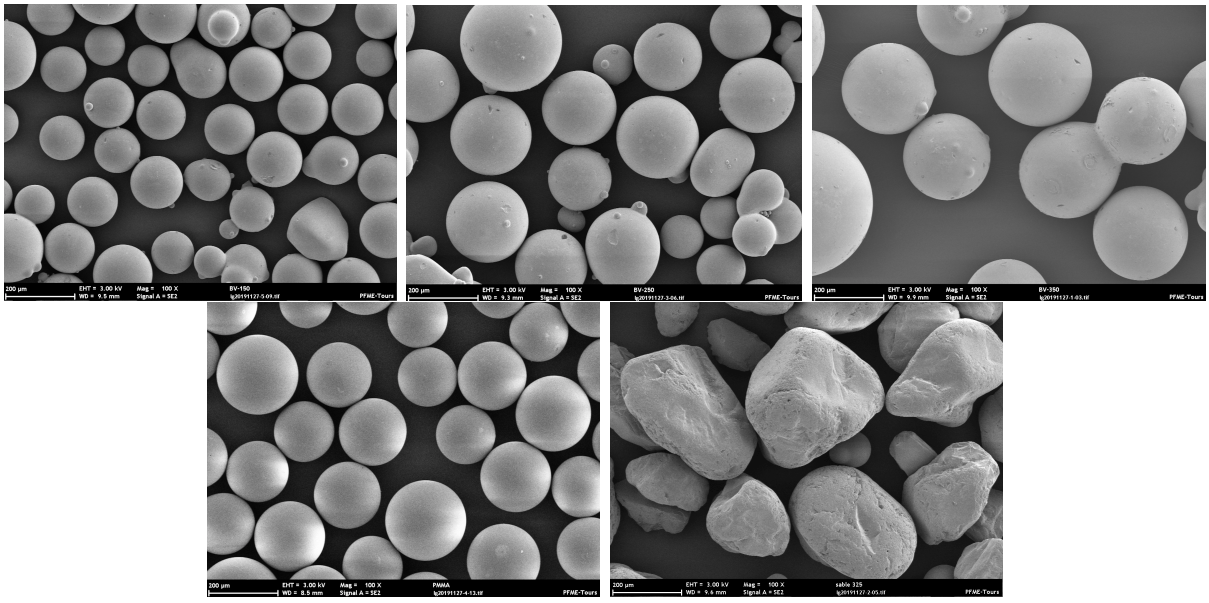

Figure 1.6

Pictures of the different particles (respectively GB^1, GB^2, GB^3, $PMMA$, *Sand*, from left to right) used in this study and get with a scanning electron microscope ('MEB').

Once sieved, a representative sample of the material batch used in experiments was obtained in aid of a splitter. The grain size distribution of each powder was then studied with a laser micro-granulometer Malvern mastersizer 3000, which uses the technics of a laser diffraction by measuring the light intensity scattered as a laser beam passes through a dispersed particulate sample. This data is then analyzed to calculate the particles size associated with the scattering pattern. For each material, ten measurements of the grain size distribution have been repeated and turn out to be enough to get an accurate measurement of d_{50}, with a reasonable error bar. The mean representative granulometric distribution obtained for each material is represented in Figure 1.7. The grain size distribution of the PMMA beads is narrower than that of the sand material or the coarsest glass beads, termed as GB^3.

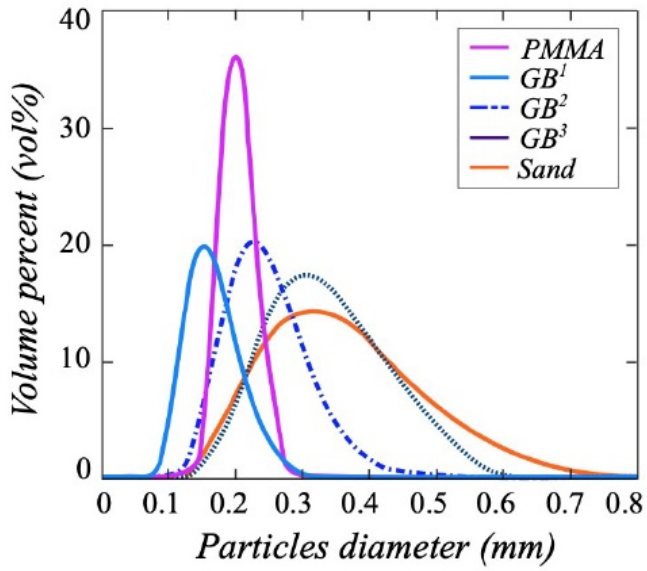

Figure 1.7

Grain size distribution of the different materials used in experiments.

The particles density was measured in aid of a pycnometer. The measurement is made with a liquid of known density ρ_{liq}, here water at a given temperature. The empty pycnometer is first weighted before the introduction of the sample and then water (Figure 1.8).

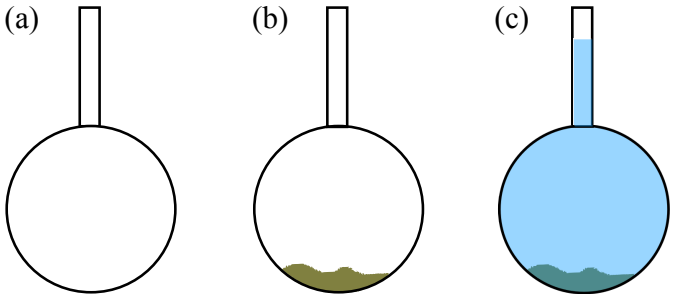

Figure 1.8

Measurement of the particles density with a pycnometer : (a) empty pycnometer ; (b) pycnometer with the solid sample ; (c) pycnometer filled by the solid sample and water taken at a known temperature.

Knowing the mass of the sample m_s, that of water m_{liq}, the density of the water ρ_{liq} at the given temperature, and the volume of the pycnometer V_{pyc}, we can deduce the volume of the sample V_s and thus its density ρ_s, such as :

$$\rho_s = \frac{m_s}{V_{pyc} - \left(\frac{m_{liq}}{\rho_{liq}}\right)}.$$

The measurements incertitude is calculated as follows :

$$\Delta d_{50} = \pm \frac{\max\left|d_{50(i)} - \overline{d_{50}}\right|}{\overline{d_{50}}} \times 100 \tag{1.1}$$

$$\Delta \rho_s = \pm \frac{\max\left|\rho_{s(i)} - \overline{\rho_s}\right|}{\overline{\rho_s}} \times 100 \tag{1.2}$$

Several samples were prepared with the splitter. The same method of grain size or density was applied. Each measurement gives one d_{50} (or ρ_s). A statistical average was calculated for all samples. The error percentage calculation was made by taking the greatest absolute difference between each measurement $(d_{50(i)}, \rho_{s(i)})$.

1.4 Suspensions features

The processes of fluidization are commonly used by the oil and gas companies, as well as in pharmaceutical industry. This technique consists in uniformly injecting a fluid at the base of a granular medium, at a known and controled velocity U_f, until forming a homogeneous suspension. The interest of using such a technique, here, lies in the ability of controling the solid volume fraction of the suspension ϕ_s at the beginning of each experiment, in aid of the direct measurement of the mixture expansion rate $E = \frac{h_s}{h_0}$, as well as the solid volume fraction of the bed at packing ϕ_{pack}, such as $\phi_s = \frac{\phi_{pack}}{E}$. The fluidization technique also allows to control the fluidization velocity U_f (measured with an accuracy of $\pm 2\%$) as well as measuring easily the sedimentation velocity of the bed surface U_{sed} (measured with an accuracy of $\pm 4\%$). The control of these parameters

ensures a satisfying reproducibility of the flows and enables to study their influence on the dynamics and emplacement of the suspensions characterized by their initial particles concentration normalized by their value at packing $\frac{\phi_s}{\phi_{pack}}$.

In the different studies presented here, different materials were used for the suspensions, such as glass beads characterized by different sizes, PMMA beads (a thermoplastic polymer) of similar mean diameter but of different density and a sand material of similar mean diameter and density but characterized by different shapes and a larger granulometric distribution. The choice of the different materials was made to study the influence of such parameters (size, density, shape, granulometric distribution) on the dynamics and sedimentation processes of the suspensions. The properties of the particles are summarized in Table 1.1. The fluid used was water brought to different temperatures such as slightly varying its dynamic viscosity. The results obtained with the liquid-solid suspensions were then compared with similar experiments performed with other types of particles and fluids, such as : volcanic ash and chemical catalysts (FCCs) and air (Girolami et al., 2008 ; 2015).

1.5 Suspensions dynamics

The fluidization processes, largely developed in natural flows, act in significantly reducing the friction between particles, thus increasing the flows mobility and more specifically their ability to travel large distances down gentle slopes, with degrees quite inferior to that determined by the internal friction angle of the material involved in the mixture (Girolami et al., 2008). When the channel is filled with air, the flows generated in experiments are free-surface flows and allow the study of natural phenomena such as the final course of non-colloidal mud-flows in which the sedimentation processes are dominant. In this case, the initial suspension (prepared in the reservoir) does also have a free surface (e.g. not overlyed by a column of water) with a constant height h_0. For this reason, the principal reservoir was separated into two compartments (Figure 1.9). At the vicinity of

the sliding gate, the frontal part was used as a smaller fluidization rig. At the rear of the reservoir, in the back part, a spillway was constructed in order to allow the instantaneous expel of water from the suspension surface and maintains its height constant over time (Figure 1.9).

Otherwise, when the channel was completely filled with water, the flows generated in experiments are immersed flows, with no effect of the free surface, and enable the study of submarine avalanches and turbidity currents that travel and deposit in deep marine environments. In this case, the initial suspension (prepared in the reservoir) is also immersed (e.g. overlyed by a column of water), such that the height h_0 can vary from one experiment to another.

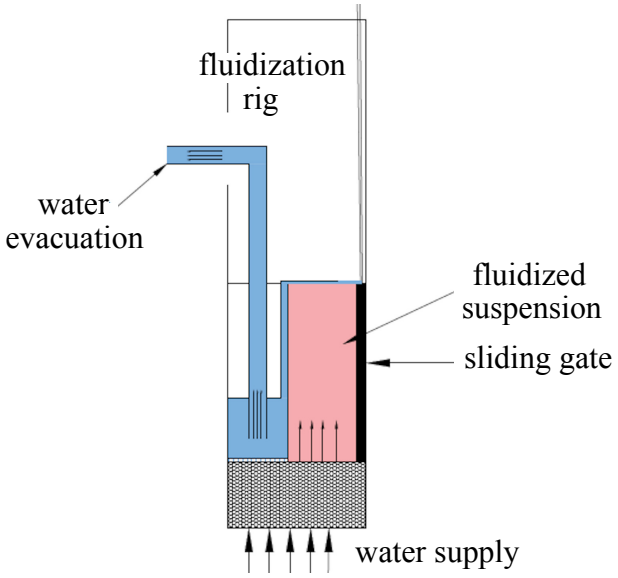

Figure 1.9

Scheme of the reservoir configuration in the case of free-surface flows that require the formation of free-surface suspensions in the fluidization rig before release.

The flows thus generated are characterized as fast flows (whose speed is greater than $2m.s^{-1}$) and thus require the use of a high-speed video camera. The model 'LaVision Phantom VEO340L' was used to record all the flows at frequencies ranged between 800

and 1700 Hz (e.g. 800 to 1700 frames per second). The reproducibility of each flow, from suspensions prepared in the same initial conditions, allowed us to record different movies for a same experiment (Figure 1.10). For each experiment, the recording includes :

- a global film (of around 3 m wide) that enables to visualize the entire flow from the suspension release in the reservoir to the stop of the flow front (Figure 1.10).

- a series of visualization windows (of 50 cm wide) from which the post-processing was made possible and greatly improved (Figure 1.10). The contrasts obtained in these movies allowed to explore in detail the sedimentation processes during the flow. Note however that the flow front thickness was too thin to pursue the study beyond a distance of 2 m from the sliding gate.

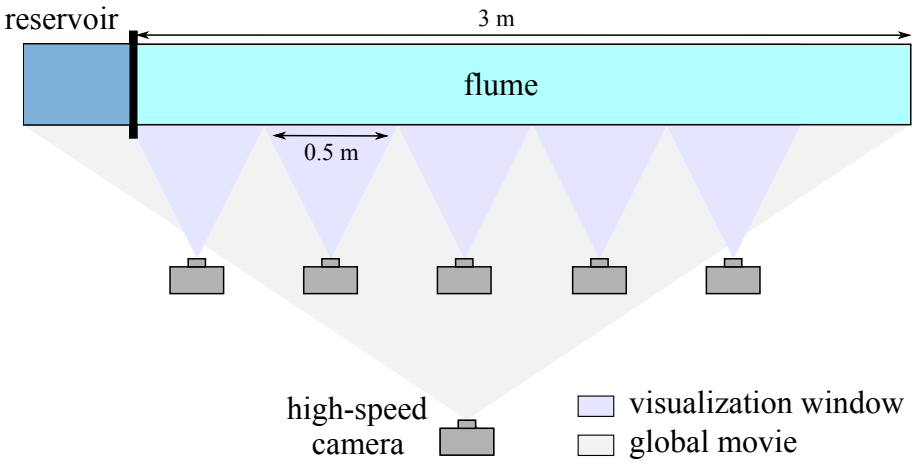

Figure 1.10

Positions of the high-speed video cameras placed along the flume for each experiment generated from suspensions prepared in similar initial conditions.

1.6 Imagery and visualization

After experiments, the post-processing of the movies includes different steps. First, a visual analysis allowed us to determine the aggradation rates of the basal deposit formed within the flows during propagation, the velocity at which the water layer is expelled from above in the cases of free-surface flows, as well as the frontal position over time.

The measurements of the aggradation velocity were taken at a given location x and consisted of measuring the thickness of the deposit h over time t. The kinematic profiles consisted in measuring the position of the flow front x_F over a small time interval $\Delta t \simeq 0.05\ s$. Once acquired, we studied the correlation between the flow and the settled bed by taking the deposit morphology at a given time from the visualization windows that we correlate to the global flow.

The velocity fields and profiles, measured in the flows, are obtained by a PIV (Particle Image Velocimetry) study. The first step of this processing consists in applying a filter on each image to highlight the signal. We call it 'pre-treatment' because it is applied before the PIV process. Then a geometric mask is applied to reduce the calculation area from the whole frame to the area of interest (thus discarding from any useless calculation performed on the background of the flume, that can furthermore generate noise). Finally, the PIV calculation is carried out by determining the velocity vectors (taking relevant time and space steps) inside the flow and between two consecutive images. The different steps of post-processing are summarized below :

- a temporal filter allows the extraction of the background. It aims at removing the static frame signal.

- a geometric mask is employed to significantly reduce the calculation time to the area of interest.

- a non-linear filter is used to normalize the image (min-max). It has been applied on 80 pixels (including the PIV pre-processing).

- the PIV calculation is first performed on a $64px \times 64px$ "pass" mesh (squared window) with an overlap of around 75%. It allows to mesh the whole study area. Afterwards, the calculation is applied on the first outputs with a final $32px \times 32px$ pass on a circular window in order to obtain the final resolution of the grid.

- the post-processing allows to convert the raw vectors (determined in pixels/frame, Figure 1.11) to velocity vectors (in m/s). It also allows the calculation of the correlation coefficient.

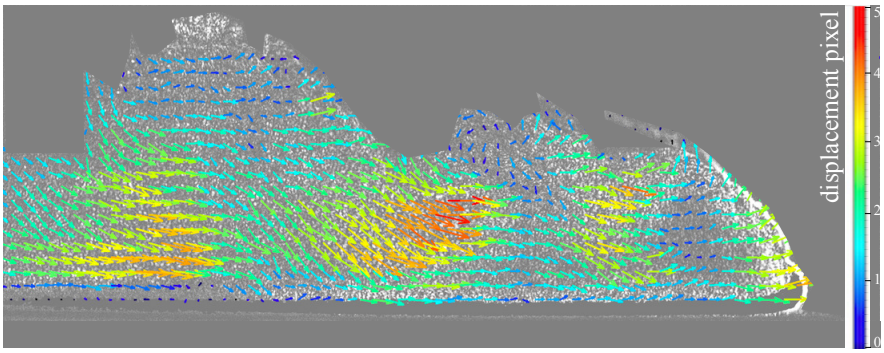

Figure 1.11

Illustration of the raw displacement vectors (determined in pixels) calculated within a submarine avalanche traveling down the proximal part of the flume, using the PIV software of LaVision.

After the PIV calculations, velocity profiles can be calculated within the flows for different distances x along the flume (Figure 1.12). In the same manner, the profile is first calculated in pixels per frame such that a correction is required to convert the pixels displacement into a velocity. The correlation is made by taking both known vertical and horizontal scales in centimetres and in pixels in order to get the correlation factor in cm/px (or m/px). The correction in time is made in aid of the camera frequency and the number of images.

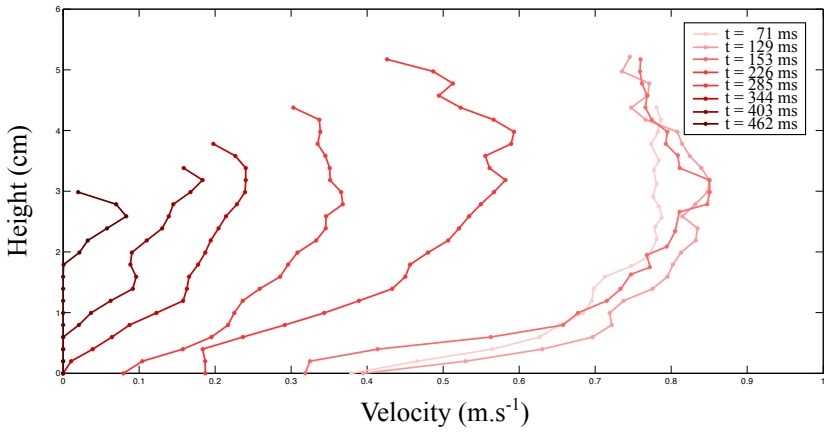

Figure 1.12

Illustration of the velocity profiles determined inside a free-surface non colloidal mud-flow, from the LaVision software, at the vicinity of the sliding gate.

Note that for a standard flow movie (including around 3000 frames), the time of calculation is about 1 or 2 hours for the pre-processing and about 6 hours for the PIV calculation and the post-processing. It means that a total of around 7-8 hours of calculation is required to obtain the velocity fields and profiles for each visualization window.

Bibliographie

Baerns M. (1966), Effect of interparticle adhesive forces on fluidization of fine particles, Ind. Eng. Chem. Fundam. 5, 50516.

Bruni B., P. Lettieri, D. Newton, and J. Yates, (2006) The influence of fines size distribution on the behaviour of gas fluidized beds at high temperature, Powder Technology, 163, pp. 88-97.

Chen J. L. P. and D. L. Keairns, (1975) Particle segregation in a fluidized bed, Can.

J. Chem. Eng. 53, 395.

Eames I., and M.A. Gilbertson (2000), Aerated granular flow over a horizontal rigid surface, J. Fluid Mechanics, 424, 169-195.

Geldart D. (1973) Types of gas fluidization, Powder Technology, 7, 285-292.

Geldart D., and A.C.Y Wong, (1985) Fluidization of powders showing degrees of cohesiveness, II, Experiments on rates of deaeration, Chemical Engineering Sciences, 40, 653-661.

Girolami L. (2008) Dynamique et sÈdimentation des Ècoulements pyroclastiques reproduits en laboratoire, PhD dissertation, Clermont-Ferrand-2.

Girolami L., O. Roche, T.H. Druitt, and T. Corpetti, (2010) Particle velocity fields and depositional processes in laboratory ash flows, with implications for the sedimentation of dense pyroclastic flows, Bulletin of Volcanology, 72(6), pp. 747-759.

Girolami L., T.H. Druitt, and O. Roche, (2015) Towards a quantitative understanding of pyroclastic flows : effects of expansion on the dynamics of laboratory fluidized granular flows, Journal of Volcanology and Geothermal Research, 296, pp. 31-39.

Girolami L., and F. Risso, (2018) Rheological behaviour and runout of short-lived fast-moving flows of hot, dense suspensions, Journal of Energy Challenges and Mechanics 5 (1), 17-23.

Lettieri P., J.G. Yates, and D. Newton (2000) The influence of inter-particle forces on the fluidization behaviour of some industrial materials at high temperature, Powder Technology, 110, pp. 117-127.

Chapitre 2

Sedimentation behavior of particulate suspensions

This chapter concerns a publication in a peer-reviewed journal.

On the fluidization/sedimentation velocity of a homogeneous suspension in a low-inertia fluid.

by Ahmad Amin, Laurence Girolami, Frédéric Risso.

Powder Technology, 391, 1-10, DOI :10.1016/j.powtec.2021.05.073.

Abstract

The modeling of the fluidization or sedimentation velocity of a suspension of solid particles is revisited by examining experiments conducted in either a liquid or a gas. A general expression is found in the case of negligible fluid inertia, i.e. at low Reynolds or Archimedes number. It is built as the product of the velocity of an isolated particle by three non-dimensional corrections that each takes into account a specific physical mechanism. The first correction reflects the variation of the buoyancy with the particle concentration. The second correction describes how the drag force increases with the concentration in case of negligible particle inertia. The third one accounts for the further

increase of the drag when the particle inertia is increased. Remarkably, each correction only relies on a single of the three independent non-dimensional groups that control the problem : (1) the particle volume fraction Φ_s ; (2) the ratio Φ_s/Φ_{pack} where Φ_{pack} is the bed packing concentration ; (3) the Stokes number $\mathcal{S}t_0$, which characterizes the inertia of the particles and controls their agitation. Moreover, the onset of the instability that separates the homogeneous regime from the heterogeneous one is found to be controlled similarly by the Stokes number. Empirical expressions of the corrections are given, which provide a reliable tool to predict fluidization and sedimentation velocities for all values of the three non-dimensional numbers. The present results emphasize the crucial role of particle inertia, which is often disregarded in previous modeling approaches, such as that of Richardson and Zaki.

Keywords : Fluidization velocity sedimentation velocity, liquid-solid fluidized beds, gas-solid fluidized beds, particulate suspensions.

2.1 Introduction

This article revisits two closely related fundamental problems : the fluidization of solid particles by an upward flow of fluid and the sedimentation of population of solid particles in a fluid at rest. The physics of these configurations is complex because of the intricate interplay between the continuous fluid phase and the dispersed solid phase. Especially, the interactions between the particles may involve hydrodynamic forces, shocks between particles, solid friction, short-range adhesion forces... In this work, we focus on the case where hydrodynamic forces are predominant, shocks possibly play a significant role, whereas the other effects are negligible. This situation is achieved when the continuous phase is liquid, provided that the particles are not too small to avoid colloidal or Brownian effects, and that their concentration is not too close to packing to avoid solid friction and jamming. It can also be obtained in a gas that is heated in order to prevent capillary forces resulting from moisture. In this context, there exists a range of solid volume fractions in which the flow is homogeneous. Apart from a narrow region close to the wall, the average particle velocity, fluid velocity and volume fraction Φ_s are spatially uniform. The sedimentation and fluidization processes thus only differ by a Galilean change of reference frame, so that the fluidization velocity U_f and the sedimentation velocity U_{sed} are equal, and will be referred as U in the following of this paper. This range is limited by an upper boundary Φ_{up} and a lower boundary Φ_{low}. Let us consider a fluidization experiment in which the fluidization velocity is regularly increased while the concentration of the mixture decreases. Concentration Φ_{up} is reached when the solid friction between the particles ceases to play a significant role and the influence of the walls becomes negligible. It is close to the concentration of the bed at the minimum fluidization velocity and corresponds to the end of the jamming state. Concentration Φ_{low} is reached when strong large-scale fluctuations of the particle concentration develop, giving birth to the well-known bubbling regime in gas-solid fluidized beds. Within the homogeneous regime, the dynamics is controlled by four main forces : (1) the effective weight of the particles, which depends on the density

difference between the two phases ; (2) the viscous stresses within the fluid, which control the dissipation of mechanical energy ; (3) the fluid inertial stresses, which influence the flow between the particles ; (4) the particle inertia, which determines the intensity of particle-velocity fluctuations relative to those of the fluid. The relative magnitude of these forces depends on the physical parameters that characterize the two phases, which makes it difficult to provide a unified description, valid for a wide range of situations, and to find a universal law capable of describing the relation between U and Φ_s.

Historically, two different ways have been opened to address the problem. The first, initiated by Richardson and Zaki Richardson & Zaki (1954); Richardson & D (1954) considers the dilute state as a starting point, whereas the second, developed by Abrahamsen and Geldart Abrahamsen & Geldart (1980), starts from the packing state.

Let's begin with the Richardson-and-Zaki's approach. The average velocity U is modeled as a correction to the velocity U_i of an isolated settling particle in the corresponding flow regime,

$$U = U_i \left(1 - \Phi_s\right)^n \ , \tag{2.1}$$

where n is an exponent that is expected to depend on the particle Reynolds number Re, being equal to 4.65 in the limit of vanishing Re. This approach has become very popular and many studies have shown that eq. 2.1 describes experimental results well, provided that U_i and n are adequately chosen (see Kramer *et al.* (2019) and references therein). Then, several works have investigated how this law can be extended to account for more complex effects, such as suspensions of binary particles Funamizu & Takakuwa (1995), adhesion forces depending on temperature Lettieri *et al.* (2002), magnetic field Valverde & Castellanos (2008), multisized irregular particles Bargieł & Tory (2013)... However, even considering the simplest case of a monodisperse homogeneous suspension of spheres in the absence of adhesion forces, this approach has limitations. First, eq. 2.6 predicts that the sedimentation velocity U becomes null at $\Phi = 1$ although it actually vanishes when the jamming occurs, at a concentration which is less than unity. As a consequence, such a

law necessarily ceases to be valid when approaching the packing state. On the other hand, the homogeneous regime is destabilized at a concentration Φ_{low}, which is not necessarily small. There is hence no reason to expect that a law that is relevant for $\Phi > \Phi_{low}$ would still be valid in the limit of vanishing concentration, and the value of U_i involved in eq. 2.6 does not represent the terminal velocity of an isolated settling particle, as it will be shown later. In addition, by following the original dimensional analysis of Richardson and Zaki Richardson & D (1954), the proposed expressions for n and U_i Kramer *et al.* (2019) generally do not account for the particle inertia, which questions their validity when the particle-to-fluid density ratio can significantly vary from one case to another.

The alternative approach is more specific to the fluidized-bed configuration. The fluidization velocity is modeled as a correction to the minimum velocity U_{mf} required to fluidize the bed Abrahamsen & Geldart (1980),

$$U = U_{mf} + \frac{g\,(\rho_s - \rho_f)\,d^2}{210\;\mu_f}\left[\frac{(1-\Phi_s)^3}{\Phi_s} - \frac{(1-\Phi_{pack})^3}{\Phi_{pack}}\right], \tag{2.2}$$

where g is the gravitational acceleration, ρ_s the density of the particle, ρ_f the density of the fluid, d the particle diameter, μ_f the fluid dynamic viscosity and Φ_{pack} the particle volume fraction of the bed just before expansion. This approach is based on the description of the flow through a porous medium of porosity $\epsilon = 1 - \Phi_s$, and can be seen as an extension of the original work of Ergun Ergun (1952). Being based on the properties of the bed at U_{mf}, it is expected to be relevant at concentrations close to Φ_{up}. But it can hardly constitute a universal law, since its evolution away from Φ_{pack} does not involve parameters that may account for the variations, between the many possible different fluid/particle systems, of the magnitude of the four main forces listed above. Nevertheless, this approach emphasizes that a model that intends to describe the entire homogeneous regime should probably involve Φ_{pack}.

Suspensions are often described as an equivalent continuous medium of effective viscosity μ_m. Since the pioneering work of Einstein in 1905, which dealt with the dilute limit, and that of Krieger and Dougherty Krieger & Dougherty (1959), which proposed a way

to continuously connect the dilute and the concentrated regime, many authors have been attempted to model the effective rheology of a suspension (see Guazzelli & Pouliquen (2018*a*) for a recent review). The definition of an effective viscosity requires to consider a volume that contains enough particles so that the average particle volume concentration can be considered as a relevant parameter at this scale Hinch (1977*a*). Consequently, if the effective viscosity is suitable to predict the sedimentation velocity of a large body falling in a suspension of small particles, it is questionable to relate it to the settling velocity of the small particles that make up the suspension. For that reason, although both problems are closely related, the literature on sedimentation/fluidization velocity is disconnected from that on suspension rheology, except in rare cases as Koo (2008). Considering an effective viscosity determined from the mean sedimentation velocity of the particles, which differs from that measured in large-scale sheared suspensions, is however not without interest. This important issue has been recently addressed by two of the authors Girolami & Risso (2019), who defined the effective mixture viscosity μ_m by balancing the buoyancy force acting on a spherical particle, $g(\rho_s - \rho_f)\frac{\pi}{6}d^3$, to the Stokes drag, $3\pi\,\mu_m\,d\,\frac{U}{1-\Phi_s}$, acting on a particle that moves at velocity $\frac{U}{1-\Phi_s}$ relative to a fluid of viscosity μ_m. This definition turns out to be the only way to gather the experimental values of U, measured for three different types of small particles fluidized by a gas, on a master curve of the form

$$\frac{\mu_m}{\mu_f} = \frac{U_0(1-\Phi_s)}{U} = F\left(\frac{\Phi_s}{\Phi_{pack}}\right), \tag{2.3}$$

where

$$U_0 = \frac{g(\rho_s - \rho_f)d^2}{18\mu_f} \tag{2.4}$$

is the Stokes velocity for an isolated settling particle, and F is an empirical function that is independent of the nature of the particles. This equation describes non-cohesive fine particles suspended by a gas all over the homogeneous regime. In particular, this law is expected to be valid for fluid catalytic cracking (FCC) or volcanic ash which are both able to generate highly expanded suspensions at high temperature Girolami (2008); Girolami

et al. (2015). However, the question of its generalization to lower particle-to-fluid density ratios, as those corresponding to particles in liquids, remains open and represents the principal objective of this present paper.

In the present work, a fluidization column is used to measure the fluidization and the sedimentation velocities of a suspension of solid particles in a liquid. A series of experiments were carried out for various particle sizes, particle densities and liquid viscosities. Combined with experimental results of our previous work Girolami & Risso (2019) which were performed by using a gas, this amounts to exploring a wide range of the control parameters. From the analysis of these data, we propose an expression able to accurately predict the value of U for any systems involving a suspension of particles all over the homogeneous regime ranging from Φ_{low} to Φ_{up}, provided that the inertia of the fluid is negligible. This law relies on the key physical parameters that describe the particle/fluid system, namely the Stokes velocity of an isolated particle, the particle volume fraction, a specific packing concentration, and a Stokes number. In addition, the values of Φ_{up} and Φ_{low} are also determined and found to be simple functions of the Stokes number, which provides a prediction of the achievable expansion in a fluidization column.

This paper is organized as follows. Section 2.2 reviews the involved physical parameters and introduces the relevant dimensionless groups. Section 2.3 describes the experimental setup and presents the investigated systems. Section 2.4 analyzes the results by means of Richardson-Zaki's and Abrahamsen-Geldart's approaches. Section 2.5 describes our approach and introduces a new sedimentation/fluidization law. Section 2.6 examines the boundaries of the homogeneous range. Finally, concluding remarks are given in Section 2.7.

2.2 Dimensional analysis

We consider the fluidization and the sedimentation of a homogeneous suspension of non-cohesive particles in a fluid. Each particle is characterized by its density ρ_p, its

equivalent diameter $d = (6\vartheta_p/\pi)^{1/3}$, and its shape. In the case where all particles do not have the same size, we consider that d is either the mean or median of the diameter distribution. The solid particles are made of a homogeneous material of density ρ_s, so that $\rho_p = \rho_s$.

The concentration of the suspension is characterized by the particle (or solid) volume fraction, Φ_s, or equivalently by the fluid volume fraction (or bed porosity), $\epsilon = 1 - \Phi_s$. In order to be able to describe large concentration cases, it is useful to introduce a packing concentration, Φ_{pack}, which is defined as the particle volume fraction of a fluidized bed just below the minimum fluidization velocity or that of a settling suspension at the point where the sedimentation velocity vanishes. Note that, in a fluidized bed, Φ_{pack}/Φ_s corresponds to the bed expansion, which can be measured from the ratio between the fluidized bed height and the initial bed height, without knowing the value of Φ_{pack}. It is also worth mentioning that, when considering a population of particles with non-uniform distributions of size and shape, Φ_{pack} embeds important information about these distributions, which can be enough to determine the sedimentation/fluidization velocity U in certain cases, such as those of heated volcanic ash in a gas Girolami & Risso (2019, 2020).

Then, we consider a Newtonian fluid which is characterized by its density, ρ_f and dynamic viscosity, μ_f. Finally, we account for a uniform gravity field of acceleration g. Since gravity is only involved in weight and buoyancy, it is better to consider the effective weight $g(\rho_p - \rho_f)$. Also, since the particles are moving relatively to a fluid, it is better to consider their effective inertia, $\rho_p + C_M\rho_f$, where $C_M\rho_f$ represents for the mass of fluid entrained by a particle while C_M is the added-mass coefficient, which is equal to $1/2$ for a sphere.

The problem is thus controlled by seven parameters, two non-dimensional ones (Φ_s, Φ_{pack}) and five dimensional ones (ρ_f, μ_f, d, $\rho_p + 1/2\rho_f$, $g(\rho_p - \rho_f)$), and involves three physical dimensions (length, mass, time). The problem is thus fully characterized by $7 - 3 = 4$ independent non-dimensional groups. We thus need to build two non-dimensional groups in addition to Φ_s and Φ_{pack}. Since numerous practical configurations involve fine par-

ticles, viscous forces are often dominant. It is thus relevant to introduce non-dimensional numbers that compare inertial forces to viscous ones.

Let us begin by considering the inertia of the fluid. The Reynolds number, $Re = \rho_f dU/\mu_f$, is the non-dimensional group that compares fluid inertial stresses to viscous ones. However, U being not an initial parameter, we need to replace it by a velocity scale that is built on the control parameters. Considering the settling velocity U_0 of a single particle in the Stokes regime (Eq. 2.4), we get the Archimedes number, $\mathcal{A}r = \frac{\rho_f(\rho_p-\rho_f)gd^3}{18\mu_f^2}$.

Evaluating the importance of the particle inertia force is more delicate. Indeed, this force does not play any role when a particle moves at a constant velocity and is therefore associated with the velocity fluctuations that take place in a settling or fluidized suspension. We thus introduce the Stokes number, $\mathcal{S}t = \tau_p/t_f$, which compares the particle response time, τ_p, to the time scale of the fluctuations of the fluid velocity, t_f. By balancing particle inertia, $\frac{(\rho_p+1/2\rho_f)\pi d^3U}{6\tau_p}$ and Stokes drag, $3\pi\mu_f dU$, τ_p is found to scale with $\frac{(\rho_p+1/2\rho_f)d^2}{\mu_f}$. Then, t_f can be estimated as d/U, which leads to $\mathcal{S}t = \frac{(\rho_p+1/2\rho_f)dU}{\mu_f}$. Finally, by replacing U by U_0, we obtain a Stokes number that depends only on the initial control parameters : $\mathcal{S}t_0 = \frac{(\rho_p+1/2\rho_f)(\rho_p-\rho_f)gd^3}{18\mu_f^2}$.

The problem is then fully characterized by Φ_s, Φ_{pack}, Ar and St_0. Note that Ar is the only non-dimensional group that can be constructed from the three physical parameters when $\rho_p + 1/2\rho_f$ is removed, while St_0 is the only one when ρ_f is disregarded. Therefore, in cases where $\mathcal{A}r$ (or Re) is small, the inertia of the fluid can be neglected, whereas in cases where $\mathcal{S}t_0$ (or $\mathcal{S}t$) is small, that is the inertia of the particle that is negligible.

2.3 Experimental setup, procedures and regime characterization

We report fluidization and sedimentation experiments that were carried out in the experimental setup schematized in figure 3.1. It includes a transparent vertical column

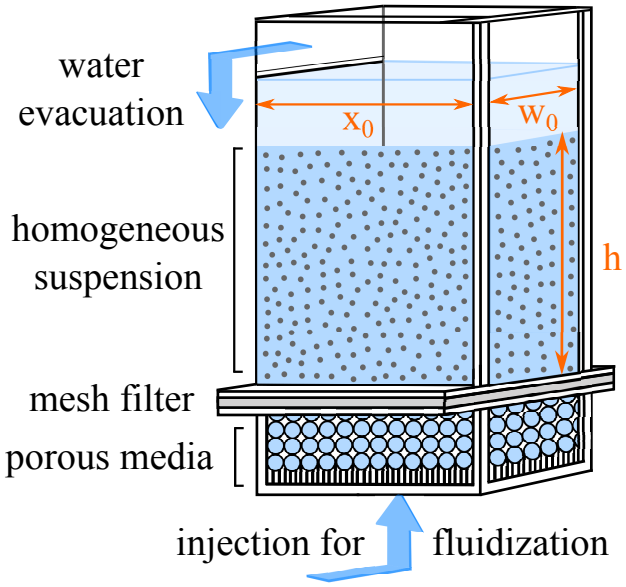

Figure 2.1

Scheme of the fluidization column.

of height $H = 0.7$ m which has a rectangular cross-section of sides $x_0 = 0.2$ m and $w_0 = 0.3$ m. A liquid, supplied by a centrifugal pump, can be injected at the bottom of the column through an array of straws discharging in a stack of large glass pebbles and smaller lead beads, all covered by a mesh filter. This injection system ensures a uniform liquid flow and prevents the solid particles from leaving the column. At the top, an evacuation system is connected to an external tank which allows a closed-loop flow.

The experimental procedure can be described as follows. The column is filled with a mixture of solid particles and a liquid. The particles being denser than the liquid, they form a bed of initial height h_0. The bed consists of a loose random packing at a concentration Φ_{pack}. The total volume of solid ϑ_s having been preliminarily measured, the initial concentration is determined as $\Phi_{pack} = \frac{\vartheta_s}{x_0 w_0 h_0}$. Then, the liquid is injected from the bottom at a given flow rate Q, corresponding to a fluidization velocity $U_f = \frac{Q}{x_0 w_0}$, determined with an accuracy of $\pm$ 2%. Provided U_f is larger than the minimum fluidization velocity, the bed expands, reaching a height $h > h_0$ and a concentration Φ_s,

which correspond to an expansion $E = \frac{h}{h_0}$, determined with an accuracy of ± 2%. The normalized concentration is thus obtained from $\frac{\Phi_s}{\Phi_{pack}} = \frac{1}{E}$ while the concentration is given by $\Phi_s = \frac{\Phi_{pack}}{E}$, with an accuracy of ± 4%. When the liquid injection is stopped, the sedimentation velocity is measured from the duration Δt taken by the bed to settle : $U_{sed} = \frac{h-h_0}{\Delta t}$, with an accuracy of ± 4%. A preliminary fluidization-sedimentation cycle is performed before the collect of data, so that the initial packing state Φ_{pack} is the result of particle sedimentation and not to an arbitrary configuration following the filling of the column. Then, a series of cycles are carried out for different liquid flow rates in order to measure how U_f and U_{sed} evolve with the particle concentration. For each considered system of a fluid and particles, the boundaries Φ_{up} and Φ_{low} of the homogeneous regime are determined. Practically, Φ_{up}, is here determined as the concentration corresponding to the minimum flow-rate for which a visible bed expansion is achieved. Φ_{low} corresponds to the limit of stability of the bed beyond which visible fluctuations of concentration develop and its surface begins to be agitated. Note that this transition is quite abrupt, which makes possible its determination with a good accuracy.

Various systems are investigated (see Table 2.1 for a summary of their properties). Five sets of particles made of three different solid materials have been studied, the density of which has been measured by means of a pycnometer : one set of light PMMA beads, three sets of glass beads of different sizes (GB^1, GB^2 and GB^3), and one set of sand grains. Ten samples of each set of particles have been analyzed by using a laser granulometer. Figure 2.2 shows the distributions of the particle equivalent diameters ($d = (6\vartheta_p/\pi)^{1/3}$). Beside, the shape of the particles was observed using a microscopic image of each sample, also shown in fig. 2.2. PMMA beads are almost spherical with a narrow size distribution. Glass beads are also almost spherical with a size distribution that is broader for the sets of larger particle sizes. Sand particles are less spherical and have a rather broad size distribution. In what follows, the particle size of each set will be characterized by the median diameter d_{50} of the distribution, we will thus be assimilated to d. In any case, the liquid is water but two different operating temperatures are used in order to vary the

Experimental parameters	$PMMA$	GB^1	GB^2	GB^3	$Sand$	Ash^1	Ash^2	FCC
Solid density ρ_p [kg m^{-3}]	1200	2500	2500	2500	2650	1600	1490	1420
Mean diameter d [μm]	210	160	240	335	310	80	65	70
Fluid density ρ_f [kg m^{-3}]	998	998	998	998	998	0.79	0.79	0.79
Fluid viscosity μ_f [Pas]	10^{-3}	10^{-3}	10^{-3}	10^{-3}	10^{-3}	$2.4\,10^{-5}$	$2.4\,10^{-5}$	$2.4\,10^{-5}$
Packing state Φ_{pack}	0.64	0.60	0.60	0.58	0.56	0.58	0.60	0.58
Fluidization regime $\frac{\phi_{up}}{\phi_{pack}}$	0.987	0.955	0.966	0.972	0.967	0.94	0.95	0.95
Stability regime $\frac{\phi_{low}}{\phi_{pack}}$	0.06	0.16	0.38	0.62	0.47	0.70	0.71	0.82
Uniform regime $\frac{\phi_{up}}{\phi_{low}}$	16.45	5.97	2.54	1.80	1.57	1.34	1.34	1.16
$\mathcal{A}r = \frac{\rho_f(\rho_p-\rho_f)gd^3}{18\mu_f^2}$	1	3	11	31	28	0.6	0.3	0.4
$\mathcal{S}t_0 = \frac{(\rho_p-\rho_f)(\rho_s+\frac{1}{2}\rho_f)gd^3}{18\ \mu_f^2}$	1.6	10	34	94	88	1176	545	655

Table 2.1

Experimental parameters for both liquid-solid suspensions ($PMMA$; GB^1 ; GB^2 ; GB^3 ; $Sand$) at 20^{o}C and gas-solid suspensions (Ash^1 ; Ash^2 ; FCC) at 170^{o}C.

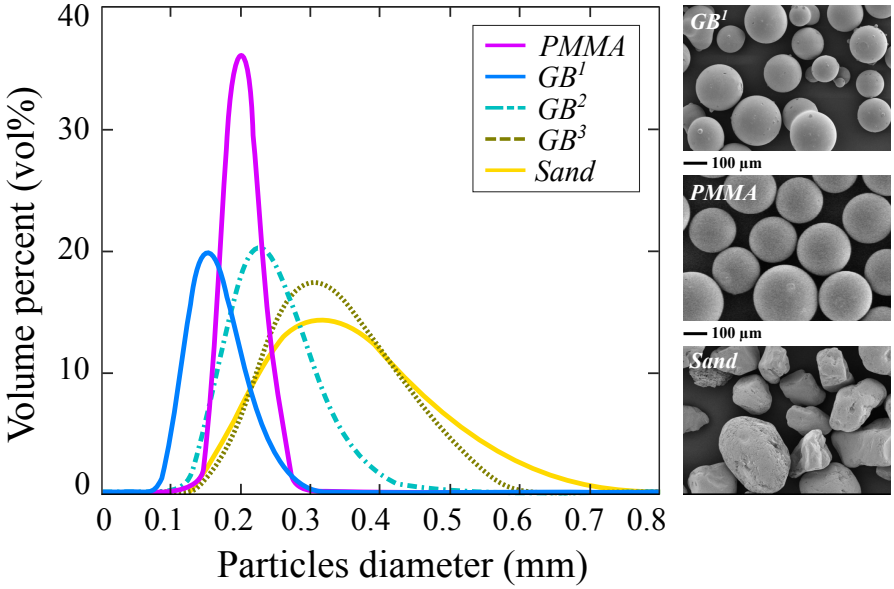

Figure 2.2

Particle size distribution and microscopic pictures of the materials used in the experiments.

viscosity : $\mu_l = 1.00 \times 10^{-3}$ Pa s at 20^{o}C or $\mu_l = 0.72 \times 10^{-3}$ Pa s at 35^{o}C.

In addition to these new experiments, the present analysis will also consider results obtained in a recent study Girolami & Risso (2019). This previous work investigated two sets of non-spherical ash particles (Ash^1 and Ash^2) and one set of almost spherical FCC particles, which were fluidized in air at 170^{o}C Girolami (2008). The physical parameters of these experiments are also reported in Table 2.1. Even though two different setups are used, the experimental procedures of the previous and present experimental campaigns are similar and their results can thus be compared without limitations. Combining results obtained in either a liquid or a gas allows us to explore a very broad range of the Stokes number and thus to reveal the role of the particle inertia.

Figure 3 shows the measured fluidization velocity U_f and sedimentation velocity U_{sed} as a function of the normalized concentration $\frac{\Phi_s}{\Phi_{pack}}$ over the whole range of the stable homogeneous regime between $\frac{\Phi_{low}}{\Phi_{pack}}$ and $\frac{\Phi_{up}}{\Phi_{pack}}$ for all the systems under investigation. In all cases, U_f and U_{sed} are equal within the measurement accuracy, which confirms that wall

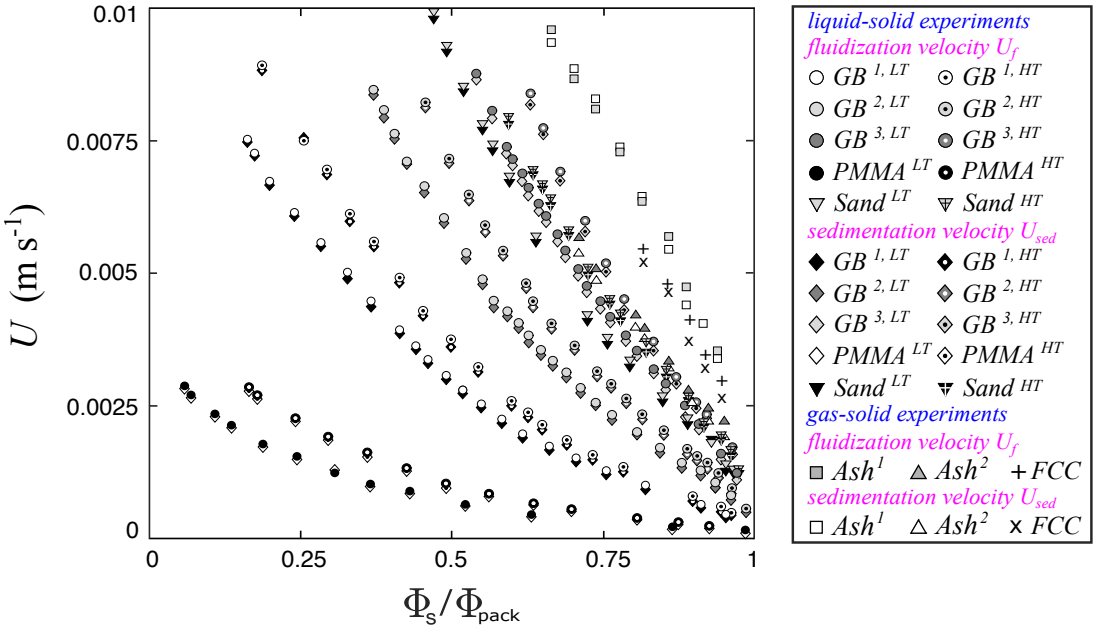

Figure 2.3

Fluidization velocity U_f and sedimentation velocity U_{sed} represented as a function of the normalized solid particle volume fraction $\frac{\phi_s}{\phi_{pack}}$ for both liquid-solid and gas-solid suspensions.

effects are negligible. In what follows, we will no longer distinguish them and consider a single velocity U, the value of which is set equal to the sedimentation velocity U_{sed}. Velocity U decreases with the concentration, but depending on the system under consideration, its values differ greatly. In particular, light PMMA particles in water feature the lowest values, the weakest decrease and the broader homogeneous range, whereas the reverse is true for particles in gas. Considering non-dimensional quantities is therefore necessary to interpret the results.

Table 2.1 gives the non-dimensional control parameters $\mathcal{A}r$ and $\mathcal{S}t_0$ for all sets of solid particles in water at 20^{o}C and in air at 170^{o}C. The Archimedes number remains moderate ($\mathcal{A}r < 30$) while the Stokes number reaches very large values ($\mathcal{S}t_0 >$1000). Disparities between the values of U of the different fluid-and-particle systems are thus rather expected to be associated with variations of particulate inertia than to fluid one.

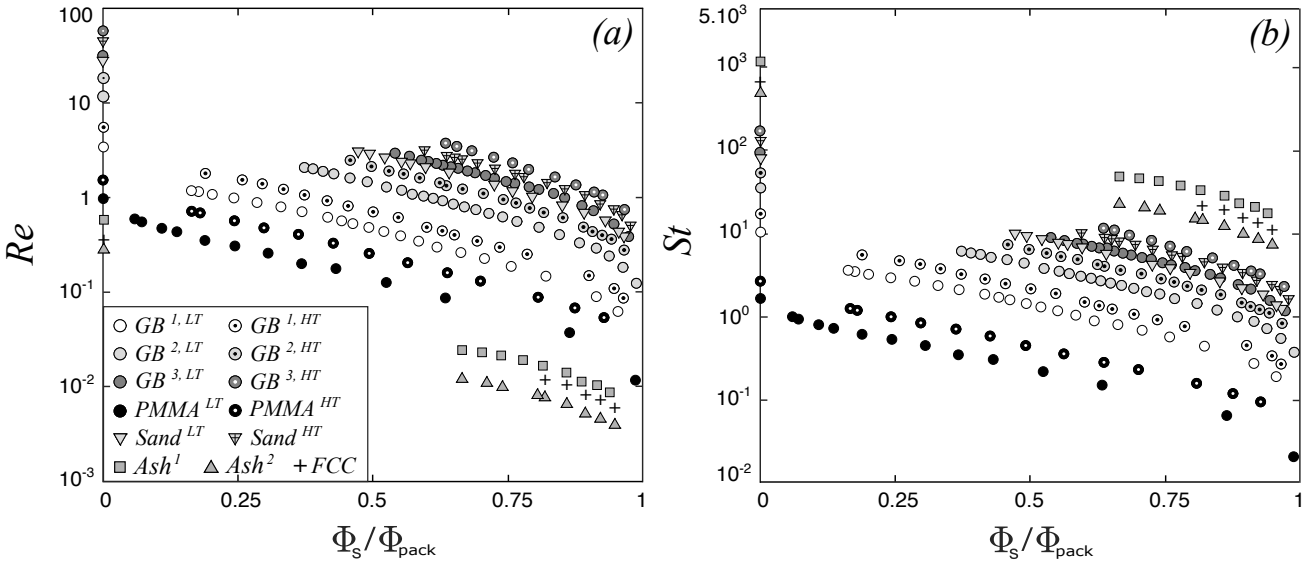

Figure 2.4

(a) Particles Reynolds number $\mathcal{R}e$ and (b) Stokes number $\mathcal{S}t$ as a function of Φ_s/Φ_{pack}.

However, since $\mathcal{A}r$ and $\mathcal{S}t_0$ are based on the Stokes velocity U_0 of an isolated settling particle, it is not straightforward to determine the flow regime within a concentrated suspension from their values. This can be better done by examining the Reynolds number Re and the Stokes number $\mathcal{S}t$ which are based on the actual velocity U corresponding to each concentration. Figure 2.4 shows the evolution of Re and $\mathcal{S}t$ with the normalized concentration. For comparison purposes, the value of $\mathcal{A}r$ (respectively $\mathcal{S}t$) corresponding to each fluid-and-particle system are reported at $\frac{\Phi_s}{\Phi_{pack}} = 0$ in fig. 2.4a (respectively in fig. 2.4b).

The maximal value of Re, which is reached for the largest glass beads in water at 35^{o}C and at a concentration $\frac{\Phi_s}{\Phi_{pack}}$ around 0.6, is about 4. The classic Schiller and Nauman correlation Clift *et al.* (1978) predicts that the terminal velocity of a solid sphere falling at $Re = 4$ is only decreased by 17% compared to the case at Re=0. Furthermore, it must be taken into account that the particles are not isolated, but immersed in a suspension whose effective viscosity μ_m is higher than that of the suspending fluid. As we will see later in this paper, μ_m/μ_f is about 10, which leads to an effective particle Reynolds number

less than 0.4 and a velocity decrease from the Stokes value by less than 4%. However, we will observe, in the limit of small concentrations, a reduction of the sedimentation or fluidization velocity relative to the Stokes velocity by a factor of 3 for the cases at the lowest Reynolds number (Re=0.004). In these experiments, it is therefore reasonable to conclude that fluid inertia plays a minor role regarding the fluidization or sedimentation velocity. We will thus disregard the Archimedes number in our analysis of the results

Varying the particle-to-fluid density ratio from 1.2, for PMMA particles in water, to more than 2000, for ash particles in hot air, allows us to investigate an unprecedented range of Stokes numbers ($1.6 \leq St_0 \leq 1200$, $0.015 \leq St \leq 70$) while keeping a low Reynolds number. Little is known about the effect of the Stokes number on the fluidization or sedimentation velocity, so that it is difficult to foresee whether this range is large enough to reveal the whole evolution of $U(St_0)$. It is indeed one of the main objective of this work to investigate this effect in situations where the fluid inertia plays a negligible role.

In the following, we will therefore examine the data by considering the three non-dimensional groups : $\mathcal{S}t_0$, Φ_s and Φ_{pack}. This choice will be proved to be relevant since all data can be modeled by accounting for these only three parameters.

2.4 Discussion of existing laws

In this section, we confront the two classical approaches with our results. We begin with that of Abrahamsen and Geldart. Fig. 2.5 compares the predictions of eq. 2.2 with experimental results. Eq. 2.2 involves a free parameter that is the minimum fluidization velocity U_{mf} for which we used the value of U_f measured at Φ_{up}, so that experiments and predictions necessarily match at this concentration. For particles in gas, Eq. 2.2 follows rather the evolution of U at high concentrations. However, it fails at low concentrations and is clearly not suitable for particles in water. Therefore, we do not think that this approach is relevant to gather the data, obtained from configurations of contrasted properties, into a unique description.

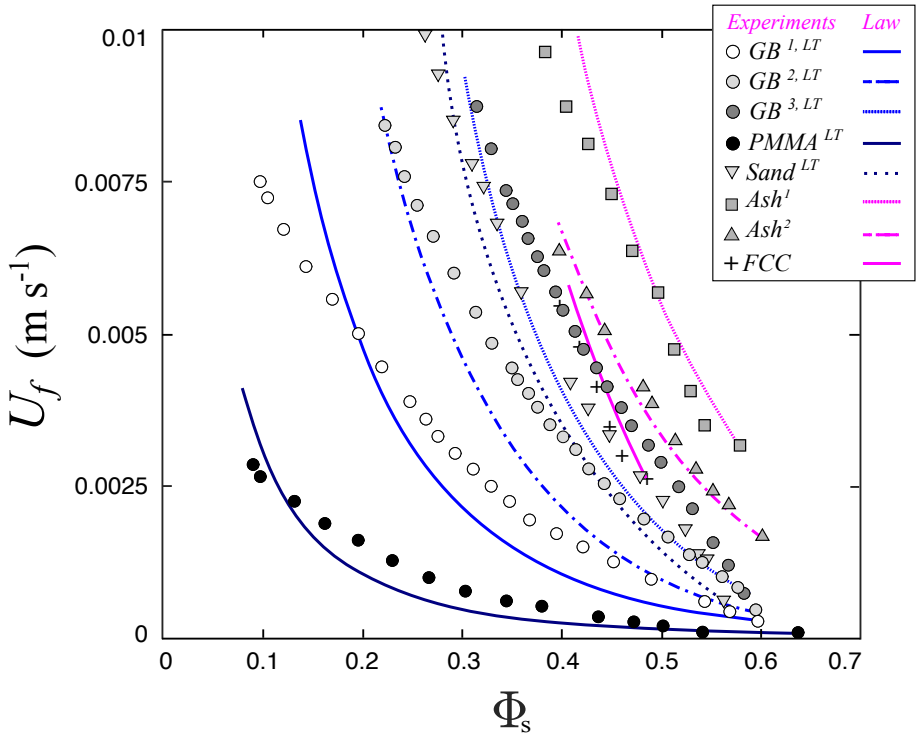

Figure 2.5

Fluidization velocity U_f as a function of the particle volume fraction Φ_s. Plain lines represent the Abrahamsen-Geldart's Abrahamsen & Geldart (1980) (Eq. 2.2) prediction for both the liquid-solid and the gas-solid suspensions.

Now we examine the popular approach of Richardson and Zaki. Eq. 2.6 involves two parameters : velocity U_i and exponent n. As it is usually done, the experimental results have been represented in Fig. 2.6a under the form $\log_{10}(\frac{U}{U_i})$ as a function of $\log_{10}(1-\Phi_s)$. The value of U_i corresponding to each experimental system has been determined such that the extrapolation of the best fit of the data by Eq. 2.6 intercepts $\frac{U}{U_i}=1$ at $\Phi_s=0$. Fig. 2.6a shows that the data of all systems gather on a straight line of slope $n=3.75$ within values of $\log_{10}(1-\Phi_s)$ ranged from approximately -0.3 to -0.05. This exponent is expected to depend on the Reynolds number. Since the exponent turns out to be the same for all considered systems, which include some cases at very low Re, the value found here should correspond to the low-Re limit. However, the present value $n=3.75$ is significantly lower than the low-Re value $n=4.65$ proposed by Richardson and Zaki. This is nevertheless not so surprising since, as pointed by Kramer *et al.* (2019), various exponents have been reported in the literature. Fig. 2.6b shows the values of U_i, normalized by the Stokes velocity U_0 of an isolated settling particle, as a function of $\mathcal{S}t_0$. They are observed to vary from 0.3 U_0 to $0.6U_0$ depending on the system under consideration. According to Richardson and Zaki, U_i can be affected by the column dimension or the Reynolds number. Here the ratio x_0/d between the minimum column side and the particle diameter is between 600 and 3000, which is enough to ensure that the results are independent of this parameter. By the way, it is worth mentioning that the existence of a dependence of U on the column dimension is incompatible with the homogeneity of the flow in the transverse direction. Regarding the Reynolds number, we note that the gas cases show the largest deviations to the Stokes velocity although they correspond to the lowest Re, which is much less than unity. On the other hand, $\frac{U_i}{U_0}$ can be described as a regular monotonous function of St_0, which indicates that, in agreement with the flow regime characterization presented in the previous section, particle inertia is the main cause of discrepancy between the various systems. Yet, the inertia of a particle does not affect its motion when moving at a constant speed. It is thus clear that the value of U_i that allows the results to gather do not correspond to the velocity of an isolated particle. To conclude, the Richardson-Zaki

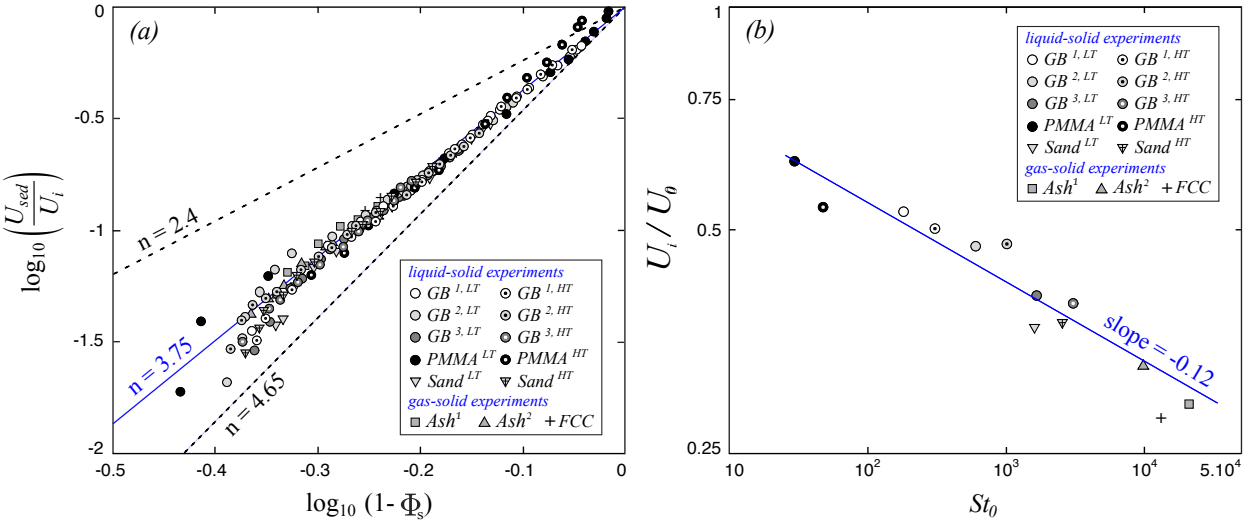

Figure 2.6

Presentation of the experimental results according to the Richardson and Zaki approach Richardson & D (1954) (Eq. 2.1). (a) Decimal logarithm of the sedimentation velocity, $\log_{10}\left(\frac{U_{sed}}{U_i}\right)$, as a function of that of the bed porosity $\log_{10}(1-\Phi_s)$. The dashed lines correspond to exponents $n = 4.65$ of the low-Re regime and $n = 2.4$ of the high-Re regime. (b) Velocity U_i normalized by the Stokes velocity U_0 as function of the Stokes number $\mathcal{S}t_0$.

approach, with an appropriate value of n and a value of U_i which depends on St_0, allows us to model the present results, provided that we renounce to describe the evolution of U at too small or large concentrations.

2.5 A more universal approach

Our objective is to gather the results obtained for all systems of materials over the entire homogeneous regime. We reconsider the idea presented in our previous study Girolami & Risso (2019) that dealt with solid particles in a gas and thus was limited to high Stokes numbers. Let us consider that the mixture of fluid and particles seen by an individual test particle of diameter d can be considered as a homogeneous fluid of density ρ_m and viscosity $\mu_m = \mu^* \mu_f$. The force balance on a test spherical particle settling at

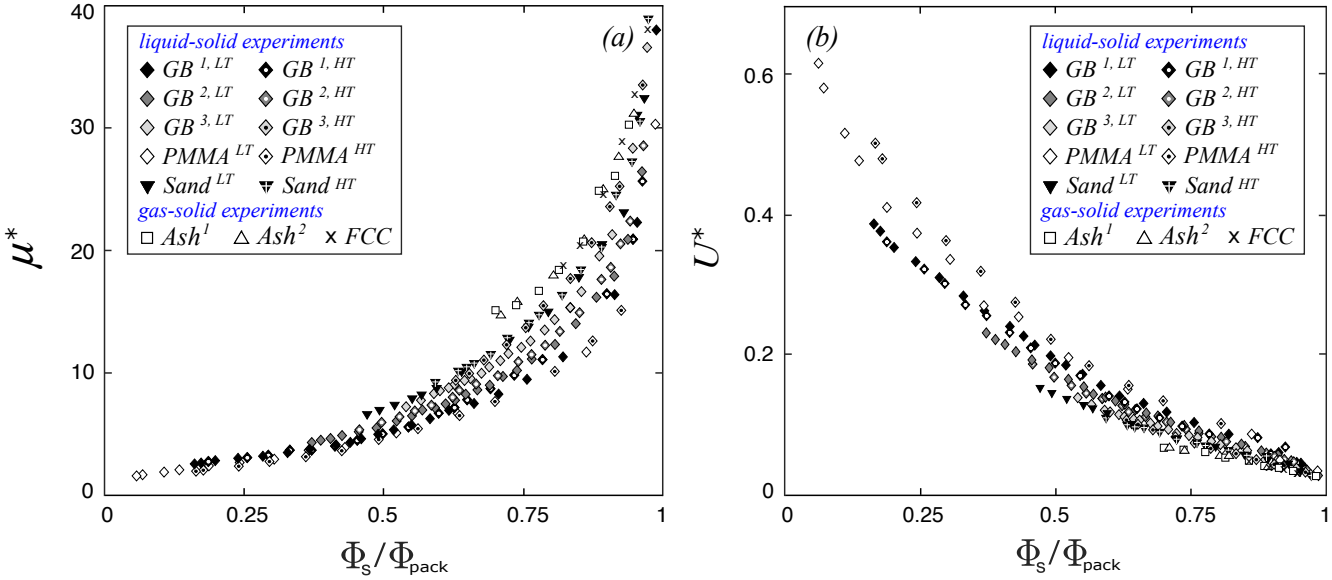

Figure 2.7

Experimental results on the non-dimensional form $\mu^* = \frac{U_0}{U(1-\Phi_s)}$ or $U^* = \frac{U(1-\Phi_s)}{U_0}$ as a function of $\frac{\Phi_s}{\Phi_{pack}}$.

velocity U under the action of gravity within in this fluid is, in the regime of negligible fluid inertia,

$$\frac{\pi d^3}{6}(\rho_p - \rho_m)g = 3\pi\mu^*\mu_f dU\,. \tag{2.5}$$

Knowing that the mixture density is of $\rho_m = \Phi_s\rho_p + (1-\Phi_s)\rho_f$ and introducing the Stokes velocity U_0 of an isolated particle (Eq. 2.4), leads to

$$\frac{U_0(1-\Phi_s)}{U} = \mu^*\left(\mathcal{S}t_0, \Phi_s, \frac{\Phi_s}{\Phi_{pack}}\right)\,. \tag{2.6}$$

This non-dimensional number a priori depends on the three non-dimensional control parameters. It describes the excess of viscous friction acting on the test particle due to the presence of the other particles. It is therefore greater than unity. It tends towards one in the dilute limit and diverges towards infinity when Φ_s tends toward Φ_{pack}. It is also expected to increase with $\mathcal{S}t_0$ from what we saw in Fig. 2.6b.

Fig. 2.7 shows experimental values of the non-dimensional viscosity $\mu^* = \frac{U_0(1-\Phi_s)}{U}$, and its inverse the non-dimensional velocity $U^* = \frac{U}{U_0(1-\Phi_s)}$, as a function of $\frac{\Phi_s}{\Phi_{pack}}$. Even

if they contain the same information, these two representations are complementary. The evolution of μ^* emphasizes the differences between the various cases at large concentrations, while that of U^* highlights the differences at low concentration. Each system of materials is characterized by a specific value of the Stokes number $\mathcal{S}t_0$. We remark that the evolution of μ^* or U^* against $\frac{\Phi_s}{\Phi_{pack}}$ looks similar at all $\mathcal{S}t_0$. The only differences lie in their overall magnitude and the limit of stability of the homogeneous regime. The values of μ^* corresponding to solid particles in a gas are above the others and defined on a short range, whereas those corresponding to PMMA particles in water are below and defined on a very broad range. Comparing all systems, we can claim that the smaller $\mathcal{S}t_0$, the smaller μ^* and Φ_{low}. A closer look reveals that, over their definition range, the curves are proportional and only differ by a factor, which depends only on $\mathcal{S}t_0$. It means that there exist a function $\mathcal{K}(\mathcal{S}t_0)$ so that the evolutions of $\frac{\mu^*}{\mathcal{K}}$ can be described by a unique function of $\frac{\Phi_s}{\Phi_{pack}}$. The expression of μ^* thus simplifies into

$$\mu^* \left(\mathcal{S}t_0, \Phi_s, \Phi_{pack}\right) = \mathcal{K}\left(\mathcal{S}t_0\right) \mathcal{F}\left(\frac{\Phi_s}{\Phi_{pack}}\right) , \tag{2.7}$$

where the Stokes number and the concentration are now involved in two separate functions, and where Φ_s and Φ_{pack} only appear through their ratio. The experimental values of $\mathcal{K}$ are easily determined from the data. Since it does not depend on the concentration, we can chose any given value Φ^* of $\frac{\phi_s}{\phi_{pack}}$ to calculate them. The ith value is given by

$$\mathcal{K}(\mathcal{S}t_0^i) = c\, \frac{\mu^* \left(\mathcal{S}t_0^i, \Phi^*\right)}{\mu^* \left(\mathcal{S}t_0^1, \Phi^*\right)} , \tag{2.8}$$

where c is a constant that can be arbitrarily included in $\mathcal{K}$ or $\mathcal{F}$ without changing their product, and thus without changing the value of μ^* according to Eq. 2.7. We choose the value of c so that $\mathcal{F}$ tends towards unity when $\left(\frac{\Phi_s}{\Phi_{pack}}\right)$ tends toward zero. Fig. 2.8 represents the experimental data in the form of $\mathcal{F}\left(\frac{\Phi_s}{\Phi_{pack}}\right)$. The corresponding values of $\mathcal{K}(\mathcal{S}t_0)$, obtained by using Eq. 2.8, are shown in Fig. 2.9.

The excellent collapse of all data into a unique master curve seen in Fig. 2.8 proves the validity of the simple model expressed by Eq. 2.7. In the absence of a theory predicting

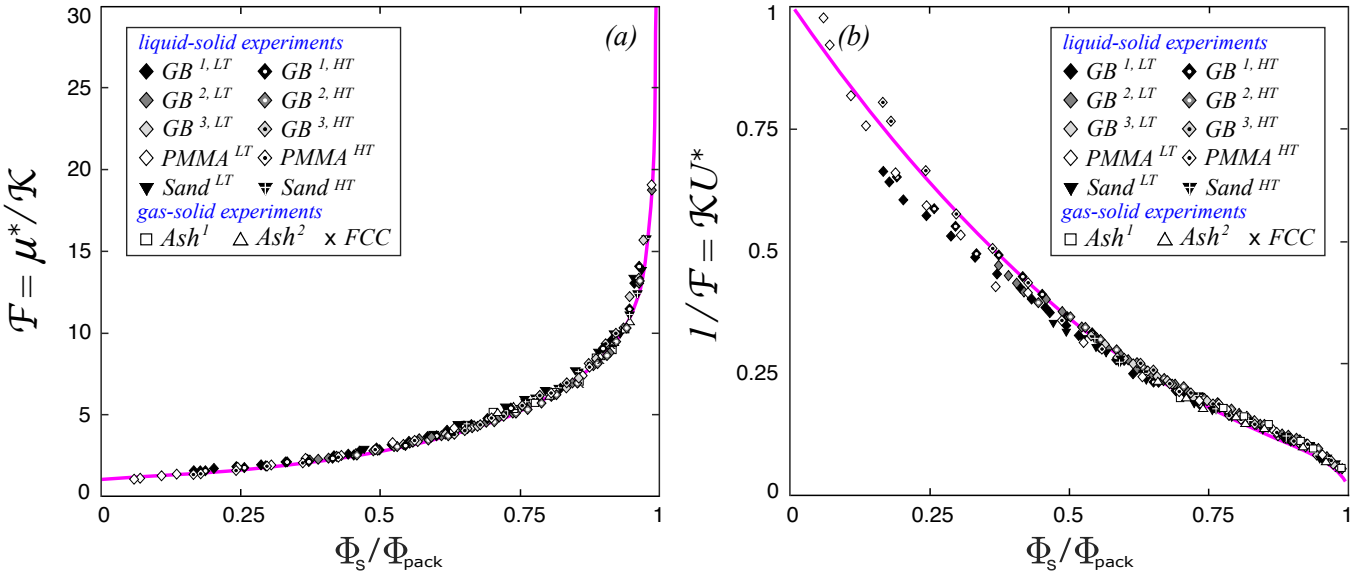

Figure 2.8

Non-dimensional function $\mathcal{F}\left(\frac{\Phi_s}{\Phi_{pack}}\right) = \frac{\mu^*}{\mathcal{K}(\mathcal{S}t_0)}$, which reflects the dependence of U on the concentration due to the enhanced viscous dissipation in the presence of many particles. Symbols represent experiments, the pink curve shows empirical law 2.9.

the function $\mathcal{F}$, it is interesting to search for an empirical expression. It turns out that it cannot be accurately described by either a power law or an exponential function. In fact, the low concentration range shows an exponential increase, whereas the divergence at high concentration is well described by a power law. These considerations lead us to propose an expression of the form

$$\mathcal{F}\left(\frac{\Phi_s}{\Phi_{pack}}\right) = C_0\left(\exp\left[-C_1\left(1-\frac{\Phi_s}{\Phi_{pack}}\right)\right] + C_2\left(1-\frac{\Phi_s}{\Phi_{pack}}\right)^{-C_3}\right), \tag{2.9}$$

where the constants C_i are positive numbers and $C_0 = \frac{1}{\exp(-C_1)+C_2}$. This expression satisfies the two conditions $\mathcal{F}(0) = 1$ and $\mathcal{F}(1) = \infty$. The best fit is obtained with $C_1 = 3$, $C_2 = 0.08$ and $C_3 = 2/3$. It is represented by the pink curve in Fig. 2.8 and accurately describes the experimental results.

The evolution of $\mathcal{K}$ against $\mathcal{S}t_0$, plotted in Fig. 2.9, reveals the effect of the particle inertia on the fluidization or sedimentation velocity. The experimental results show that

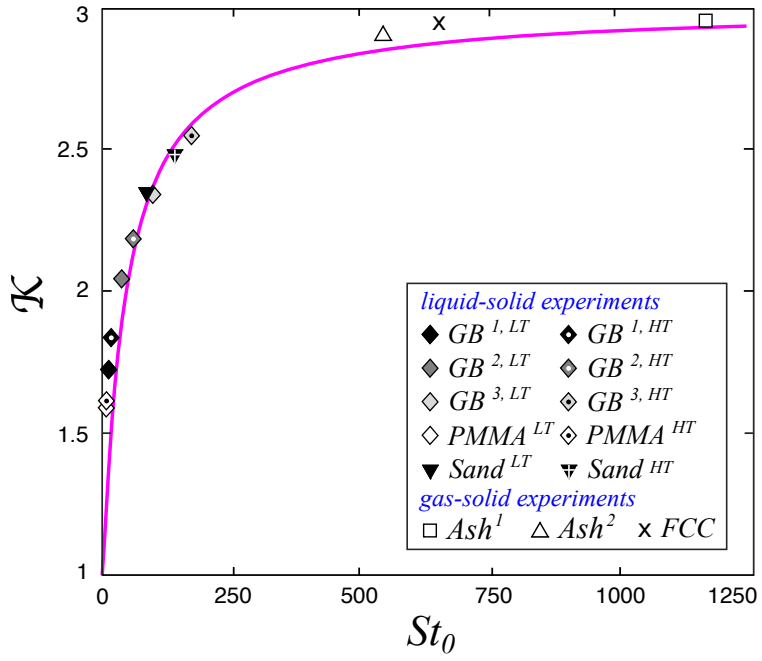

Figure 2.9

Non-dimensional function $\mathcal{K}(\mathcal{S}t_0)$, which reflects the increase of viscous dissipation due to the difference between instantaneous motions between inertial particles and the carrier fluid. Symbols represent experiments, the pink curve shows empirical law 2.10.

$\mathcal{K}(\mathcal{S}t_0)$ is an increasing function, with a slope that is large at low $\mathcal{S}t_0$ but then decreases continuously as $\mathcal{S}t_0$ increases, finally reaching a plateau at high $\mathcal{S}t_0$. Such a behavior can be described by means of a simple saturation function of the form

$$\mathcal{K}\left(\mathcal{S}t_0\right) = \left(K_\infty - K_0\right) g\left(\mathcal{S}t_0\right) + K_0\,, \tag{2.10}$$

where K_0 and K_∞ are respectively the limits of $\mathcal{K}\left(\mathcal{S}t_0\right)$ at zero and infinity.

$$g(x) = \frac{x}{x+1}\,, \tag{2.11}$$

where $x = \frac{\mathcal{S}t_0}{\mathcal{S}t_{0c}}$, $\mathcal{S}t_{0c}$ characterizing the rate at which transition between small and large $\mathcal{S}t_0$ regimes occurs. Now recall that the smaller $\mathcal{S}t_0$, the smaller Φ_{low}. With light particles, dilutions strong enough for U to approach U_0 can be achieved while remaining in the homogeneous regime. Thus, if we stand that Φ_{low} tends towards zero when $\mathcal{S}t_0$ tends towards zero, we obtain from Eqs. 2.6 and 2.7

$$\mu^*\left(\mathcal{S}t_0 = 0, \frac{\Phi_{low}}{\Phi_{pack}}\right) = \mu^*\left(0,0\right) = K_0\mathcal{F}(0) = K_0 = \frac{U_0(1-0)}{U_0} = 1\,. \tag{2.12}$$

Given that $K_0 = 1$, K_∞ and $\mathcal{S}t_{0c}$ are the two remaining free parameters in Eq.2.10. A reasonable fit of the experimental results, shown by the pink curve in Fig. 2.9, is obtained by setting $K_\infty = 3$ and $\mathcal{S}t_{0c}$=45. (It can be mentioned that a slightly better fit of the experimental results is obtained with $K_0 = 1.5$, $K_\infty = 3$ and $\mathcal{S}t_{0c}$=70, but is not consistent with equation 2.12.)

We finally end up with a general model of the sedimentation/fluidization velocity U of a suspension that is valid all over the homogeneous range and for all systems of fluid and particles, provided that the inertia of the fluid can be neglected compared to viscous forces. From Eqs. 2.6 and 2.7, U can be written as a product of four terms

$$U = \underbrace{\frac{g(\rho_p - \rho_f)d^2}{18\,\mu_f}}_{\text{1. Isolated particle, } U_0} \underbrace{\left(1-\phi_s\right)}_{\text{2. mixture density}} \underbrace{\frac{1}{\mathcal{F}\left(\frac{\phi_s}{\phi_{pack}}\right)}}_{\text{3.bed porosity, Eq. 2.9}} \underbrace{\frac{1}{\mathcal{K}\left(\mathcal{S}t_0\right)}}_{\text{4. particle agitation, Eq. 2.10}}\,, \tag{2.13}$$

which can be interpreted as follows :

1. The first term is the theoretical Stokes terminal velocity U_0 of an isolated sphere of density ρ_p settling under the action of gravity in a fluid of density ρ_f and viscosity μ_f. It is the value reached by U when both $\Phi_s = 0$ and $\mathcal{S}t_0 = 0$. The three other terms are non-dimensional corrections to U_0 accounting for the various effects associated with the presence of many particles.

2. The second term simply accounts for the evolution of the density ρ_m of the mixture which affects the buoyancy force acting on each solid particle in Eq. 2.5. As noticed in Girolami & Risso (2019), Eq. 2.5 can also be obtained by considering a test particle moving at velocity $\frac{U}{1-\Phi_s}$ relative to the fluid of density ρ_f instead of moving at velocity U relative to the mixture of particles and fluid at density ρ_m. Thus, the second term can also be interpreted as reflecting the increase of the relative velocity between the particle and the fluid when the concentration increases. It is worth mentioning that this term is not associated with interactions between particles nor with an increase of the drag force acting on the particles.

3. As well as in a porous medium, the fluid follows complex paths within the interstices between the particles. The friction on each particle and the corresponding viscous dissipation are therefore increased compared to the case of an isolated particle. This causes the increase of the average drag force on the particle and the decrease of U. The third term of Eq. 2.13, modeled by Eq. 2.9, quantifies this effect in the case of particles of negligible inertia, i.e. $\mathcal{S}t_0 = 0$. Function $\frac{1}{\mathcal{F}}$ decreases from unity to zero as $\frac{\phi_s}{\phi_{pack}}$ goes from zero (isolated particle) to one (packed state).

4. In fluidized beds or sedimenting suspensions, both fluid and particle velocities undergo fluctuations, even at low Reynolds number Nguyen & Ladd (2005); Abbas *et al.* (2006). These fluctuations contribute to the dissipation of mechanical energy and thus affect the average velocity U. In particular, the fluctuations of the relative velocity between the fluid and the particles are intimately related to how U depends on the concentration Alméras *et al.* (2019). However, these fluc-

tuations do not only depend on the concentration but also on the Stokes number. Particles of negligible inertia ($\mathcal{S}t_0 \ll 1$) instantaneously follow any local fluctuations of the fluid that surrounds them, while particles of significant inertia follow trajectories that differ from those of the fluid. For particles of negligible inertia, the effect of the fluctuations is already embedded in $\frac{1}{\mathcal{F}}$ and turns out to vanish at strong dilution. The fourth term of Eq. 2.13, modeled by Eq. 2.10, describes the evolution of this effect with the Stokes number. It turns out that $\frac{1}{\mathcal{K}}$ is a decreasing function of $\mathcal{S}t_0$ which reaches a minimum value of about 1/3 at large $\mathcal{S}t_0$. The larger $\mathcal{S}t_0$, the smaller U, which is at most three times smaller for high-inertia particles compared to low-inertia ones.

2.6 Boundaries of the homogeneous range

Eq. 2.13 provides a general relation between U and all the control parameters of the problem. To achieve a complete description, we need henceforth to determine the boundaries of the homogeneous range in which this law is valid.

Fig. 2.10a shows the upper boundary, $\frac{\Phi_{up}}{\Phi_{pack}}$, as a function of $\mathcal{S}t_0$. Note that Φ_{up} is defined as the maximum concentration below which the bed of particles is fully fluidized, i.e. $U_f = U_{sed}$. In principle, this point may differ from the concentration Φ_{mf} corresponding to the minimum fluidization velocity, where the presence of the wall can still play a significant role and cause U_f to be larger than U_{sed}. However, it turned out that U_f was approximately equal to U_{sed} at the first point where measurable expansion was detected. We can thus make no distinction between Φ_{up} and Φ_{mf} in the present experiments. This is not surprising since the ratio between Φ_{up} and Φ_{pack} remains in any case ranged from 0.94 and 1, without showing any clear correlation with $\mathcal{S}t_0$.

The study of the lower boundary Φ_{low} is much more interesting, since it characterizes the limit of stability of the homogeneous regime when the concentration is decreased as well as the bed expansion. Above Φ_{low}, the bed shows no noticeable fluctuations.

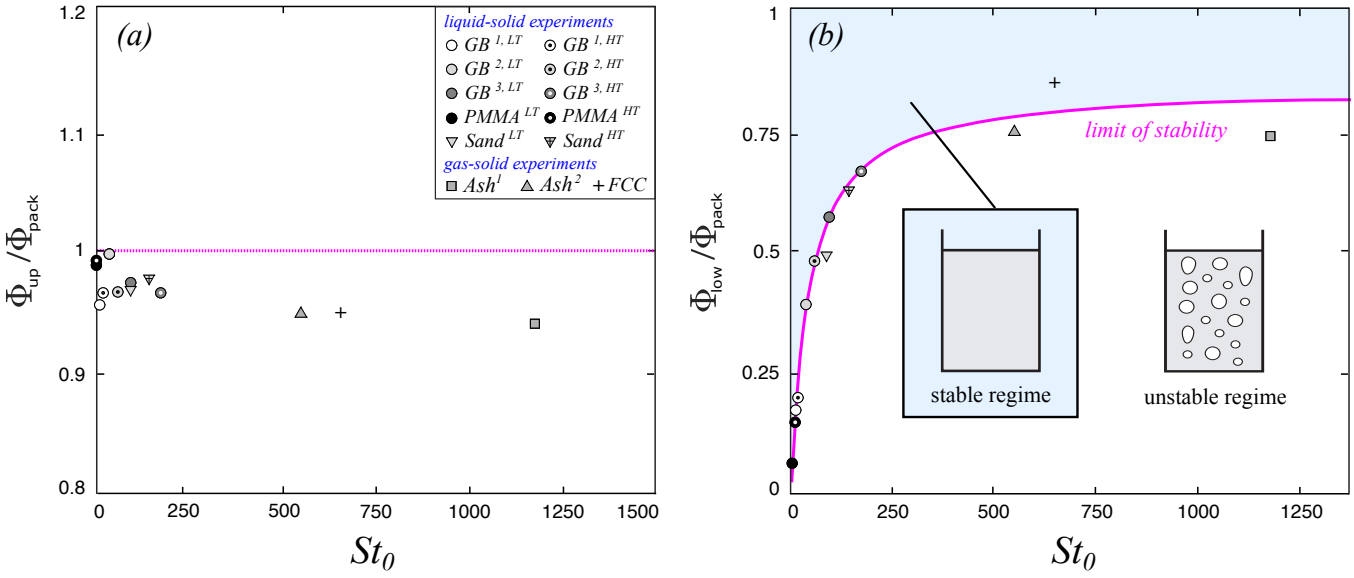

Figure 2.10

Boundaries of the homogeneous range at a function of $\mathcal{S}t_0$. (a) Upper limit $\left(\frac{\phi_{up}}{\phi_{pack}}\right)$ determined from the minimum fluidization velocity; (b) lower limit $\left(\frac{\phi_{low}}{\phi_{pack}}\right)$ corresponding to the onset of the bed instability.

Below Φ_{low} the surface of the bed becomes strongly agitated and visible fluctuations of concentration at large scales compared to d are visible. Fig. 2.10b shows $\frac{\Phi_{low}}{\Phi_{pack}}$ as a function of $\mathcal{S}t_0$. It is immediately noticeable that this behavior is similar to that of $\mathcal{K}\left(\mathcal{S}t_0\right)$ presented in Fig. 2.9 and can thus be described by an expression similar to Eq. 2.10,

$$\frac{\Phi_{low}}{\Phi_{pack}}\left(\mathcal{S}t_0\right) = \left(\left[\frac{\Phi_{low}}{\Phi_{pack}}\right]_{\infty} - \left[\frac{\Phi_{low}}{\Phi_{pack}}\right]_{0}\right) g\left(\mathcal{S}t_0\right) + \left[\frac{\Phi_{low}}{\Phi_{pack}}\right]_{0}, \tag{2.14}$$

where function g is still given by Eq. 2.11 with $\mathcal{S}t_{0c}$=45. The best fit of the experimental results, given by $\left[\frac{\Phi_{low}}{\Phi_{pack}}\right]_0 = 0$ and $\left[\frac{\Phi_{low}}{\Phi_{pack}}\right]_{\infty} = 0.8$, is represented by the pink curve in Fig. 2.10b. Considered together, the evolutions of $\mathcal{K}\left(\mathcal{S}t_0\right)$ and $\frac{\Phi_{low}}{\Phi_{pack}}\left(\mathcal{S}t_0\right)$ draw an interesting picture. First, it is worth recalling that $\left[\frac{\Phi_{low}}{\Phi_{pack}}\right]_0 = 0$ means that a bed of particles of negligible inertia should be expanded without limit while remaining homogeneous. At $\mathcal{S}t_0 = 0$, there is no discontinuity between the case of an isolated particle ($\Phi_s = 0$) and the onset of the transition towards jamming ($\Phi_s = \Phi_{pack}$), U being determined by the three first terms of Eq. 2.13. At $\mathcal{S}t_0 > 0$, the velocity U is divided by a factor $\mathcal{K}\left(\mathcal{S}t_0\right) > 1$

and, concurrently, the homogeneous regime is restricted to concentrations larger than $\Phi_{low}\left(\mathcal{S}t_0\right) > 0$. In this case, the existence of a bifurcation at Φ_{low} limits the evolution of U that cannot be extrapolated towards $\Phi_s = 0$ to recover the value U_0 corresponding to an isolated particle. Increasing $\mathcal{S}t_0$ leads to the increase of $\mathcal{K}$ and $\frac{\Phi_{low}}{\Phi_{pack}}$ by following a similar law, which indicates that the same mechanism related to the inertia of the particles is responsible for both the instability of the suspension and the decrease of U.

2.7 Conclusion

From a thorough examination of experimental results conducted with systems of contrasted properties, we have established a general law (Eq. 2.13) for the sedimentation/fluidization velocity U of a non-cohesive suspension of particles in a low-inertia fluid, either gaseous or liquid. This law takes into account all the physical parameters that control the flow. It is valid over the whole range of particle volume fractions where a fully fluidized homogeneous suspension is stable, between the lower limit Φ_{low} below which large-scale fluctuations of concentration develop, and the upper limit Φ_{up} above which solid friction starts to play a significant role. A major finding of this work is that the expression of U can be decomposed into the product of four terms, each of them accounting for a different physical mechanism : (1) the settling velocity of an isolated particle, (2) the effective particle weight, (3) the effect of the concentration of particles of negligible inertia (4) the effect of particle inertia. Remarkably, the function $\mathcal{F}\left(\frac{\Phi_s}{\Phi_{pack}}\right)$ modeling term (3) is independent of function $\mathcal{K}\left(\mathcal{S}t_0\right)$ modeling term (4). Also, the flow instability beyond a given concentration is directly related to the inertia of the particles. A bed of inertialess particles ($\mathcal{S}t_0 = 0$) can be indefinitely expanded while remaining stable. Increasing $\mathcal{S}t_0$, $\frac{\Phi_{low}}{\Phi_{pack}}$ and $\mathcal{K}\left(\mathcal{S}t_0\right)$ both increase by following the same law. Thus, the larger the Stokes number, the lower U and the less the maximum stable bed expansion.

Combined to general expression 2.13, empirical laws 2.9, 2.10 and 2.14 provide a reliable tool for engineers needing to predict the behavior of a fluidized bed. Note that

this expression is valid in the homogeneous regime and cannot be extrapolated to values of Φ_s that are lower than Φ_{low}.

Now, let us discuss two possible limitations of the present result. We can wonder whether there could be an effect of the width of the size distribution. Although the particle sets investigated in a liquid (Fig. 2.2) as well as those investigated in a gas (Fig. 1 of Girolami *et al.* (2015), Girolami & Risso (2019)) have various size distributions, our model is able to describe them by only accounting for the average diameter of the particles. We thus think that the particle distribution can be disregarded, provided that its width is narrow enough to prevent size segregation from occurring Chen & Keairns (1975). Note that the mixture was made with the same material and also prevents the density segregation. Moreover, in experiments made in gas, one set of roughly spherical FCC particles and two sets of non-spherical randomly shaped volcanic ash were studied (see pictures in Fig. 1 of Girolami *et al.* (2015), Girolami & Risso (2019)). In experiments made in liquid, glass beads and PMMA particles are spherical, whereas sand grains are not (see pictures in Fig. 2.2). Since the present model is found to work with all the considered materials, it seems that Φ_{pack} embeds the most important information about the particle shape, at least for shapes that are moderately anisotropic.

Lastly, it is important to recall that the present model described situations where the effect of the fluid inertia can be neglected, i.e. small Reynolds numbers. To deal with all possible cases, a model must provide the dependence of U with all four non-dimensional parameters : Φ_s and Φ_{pack}, St_0 and Ar. Is it possible to extend the present model to include the Archimedes number ? A more general expression for the velocity of the isolated particle (term 1) could be considered in oder to account for a finite-Reynolds-number drag. Also, the effect of the concentration on the mixture density (term 2) should remain unchanged. However, it is more difficult to anticipate about the two other terms. In particular, it would be interesting to know whether a separation of variables as that expressed by Eq. 2.7 is still relevant when the role of Ar is considered. A Future work based on further experimental investigations will address these issues.

Acknowledgment

This study was supported by the Region Centre-Val de Loire (Contribution of 'Academic Initiative' : MAGIC/201500103985). LG particularly thanks Romain Morini and Stephane Moreau (AVILEX) for their contribution to experiments.

Bibliographie

Abbas, M., Climent, E., Simonin, O. & Maxey, M. R. 2006 Dynamics of bidisperse suspensions under Stokes flows : Linear shear flow and sedimentation. *Physics Of Fluids* **18** (12), 121504.

Abbas, M., Pouplin, A., Masbernat, O., Liné, A. & Décarre, S. 2017 Pipe flow of a dense emulsion : Homogeneous shear-thinning or shear-induced migration ? *AIChE J.* **63** (11), 5182–5195.

Abrahamsen, A. R. & Geldart, D. 1980 Behaviour of gas-fluidized beds of fine powders part I. Homogeneous expansion. *Powder Technology* **26** (1), 35–46.

Alméras, E., Masbernat, O., Risso, F. & Fox, R. O. 2019 Fluctuations in inertial dense homogeneous suspensions. *Physical Review Fluids* **4** (10), 102301.

Amin, A., Girolami, L. & Risso, F. 2021 On the fluidization/sedimentation velocity of a homogeneous suspension in a low-inertia fluid. *Powder Tech.* **391**, 1–10.

Bargieł, M. & Tory, E. M. 2013 Extension of the Richardson–Zaki equation to suspensions of multisized irregular particles. *International Journal of Mineral Processing* **120**, 22–25.

Batchelor, G. K. 1967 *An introduction to fluid dynamics*. Cambridge University Press.

Briceño, M. & Joseph, D. 2003 Self-lubricated transport of aqueous foams in horizontal conduits. *Int. J. Multiphase Flow* **29** (12), 1817–1831.

Chen, J. L. P. & Keairns, D. L. 1975 Particle segregation in a fluidized bed. *The Canadian Journal of Chemical Engineering* **53** (4), 395–402.

Clift, R., Grace, J. & Weber, M. 1978 *Bubble, Drops and Particles*. Academic Press.

du Cluzeau, A., Bois, G. & Toutant, A. 2019 Analysis and modelling of Reynolds stresses in turbulent bubbly up-flows from direct numerical simulations. *J. Fluid Mech.* **866**, 132–168.

Einstein, A. 1906 Eine neue bestimmung der moleküldimensionen. *Ann. Phys.* **19**, 289–306.

Einstein, A. 1911 Berichtigung zu meiner arbeit : Eine neue bestimmung der moleküldimensionen. *Ann. Phys.* **34**, 591–592.

Ergun, S. 1952 Fluid flow through packed colmuns. *Chemical Engineering Progress* **48** (2), 89–94.

Funamizu, N. & Takakuwa, T. 1995 An improved Richardson-Zaki formula for computing mixed layer composition in binary solid-liquid fluidized beds. *Chemical Engineering Science* **50** (19), 3025–3032.

Girolami, L. 2008 Dynamique et sédimentation des écoulements pyroclastiques reproduits en laboratoire. PhD thesis, Université de Clermont II.

Girolami, L., Druitt, T. H. & Roche, O. 2015 Towards a quantitative understanding of pyroclastic flows : Effects of expansion on the dynamics of laboratory fluidized granular flows. *Journal of Volcanology and Geothermal Research* (296), 31–39.

Girolami, L. & Risso, F. 2019 Sedimentation of gas-fluidized particles with random shape and size. *Physical Review Fluids* **4** (7), 074301.

Girolami, L. & Risso, F. 2020 Physical modeling of the dam-break flow of sedimenting suspensions. *Physical Review Fluids* **5** (8), 084306.

Guazzelli, É. & Pouliquen, O. 2018*a* Rheology of dense granular suspensions. *Journal of Fluid Mechanics* **852**, 35–73.

Guazzelli, E. & Pouliquen, O. 2018*b* Rheology of dense granular suspensions. *J. Fluid Mech.* **852**, 35–73.

Hinch, E. J. 1977*a* An averaged-equation approach to particle interactions in a fluid suspension. *Journal of Fluid Mechanics* **83** (4), 695–720.

Hinch, E. J. 1977*b* An averaged-equation approach to particle interactions in a fluid suspension. *J. Fluid Mech.* **83** (4), 695–720, publisher : Cambridge Univ Press.

Hooshyar, N., van Ommen, J. R., Hamersma, P. J., Sundaresan, S. & Mudde, R. F. 2013 Dynamics of Single Rising Bubbles in Neutrally Buoyant Liquid-Solid Suspensions. *Phys. Rev. Lett.* **110** (24), 244501.

Koo, S. 2008 Sedimentation velocity of bidisperse suspensions. *Journal of Industrial and Engineering Chemistry* **14** (5), 679–686.

Kramer, O. J. I., de Moel, P. J., Baars, E. T., van Vugt, W. H., Padding, J. T. & van der Hoek, J. P. 2019 Improvement of the Richardson-Zaki liquid-solid fluidisation model on the basis of hydraulics. *Powder Technology* **343**, 465–478.

Krieger, I. M. & Dougherty, T. J. 1959 A mechanism for non-Newtonian flow in suspensions of rigid spheres. *Transactions of the Society of Rheology* **3** (1), 137–152.

Lettieri, P., Newton, D. & Yates, J. G. 2002 Homogeneous bed expansion of FCC catalysts, influence of temperature on the parameters of the Richardson–Zaki equation. *Powder Technology* **123** (2-3), 221–231.

Lubchenko, N., Magolan, B., Sugrue, R. & Baglietto, E. 2018 A more fundamental wall lubrication force from turbulent dispersion regularization for multiphase CFD applications. *Int. J. Multiphase Flow* **98**, 36–44.

Nguyen, N.-Q. & Ladd, A. J. C. 2005 Sedimentation of hard-sphere suspensions at low Reynolds number. *Journal of Fluid Mechanics* **525**, 73–104.

Ovarlez, G., Bertrand, F. & Rodts, S. 2006 Local determination of the constitutive law of a dense suspension of noncolloidal particles through magnetic resonance imaging. *J. Rheol.* **50** (3), 259–292.

Popel, A. S. & Johnson, P. C. 2005 Microcirculation and hemology. *Annu. Rev. Fluid Mech.* **37** (1), 43–69.

Richardson, J. F. & D, W. N. Z. P. 1954 Sedimentation and fluidisation : Part I. *Trans. Inst. Chem. Eng.* **32**, S82–S100.

Richardson, J. F. & Zaki, W. N. 1954 The sedimentation of a suspension of uniform spheres under conditions of viscous flow. *Chemical Engineering Science* **3** (2), 65–73.

Roman, S., Lorthois, S., Duru, P. & Risso, F. 2012 Velocimetry of red blood cells in microvessels by the dual-slit method : Effect of velocity gradients. *Microvasc. Res.* **84** (3), 249–261.

Sharan, M. & Popel, A. S. 2001 A two-phase model for flow of blood in narrow tubes with increased effective viscosity near the wall. *Biorheology* **38**, 415–428.

Valverde, J. M. & Castellanos, A. 2008 A modified Richardson–Zaki equation for fluidization of Geldart B magnetic particles. *Powder Technology* **181** (3), 347–350.

Chapitre 3

Fall of a large sphere in a suspension of fluidized particles

by Ahmad Amin, Laurence Girolami, Frédéric Risso.

This chapter has been submitted to Physical Review Fluids – Letters.

Abstract

The investigation of the fall of a sphere in a concentrated suspension of small fluidized particles leads to unexpected results. By analyzing the drag force, it is shown that the shear stress on the sphere is controlled by the slip velocity of the particles relative to the sphere and an effective viscosity determined from the particle sedimentation velocity. Consequently, the drag force is independent of the structure of the flow away from the immediate vicinity of the sphere wall. This result questions rheological characterizations obtained from measurements of the efforts exerted on a wall.

3.1 Introduction

Suspensions, consisting of small particles dispersed in a fluid, are very common in nature (turbidity currents, pyroclastic flows, blood...) as well as in industry (food and cosmetic, fluidized beds...). A suspension is a complex two-phase mixture that is desirable to model as an equivalent fluid of effective density ρ_m and viscosity μ_m. The mixture density ρ_m is simply the average density of both phases weighted by their respective volume fraction. However, defining an effective viscosity μ_m for the mixture, always larger than the suspending-fluid viscosity μ_f, remains a challenge. Since the first attempt of Einstein (1906, 1911), numerous works have been devoted to this issue, mainly focused on sheared suspensions of neutrally buoyant solid particles with negligible inertia. This case has been thoroughly reviewed in Guazzelli & Pouliquen (2018*b*) for non-Brownian suspensions. Under these conditions, the stress τ within the mixture is linear with the shear rate $\dot{\gamma}$ and, for a given fluid-particle system, $\mu_\mathrm{m}/\mu_\mathrm{f}$ is only a function of the particle volume fraction Φ. This result may not hold with deformable particles, such as droplets in emulsions Abbas *et al.* (2017) or red cells in blood Popel & Johnson (2005), since their deformation is affected by the shear rate $\dot{\gamma}$ and thus $\mu_\mathrm{m}/\mu_\mathrm{f}$ may depend on it. As well, when inertia is no longer negligible, $\mu_\mathrm{m}/\mu_\mathrm{f}$ may depend on the local Reynolds number and vary with $\dot{\gamma}$.

The flow around an obstacle is known as a reference case from which the rheology of a fluid can be analyzed. However, it has rarely been applied to suspensions, with the notable exception of Hooshyar *et al.* (2013), where the rise of a bubble through a dispersion of neutrally buoyant particles was studied. The present work investigates the fall of a large solid sphere through a suspension of small beads in a liquid, with the aim of revealing the effective behavior of the suspension.

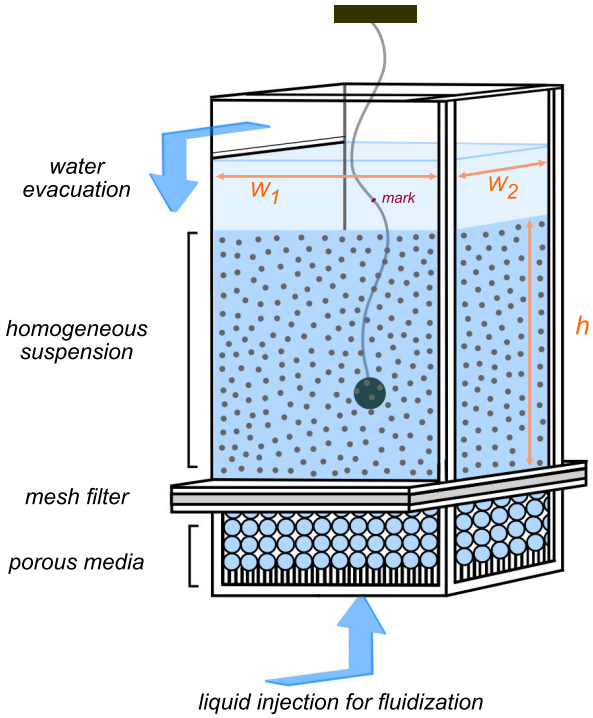

Figure 3.1

Scheme of the experimental setup.

3.2 Experimental setup and procedures

3.2.1 Fluidized suspensions

We consider dispersions of beads that are heavier than the liquid and maintained in suspension by imposing a weak upward flow. Using such a fluidized bed makes it possible to deal with buoyant particles and to easily control the volume fraction Φ by changing the fluidization velocity U_f. Here, U_f is taken in the range of the stable homogeneous fluidization regime, in which the particle distribution remains steady and uniform. The terminal velocity V_t of three large spheres of different diameters D is measured within four suspensions of different beads of diameters $d \ll D$, at concentrations Φ from 0.3 to 0.85.

The fluidization system is similar to that used in a previous work devoted to the study

Suspension properties	GB^1	GB^2	GB^3	*Sand*
Particle diameter d [μm]	160	240	335	310
Particle density ρ_d [kg m^{-3}]	2.50×10^3	2.50×10^3	2.50×10^3	2.66×10^3
Fluid density ρ_f [kg m^{-3}]	1.0×10^3	1.0×10^3	1.0×10^3	1.0×10^3
Fluid viscosity μ_f [Pa s]	1.15×10^{-3}	1.11×10^{-3}	1.11×10^{-3}	1.10×10^{-3}
$\mathcal{A}r = \frac{\rho_\mathrm{f}(\rho_p-\rho_\mathrm{f})gd^3}{18\mu_\mathrm{f}^2}$	3	11	31	28
$\mathcal{S}t_0 = \frac{(\rho_\mathrm{d}-\rho_\mathrm{f})(\rho_\mathrm{d}+\frac{1}{2}\rho_\mathrm{f})gd^3}{18\ \mu_\mathrm{f}^2}$	7.6	28	76	80

Table 3.1

Physical properties of the suspensions

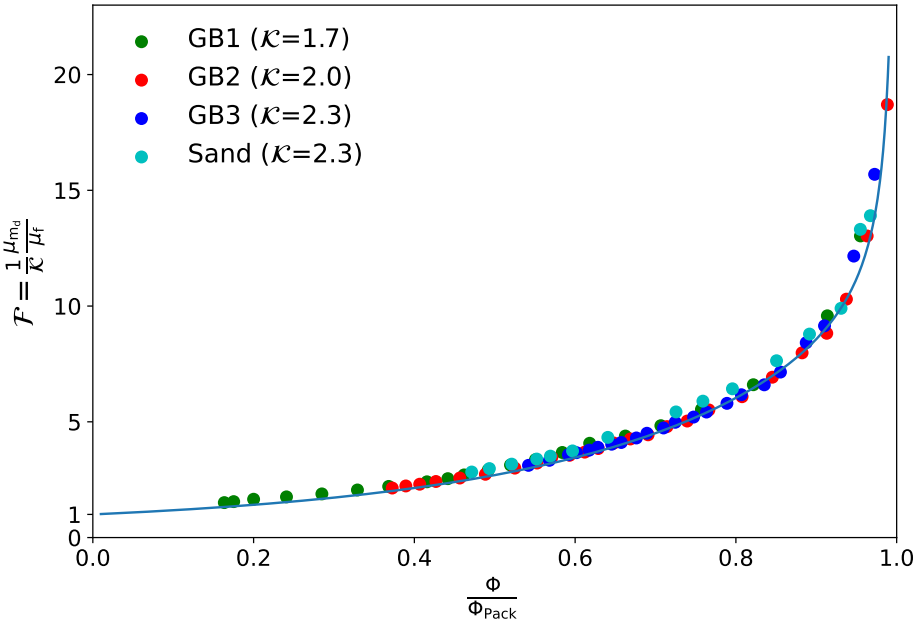

Figure 3.2

Mixture effective viscosity defined from the fluidization velocity of the suspension. Symbols : measurements. Line : model from Amin *et al.* (2021), taking $\mathcal{F}\left(\frac{\Phi_s}{\Phi_\mathrm{pack}}\right) = \frac{1}{(e^{-3}+0.08)}\left[e^{-3\left(1-\frac{\Phi_s}{\Phi_\mathrm{pack}}\right)} + 0.08\left(1-\frac{\Phi_s}{\Phi_\mathrm{pack}}\right)^{-2/3}\right]$.

of the fluidization and the sedimentation velocities of homogeneous suspensions Amin *et al.* (2021). The experimental setup is depicted in Fig. 3.1. The fluidization column has a rectangular cross-section of sides w_1=0.2 m and w_2=0.3 m. It is filled with a mixture of water and particles. In the absence of flow, the particles form a loose packed bed of height h_0 at a concentration $\Phi_{\rm pack}$ between 0.58 and 0.60. Then, water is injected from the bottom at a flow rate Q through a porous media, which ensures a uniform flow, and a mesh filter, which prevents the passage of particles. For a given fluidization velocity, $U_{\rm f} = Q/(w_1 w_2)$, the suspension expands up to reach a height h, corresponding to a concentration $\Phi/\Phi_{\rm pack} = h_0/h$. The properties of the suspensions are given in Table 3.1. We used three sets of spherical glass beads of different sizes (GB^1, GB^2, GB^3) and one set of natural sand grains. Following Girolami & Risso (2019); Amin *et al.* (2021), we introduce an effective viscosity of the suspension $\mu_{\rm m_d}$ determined from the fluidization velocity. Let's consider a spherical bead of diameter d and density $\rho_{\rm d}$ falling at velocity $U_{\rm f}$ into a fluid of viscosity $\mu_{\rm m_d}$ and density $\rho_{\rm m}$. Balancing the Stokes' drag, $3\pi\mu_{\rm m_d} d U_{\rm f}$, by the reduced weight of the bead, $\pi d^3/6(\rho_{\rm d} - \rho_{\rm m})g$, where g is the gravity acceleration and $(\rho_{\rm d} - \rho_{\rm m}) = (1-\Phi)(\rho_{\rm d} - \rho_{\rm f})$, yields

$$\frac{\mu_{\rm m_d}}{\mu_{\rm f}} = \frac{g(\rho_{\rm d} - \rho_{\rm f})(1-\Phi)d^2}{18\mu_f U_{\rm f}}. \tag{3.1}$$

From the analysis of many fluid-particle systems, it has been shown in Amin *et al.* (2021) that, provided that the fluid inertia is negligible, the fluidization velocity of a suspension can be modeled as

$$\frac{\mu_{\rm m_d}}{\mu_{\rm f}} = \mathcal{F}\left(\frac{\Phi}{\Phi_{\rm pack}}\right)\mathcal{K}\left(\mathcal{S}t_0\right) . \tag{3.2}$$

$\mathcal{F}$ is only a function of $\Phi/\Phi_{\rm pack}$, which tends towards unity as $\Phi/\Phi_{\rm pack}$ tends to zero, and towards infinity when $\Phi/\Phi_{\rm pack}$ tends to unity. $\mathcal{K}$ only depends on the Stokes number defined as $\mathcal{S}t_0 = \frac{(\rho_{\rm d}-\rho_{\rm f})(\rho_{\rm d}+\frac{1}{2}\rho_{\rm f})g d^3}{18\ \mu_{\rm f}^2}$, which is constant for a given fluid-particle system and characterizes the role played by the inertia of the dispersed particles through their

fluctuating motion. Fig. 3.2 shows that the experimental results obtained with the present suspensions collapse on the master curve proposed by Amin *et al.* (2021), which validates the relevance of the viscosity $\mu_{\mathrm{m_d}}$ determined from Eq. 3.1. However, $\mu_{\mathrm{m_d}}$ characterizes the viscous stresses at the scale of the dispersed beads. It is therefore questionable whether it is relevant to describe the macroscopic viscosity of the mixture when the suspension is subjected to a shear at a scale that is large compared to d Hinch (1977*b*). This question motivated us to study the fall of a large sphere of diameter $D \gg d$ through such fluidized suspensions.

3.2.2 Falling sphere experiments

The characteristics of the falling spheres are given in Table 3.2. They are made of glass and have a density close to that of the dispersed particles ($\pm 6\%$) and approximately 2.5 times that of the liquid. Their diameter ranges between 12.2 and 22.4 mm, corresponding to diameter ratios D/d from 36 to 140. The sphere falling experiments are conducted as follows. Since the suspension is opaque, we needed to find an alternative to optical methods. A thread of nylon with a diameter of 0.4 mm is attached to a support above the column, at one extremity, and glued to the sphere, at the other one. The thread length is adjusted so that the sphere can be suspended within the column without touching the bottom. A mark is made on the thread at a location that coincides with the top of the suspension while the sphere is hanging from the support. At the beginning of a test, the sphere is fully immersed in the suspension and positioned just below the top of the fluidized bed. Then, the sphere is released and falls through the suspension until the thread is taut. A high-speed Phantom VE-O 340L camera with a LED lighting is used to record the process at a rate of 1000 frames per second. The release of the sphere is visible on the movie and the end of the fall corresponds to the instant when the mark on the thread reaches the top of the bed. The uncertainties on the detection of the times of release and fall end are of ± 3 images. Depending on the system under consideration, the

fall time T lies between 500 and 1300 ms and is measured with an accuracy of ± 6 ms. The fall length L is known from the thread length and varies from 20 to 60 cm, depending on the suspension height.

Because the sphere velocity $V(t)$ takes a certain time to reach its terminal value V_t, the average velocity $\langle V \rangle = L/T$ is not equal to V_t. A better approximation of V_t is obtained by assuming that the sphere motion includes a stage of constant acceleration $\dot{V}_0$ followed by a stage of constant velocity $\tilde{V}_t$. Considering that the fall length is given by $L = \int_0^T V(t)dt$, one gets that $\tilde{V}_t$ is a solution of the following second-degree equation,

$$\tilde{V}_t^2 - \left(2T\dot{V}_0\right)\tilde{V}_t + \left(2L\dot{V}_0\right) = 0\,, \tag{3.3}$$

the initial acceleration being obtained from the balance between the inertial forces and the reduced weight acting on the sphere,

$$\dot{V}_0 = \frac{(\rho_\mathrm{d} - \rho_\mathrm{m})g}{\rho_\mathrm{d} + \frac{1}{2}\rho_\mathrm{m}}\,, \tag{3.4}$$

where $\frac{1}{2}\rho_\mathrm{m}$ accounts for the added mass. With this model, the terminal velocity is reached at time $t_\mathrm{t} = \tilde{V}_\mathrm{t}/\dot{V}_0$. Thus, $\tilde{V}_\mathrm{t}$ tends towards V_t when t_t/T becomes small, i.e. when the acceleration stage is short compared to the whole fall duration. We have determined $\langle V \rangle$, $\tilde{V}_\mathrm{t}$ and t_t/T for all the tests made. In the following, only the tests with $t_\mathrm{t}/T \leq 0.3$ have been retained. In this case, the difference between $\langle V \rangle$ and $\tilde{V}_t$ is less than 15% and we estimate that the discrepancy between $\tilde{V}_\mathrm{t}$ and V_t is less than 5%. All the subsequent analysis is thus done by using $\tilde{V}_\mathrm{t}$ as the terminal velocity of the spheres. Note that the experimental data have also been processed by considering a less demanding criterion $t_\mathrm{t}/T \leq 0.5$, which does not change the present conclusions and proves the robustness of the results regarding the determination of $\tilde{V}_\mathrm{t}$.

3.3 Experimental results

The terminal velocity U of the sphere relative to the fluid-particle mixture is obtained by adding the fluidization velocity U_f, so that $U = V_\mathrm{t} + U_\mathrm{f}$. Fig. 3.3 shows U as a function

Sphere properties	$S1$	$S2$	$S3$
Diameter D [mm]	12.2	15.7	22.4
Density ρ_d [kg m^{-3}]	2.64×10^3	2.60×10^3	2.50×10^3

Table 3.2

Physical properties of the falling spheres

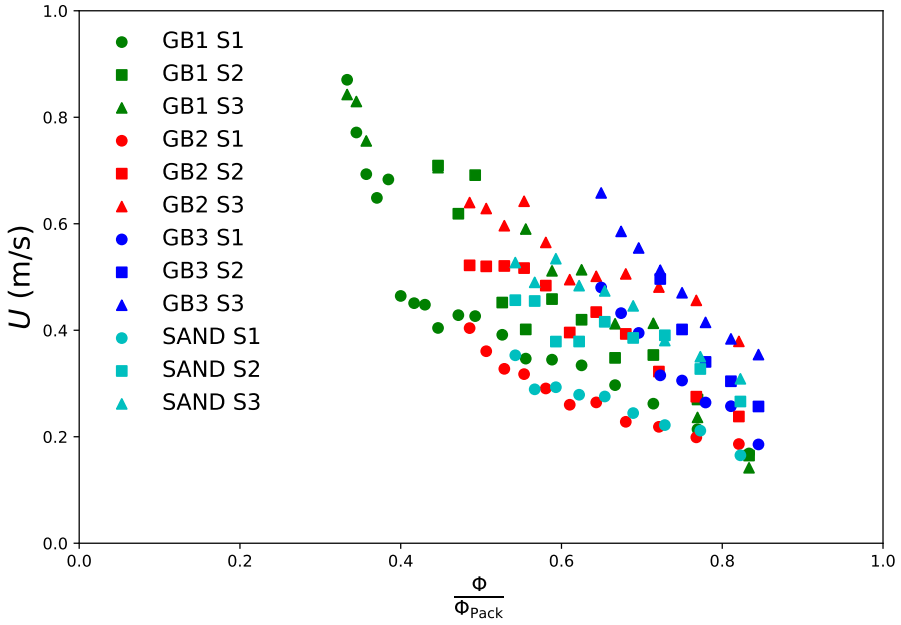

Figure 3.3

Relative sphere velocity versus particle concentration.

of Φ/Φ_{pack} for the three spheres and the four types of suspensions. The values of U ranges between 0.1 and 0.9 m/s and are much larger than the fluidization velocities, which remain less than 0.01 m/s. In any case, U is thus almost equal to V_{t}. It is a decreasing function of Φ/Φ_{pack}, since both the density and the effective viscosity of the suspension increase with the solid volume fraction. For a given type of bead, U is also observed to decrease with D. However, it is difficult to draw physical conclusions from these dimensional plots.

As shown by Hooshyar *et al.* (2013), an important dimensionless group is the other Stokes number defined by $St = \tau_d/\tau_D$, which compares the response time of the dispersed particles, $\tau_d = (\rho_{\text{d}} + \frac{1}{2}\rho_{\text{m}})d^2/18\mu$, to the time scale of the flow generated by the motion of the large body, $\tau_D = D/U$. For $St < 1$, the particles follow the stream lines of the suspending fluid, whereas, for $St > 1$, they may collide with the large body. In the present case, this Stokes number is much less than unity ($2 \times 10^{-3} < St < 9 \times 10^{-2}$), which makes it reasonable to assume that the suspension behaves globally as a homogeneous fluid. It is thus relevant to analyze the results in terms of the relationship between the drag coefficient and the Reynolds number of the falling sphere. If the drag coefficient is obtained directly from the balance between the drag force and the reduced weight of the sphere, $C_{\text{d}} = \frac{4}{3}\frac{(\rho_{\text{d}}-\rho_{\text{m}})gD}{\rho_{\text{m}}U^2}$, the Reynolds number requires the knowledge of the effective viscosity of the suspension. Let us consider the viscosity $\mu_{\text{m}_{\text{d}}}$ defined by Eq. 3.1 and introduce $Re_{\text{m}} = \frac{\rho_{\text{m}}UD}{\mu_{\text{m}_{\text{d}}}}$. Fig. 3.4 shows log-log plots of the experimental values of C_{d} versus Re_{m}, for all investigated cases. For any given pair of sphere and suspension, the values of C_{d} collapse on a $Re_{\text{m}}{}^{-1}$ straight line. On these plots, the Reynolds number has been divided by a constant k, which has been adjusted to make the data of the various systems to coincide with the drag Stokes law, $C_{\text{d}} = 24/Re$. The values of k varies from one system to another, but remain constant for a given system, which means that they are independent of Re_{m}. In Fig. 3.5, k is plotted against D/d and turns out to be a linear function of the sphere-to-bead diameter ratio : $k = \alpha D/d$, with $\alpha \approx 0.58$. Therefore, the experimental

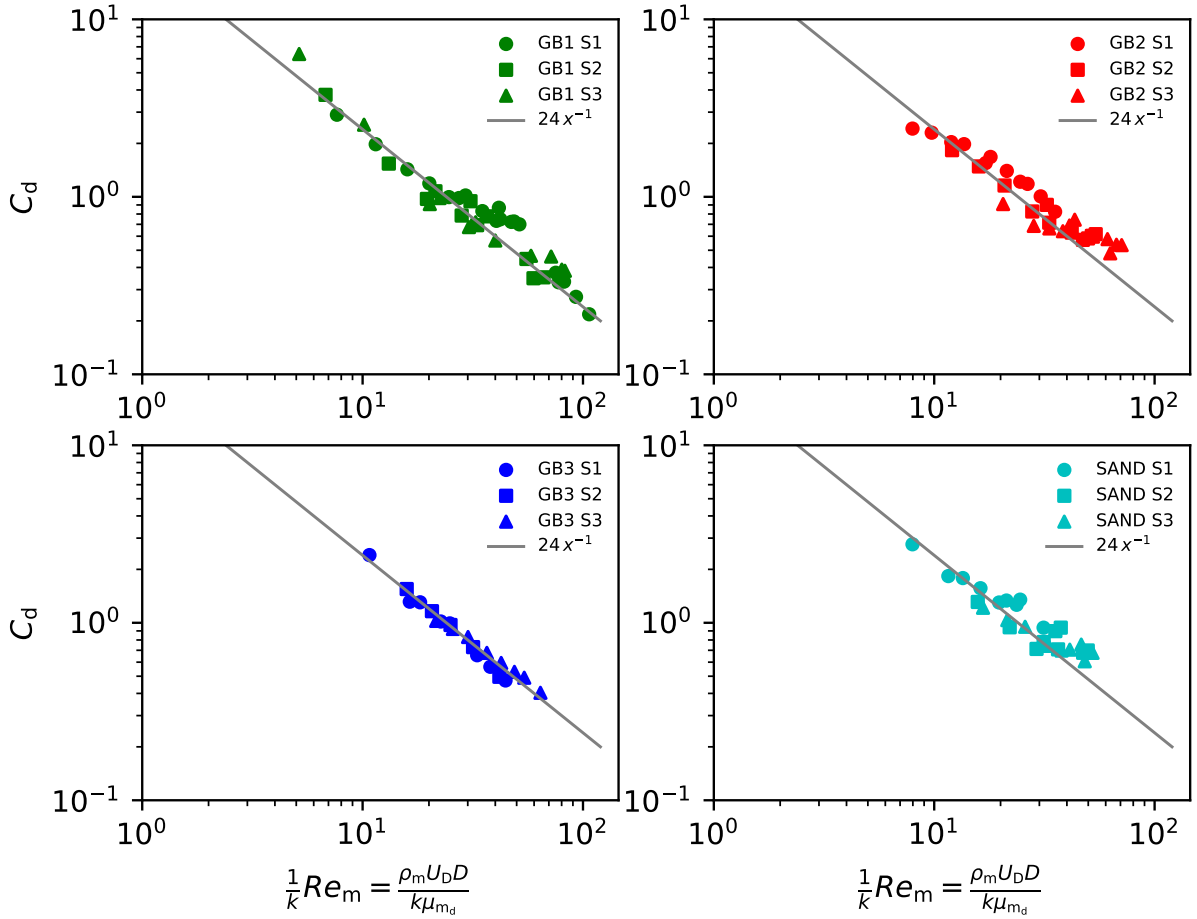

Figure 3.4

Drag coefficient of the sphere versus the Reynolds number (values of k in Fig 3.5).

results lead to the following quite unexpected expression of the drag coefficient,

$$C_{\mathrm{d}} = 24\,\frac{\mu_{\mathrm{m_d}}}{\rho_m U D}\,\alpha\frac{D}{d} = 24\alpha\,\frac{\mu_{\mathrm{m_d}}}{\rho_m U d}\,, \tag{3.5}$$

which is independent of the size D of the falling sphere and proportional to $\mu_{\mathrm{m_d}}$.

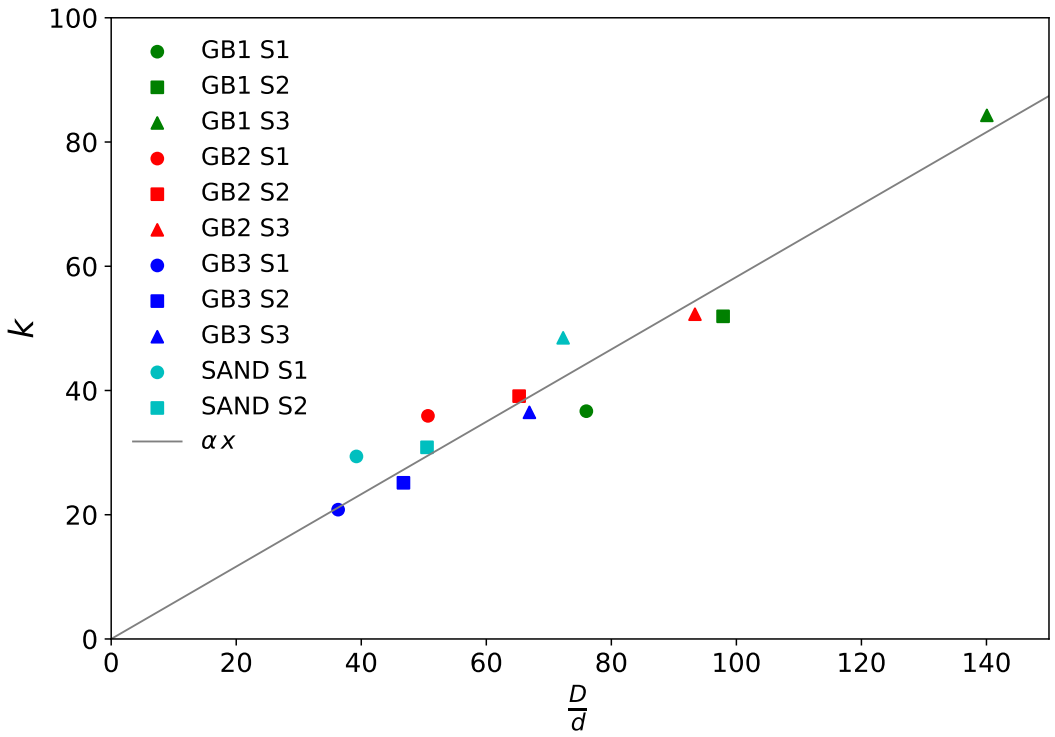

Figure 3.5

Coefficient k against $\frac{D}{d}$.

3.4 Discussion

3.4.1 Interpretation based on a large-scale effective rheology

Since Eq. 3.5 gather all the experimental results, it seems natural to use it to determine the effective viscosity μ_{m} of the suspension. Eq. 3.5 is similar to the Stokes' drag,

$$F_{\mathrm{D_{St}}} = (\pi D^2)\,\mu_{\mathrm{m}}\frac{3U}{D}\,, \tag{3.6}$$

if one sets

$$\mu_{\mathrm{m}} = \alpha\mu_{\mathrm{m_d}}\frac{D}{d}\,. \tag{3.7}$$

Since $\mu_{\mathrm{m_d}}$ represents the effective viscosity at the scale d of the beads, one would expect the effective viscosity at a much larger scale D to be different. However, it should converge towards a constant value when D/d becomes large. This is inconsistent with Eq. 3.7 that predicts that μ_{m} still increases linearly with D/d for values of D/d larger than 100. The other interpretation, which states that μ_{m} actually varies with D because it would depend on the shear rate $\dot{\gamma} \propto U/D$, is also inconsistent because it leads to contradictory behaviors according to that $\dot{\gamma}$ varies by changing either U or D. Indeed, taking U constant, decreasing D leads to an increase of $\dot{\gamma}$ and a decrease of μ_{m}, which corresponds to a strain-softening behavior. Otherwise, taking D constant, increasing U leads to an increase of $\dot{\gamma}$ while μ_{m} remains constant, which corresponds to a Newtonian behavior. Moreover, the sphere Reynolds number based on μ_{m} is too large ($5 < UD/k\mu_{\mathrm{m}} < 100$, see Fig. 3.4) for the Stokes' drag law to be valid. Therefore, the effective viscosity of the suspension cannot be determined from Eq. 3.7.

3.4.2 Interpretation based on the wall boundary condition

As noted by Ovarlez *et al.* (2006), determining the effective viscosity of a suspension from the measurement of the force exerted on a wall requires the homogeneity of the suspension near the wall. However, this condition is never rigorously fulfilled at the scale

of the dispersed particles. Since a particle cannot approach a wall at a distance that is closer than its radius, the volume fraction of the dispersed phase tends to zero at a wall Lubchenko *et al.* (2018); du Cluzeau *et al.* (2019). In addition, the interactions between a wall and the dispersed particles differ from the interactions between a wall and the suspending fluid. A fluid adheres to a wall because of molecular interactions such as van der Waals forces, whereas dispersed particles can move relatively to a wall. Considering the blood flow for example, the red blood cells may experience a wall slip velocity of 40% of the maximum flow velocity Roman *et al.* (2012). In the framework of two-fluid approaches, this can be modeled by increasing the viscosity of the plasma near the wall in order to account for the additional dissipation induced by the slip motion of the cells Sharan & Popel (2001). However, it is not relevant to model the whole mixture as a homogeneous fluid satisfying a non-slip condition at a wall.

Since a rheological approach is inappropriate for the present results, we must consider an alternative interpretation. The drag force F_D is the integral of the wall shear stress τ_p on the sphere surface. In the case of a homogeneous fluid of viscosity μ_m with negligible inertia, the shear stress is constant along the sphere wall Batchelor (1967), $\tau_p = \mu_\mathrm{m}\frac{3U}{D}$, which leads to the Stokes' drag given by Eq. 3.6. In contrast, the present experiments lead to

$$F_\mathrm{D} = (\pi D^2)\,\mu_{\mathrm{m_d}}\frac{3\alpha U}{d}\,, \tag{3.8}$$

where the average wall shear stress, $\tau_p = \mu_{\mathrm{m_d}}\frac{3\alpha U}{d}$, is the product of the effective viscosity at the scale of the particles, $\mu_{\mathrm{m_d}}$, and the wall shear rate, $\dot{\gamma} = \frac{3\alpha U}{d} \approx 0.9\frac{U}{d/2}$. This corresponds to the shear experienced by a fluid between a wall and a particle located at a distance $d/2$ from it and moving at a speed U relative to it. Since $\dot{\gamma}$ is independent of D, the wall friction is not related to the structure of the flow away from the wall, and thus to the rheology of the mixture at the scale of the sphere.

3.5 Conclusion

For dispersed two-phase flows in general, this result highlights that rheological characterizations, which rely on the measurement of the effort that a suspension exerts on a wall, should not assume a non-slip velocity at wall, but consider instead an imposed shear rate. Apart from the blood circulation, a few other studies have reported evidences of such a wall slip. A foam in a pipe was shown to behave as a rigid body slipping on a lubricated layer at the wall and the authors concluded that "the flow of such foams is not controlled by foam rheology" Briceño & Joseph (2003). The flow of a concentrated gas-solid suspension released after a dam break was also observed to flow as an inviscid fluid that slips on the wall Girolami & Risso (2020). Regarding an imposed wall shear rate, it is worth mentioning an investigation of the flow of a homogeneous oil-in-water droplet emulsion in a pipe Abbas *et al.* (2017). While the effective viscosity of the emulsion μ_{m} was found to vary over the pipe cross-section and to depend on the bulk velocity U, the viscosity at the wall $\mu_{\mathrm{m_w}}$ was observed to be independent of U and the pressure drop along the pipe to be proportional to $\mu_{\mathrm{m_w}}U$. This surprising outcome is fully compatible with the present result, $\tau_p = \mu_{\mathrm{m_d}}\frac{3\alpha U}{d}$, where $\mu_{\mathrm{m_d}}$ is independent of U and implies a pressure drop that is proportional to $\mu_{\mathrm{m_d}}U$, whatever is the nature of the flow or the mixture rheology away from the wall.

To conclude, the drag force on a large sphere falling in a fluidized suspension of small particles (Eq. 3.8) is the product of the sphere area πD^2, the viscosity μ_{m_d} determined from the fluidization velocity of the dispersed particles (Eq. 3.1), and the ratio U/d of the sphere velocity and the particle diameter. From a general perspective, this suggests that the friction exerted by a suspension on a wall is driven by a mechanism involving the dissipation associated with the slip velocity of the particles relatively to the wall.

Bibliographie

Abbas, M., Climent, E., Simonin, O. & Maxey, M. R. 2006 Dynamics of bidisperse suspensions under Stokes flows : Linear shear flow and sedimentation. *Physics Of Fluids* **18** (12), 121504.

Abbas, M., Pouplin, A., Masbernat, O., Liné, A. & Décarre, S. 2017 Pipe flow of a dense emulsion : Homogeneous shear-thinning or shear-induced migration ? *AIChE J.* **63** (11), 5182–5195.

Abrahamsen, A. R. & Geldart, D. 1980 Behaviour of gas-fluidized beds of fine powders part I. Homogeneous expansion. *Powder Technology* **26** (1), 35–46.

Alméras, E., Masbernat, O., Risso, F. & Fox, R. O. 2019 Fluctuations in inertial dense homogeneous suspensions. *Physical Review Fluids* **4** (10), 102301.

Amin, A., Girolami, L. & Risso, F. 2021 On the fluidization/sedimentation velocity of a homogeneous suspension in a low-inertia fluid. *Powder Tech.* **391**, 1–10.

Bargieł, M. & Tory, E. M. 2013 Extension of the Richardson–Zaki equation to suspensions of multisized irregular particles. *International Journal of Mineral Processing* **120**, 22–25.

Batchelor, G. K. 1967 *An introduction to fluid dynamics*. Cambridge University Press.

Briceño, M. & Joseph, D. 2003 Self-lubricated transport of aqueous foams in horizontal conduits. *Int. J. Multiphase Flow* **29** (12), 1817–1831.

Chen, J. L. P. & Keairns, D. L. 1975 Particle segregation in a fluidized bed. *The Canadian Journal of Chemical Engineering* **53** (4), 395–402.

Clift, R., Grace, J. & Weber, M. 1978 *Bubble, Drops and Particles*. Academic Press.

du Cluzeau, A., Bois, G. & Toutant, A. 2019 Analysis and modelling of Reynolds stresses in turbulent bubbly up-flows from direct numerical simulations. *J. Fluid Mech.* **866**, 132–168.

Einstein, A. 1906 Eine neue bestimmung der moleküldimensionen. *Ann. Phys.* **19**, 289–306.

Einstein, A. 1911 Berichtigung zu meiner arbeit : Eine neue bestimmung der moleküldimensionen. *Ann. Phys.* **34**, 591–592.

Ergun, S. 1952 Fluid flow through packed colmuns. *Chemical Engineering Progress* **48** (2), 89–94.

Funamizu, N. & Takakuwa, T. 1995 An improved Richardson-Zaki formula for computing mixed layer composition in binary solid-liquid fluidized beds. *Chemical Engineering Science* **50** (19), 3025–3032.

Girolami, L. 2008 Dynamique et sédimentation des écoulements pyroclastiques reproduits en laboratoire. PhD thesis, Université de Clermont II.

Girolami, L., Druitt, T. H. & Roche, O. 2015 Towards a quantitative understanding of pyroclastic flows : Effects of expansion on the dynamics of laboratory fluidized granular flows. *Journal of Volcanology and Geothermal Research* (296), 31–39.

Girolami, L. & Risso, F. 2019 Sedimentation of gas-fluidized particles with random shape and size. *Physical Review Fluids* **4** (7), 074301.

Girolami, L. & Risso, F. 2020 Physical modeling of the dam-break flow of sedimenting suspensions. *Physical Review Fluids* **5** (8), 084306.

Guazzelli, É. & Pouliquen, O. 2018*a* Rheology of dense granular suspensions. *Journal of Fluid Mechanics* **852**, 35–73.

Guazzelli, E. & Pouliquen, O. 2018*b* Rheology of dense granular suspensions. *J. Fluid Mech.* **852**, 35–73.

Hinch, E. J. 1977*a* An averaged-equation approach to particle interactions in a fluid suspension. *Journal of Fluid Mechanics* **83** (4), 695–720.

Hinch, E. J. 1977*b* An averaged-equation approach to particle interactions in a fluid suspension. *J. Fluid Mech.* **83** (4), 695–720, publisher : Cambridge Univ Press.

Hooshyar, N., van Ommen, J. R., Hamersma, P. J., Sundaresan, S. & Mudde, R. F. 2013 Dynamics of Single Rising Bubbles in Neutrally Buoyant Liquid-Solid Suspensions. *Phys. Rev. Lett.* **110** (24), 244501.

Koo, S. 2008 Sedimentation velocity of bidisperse suspensions. *Journal of Industrial and Engineering Chemistry* **14** (5), 679–686.

Kramer, O. J. I., de Moel, P. J., Baars, E. T., van Vugt, W. H., Padding, J. T. & van der Hoek, J. P. 2019 Improvement of the Richardson-Zaki liquid-solid fluidisation model on the basis of hydraulics. *Powder Technology* **343**, 465–478.

Krieger, I. M. & Dougherty, T. J. 1959 A mechanism for non-Newtonian flow in suspensions of rigid spheres. *Transactions of the Society of Rheology* **3** (1), 137–152.

Lettieri, P., Newton, D. & Yates, J. G. 2002 Homogeneous bed expansion of FCC catalysts, influence of temperature on the parameters of the Richardson–Zaki equation. *Powder Technology* **123** (2-3), 221–231.

Lubchenko, N., Magolan, B., Sugrue, R. & Baglietto, E. 2018 A more fundamental wall lubrication force from turbulent dispersion regularization for multiphase CFD applications. *Int. J. Multiphase Flow* **98**, 36–44.

Nguyen, N.-Q. & Ladd, A. J. C. 2005 Sedimentation of hard-sphere suspensions at low Reynolds number. *Journal of Fluid Mechanics* **525**, 73–104.

Ovarlez, G., Bertrand, F. & Rodts, S. 2006 Local determination of the constitutive law of a dense suspension of noncolloidal particles through magnetic resonance imaging. *J. Rheol.* **50** (3), 259–292.

Popel, A. S. & Johnson, P. C. 2005 Microcirculation and hemology. *Annu. Rev. Fluid Mech.* **37** (1), 43–69.

Richardson, J. F. & D, W. N. Z. P. 1954 Sedimentation and fluidisation : Part I. *Trans. Inst. Chem. Eng.* **32**, S82–S100.

Richardson, J. F. & Zaki, W. N. 1954 The sedimentation of a suspension of uniform spheres under conditions of viscous flow. *Chemical Engineering Science* **3** (2), 65–73.

Roman, S., Lorthois, S., Duru, P. & Risso, F. 2012 Velocimetry of red blood cells in microvessels by the dual-slit method : Effect of velocity gradients. *Microvasc. Res.* **84** (3), 249–261.

Sharan, M. & Popel, A. S. 2001 A two-phase model for flow of blood in narrow tubes with increased effective viscosity near the wall. *Biorheology* **38**, 415–428.

Valverde, J. M. & Castellanos, A. 2008 A modified Richardson–Zaki equation for fluidization of Geldart B magnetic particles. *Powder Technology* **181** (3), 347–350.

Chapitre 4

Transport and deposition of non-colloidal suspension-flows

Abstract

We carried out novel experiments of the dam-break flow of particulate suspensions made with glass beads and water at different concentrations ($0.70 < \phi_s/\phi_{pack} < 1$). When released, the mixture travels down the flume by defluidizing progressively until motion ceases. The flow front exposes three phases of transport : (1) a brief phase of gravitational acceleration associated with the mixture collapse ; (2) a dominant constant-velocity phase associated with the formation of a basal deposit and a thin upper layer of water ; (3) a brief stopping phase. The decrease of the initial values of ϕ_s/ϕ_{pack} acts in promoting the flow mobility, increasing the runout distance and time, and forming thinner and more elongated deposits. The mean flow velocity as well as the frontal velocity both increase with decreasing values of ϕ_s/ϕ_{pack}. This increase of mobility may be related to the delay of particles sedimentation during the flow and the decrease of the deposit aggradation rate with decreasing values of ϕ_s/ϕ_{pack}. In the proximal areas, the aggradation velocity decreases with time and with decreasing values of ϕ_s/ϕ_{pack}. In distal areas, the aggradation

velocity is approximately constant with time and almost independent of the initial mixture concentration. Velocity profiles, measured in the flows at different times and locations, reveal the presence of a thin basal sheared layer overlaid by a thick and rapid weakly sheared suspension in the absence of sedimentation. Otherwise, when the sedimentation is initiated, the velocity profile becomes almost independent of the time, with a basal deposit overlaid by a moderately sheared suspension. Deposit shapes allow us to distinguish two different flow regimes : (1) a regime dominated by gravity, with a flow mobility limited by a rapid sedimentation that leads to a triangular deposit shape, characteristics of the highly concentrated mixtures ($\phi_s/\phi_{pack} \geq 0.85$) ; (2) a regime dominated by the hindered settling processes, with a mobility promoted by a slow sedimentation, that leads to a trapezoidal deposit shape, characteristics of the weakly concentrated mixtures ($\phi_s/\phi_{pack} \leq 0.85$). Such moving experiments may be modeled, to a first approximation, as static, slightly horizontally sheared sedimenting suspensions.

4.1 Introduction

The sediments transfer in settled rivers can be dramatically promoted by the occurrence of extreme events (i.e. flash floods, dam failures and breaks) through the formation of hazardous debris flows, non colloidal or colloidal mudflows, as well as hyperpycnal currents. Beyond the major morphological repercussions observed at the vicinity of the watersheds heads (i.e. overflows, braided-meandering), the passage of the flood wave can cause the intense erosion of the river banks and bottom that may lead to the formation of sediment-laden flows (Figure 4.1) whose dynamics mainly depends on the particles concentration within the mixture. Classical numerical simulations, that involve purely hydrodynamic equations, commonly used to predict the proximal behavior of the dam-break wave, become no longer suitable for the description of such catastrophic events [Fraccarollo & Capart, 2002] that have recently affected the Roya and Vésubie valleys as well as the Angel Bay of Nice after the passage of the Alex storm (October 2^{nd}, 2020).

Even though the slow evolution of a river bed has been extensively explored since the last decades [Charru et al., 2004, 2006; Fourrière, 2009; Lajeunesse et al., 2010; Devauchelle et al., 2010], the problem of rapid morphological changes (Figure 4.1) remains much less advanced [Foda et al., 1997; Capart & Young, 2002; Fraccarollo & Capart, 2002; Zech et al., 2010]. One of the main explanations lies on the complex interactions between the granular bed and the wave dynamics over different space- and timescales. A famous example of dam failure occurred in 1996 at the Lake Ha! Ha! (Quebec, Canada, Figure 4.1) [Brooks & Lawrence, 1999]. Beyond the significant near-field effects, the flood wave caused a severe erosion which damaged the downstream valley by widening the river course by up to 700 % (Figure 4.1). Afterwards, Fraccarollo & Capart (2002) as well as Zech et al. (2010) developed idealized dam-break experiments and modeling to predict the wave dynamics (i.e. height, arrival time) and get insights into the risk assessment and alert organization in upland valleys in case of similar situations.

Figure 4.1

(a) Correlation between the volume of sediments mobilized and that of the water released during past episodes of dam or dyke failures [Capart, 2000]. (b) Resulting widening of the river bed during the dam-failure of lake Ha! Ha! [Brooks & Lawrence, 1999]. (c) Evidences of bottom erosion after the passage of a highly concentrated flow down to the Ha! Ha! Bay [Brooks, 2003].

Since the two last decades, the physical description of these flows has become a major issue for the prediction of both the wave arrival time and speed as well as the surface

affected by the deposits, which may depend on the mixture dynamics and rheology. This step requires therefore the determination of relevant scaling laws that can be achieved only through the realization of laboratory experiments, performed in a well-controled geometry, such as a rectangular dam-break flume which reasonably enables to both generate a dense, homogeneous suspension in a locked reservoir as well as a gravitational sedimenting current that travel down a flume. To date, many scientific efforts have been devoted to the description of the dam-break flow of pure fluids, dry granular materials, or gas-fluidized mixtures principally [Rottman & Simpson, 1983 ; Simpson, 1997 ; Eames & Gilbertson, 2000 ; Fraccarollo & Capart, 2002 ; Hogg & Pritchard, 2004 ; Roche et al., 2004 ; Lajeunesse et al., 2005 ; Hogg, 2006 ; Cantero et al., 2007 ; Girolami et al., 2008 ; 2015 ; Zech et al. 2010 ; Shimizu et al., 2017 ; 2019] as well as to the collapse of loose or compacted immersed granular materials, or gas-fluidized suspensions into a flume filled with water [Courrech du Pont et al., 2003 ; Chauchat, 2007 ; Pailha, 2008 ; Rondon et al., 2011 ; Bougouin, 2017 ; Bougouin et al., 2019 ; Robbe-Saule et al., 2021]. These works have highlighted the role of both the solid volume fraction and the initial column geometry on the flow dynamics. However, to date no laboratory experiments, involving homogeneous liquid-solid suspensions explored in a wide range of solid volume fractions, have been proposed to properly describe the sedimentation behavior that control the dynamics of such flows during their final course. Amin et al. (2021) recently highlighted that the sedimentation velocity U_{sed} of such static suspensions solely depends on the solid volume fraction ϕ_s normalized by its value at packing ϕ_{pack}, a parameter that appears sufficient to encapsulate all the specificities of the considered material, as well as on the particle inertia through the Stokes number St. They have so identified the relevant scaling for U_{sed} in static suspensions but need henceforth to describe the flowing situation. Once released down the flume, gas-solid suspensions collapse from a height h_0 to form a quasi-inviscid current whose flow front travels at a quasi-constant speed $U_{\mathcal{F}}$ that scales with the gravitational velocity $\sqrt{gh_0}$ [Roche et al., 2004 ; Girolami et al., 2008]. However, the correlation between the sedimentation processes, closely related to the mixture rheology, and the

gravitational flow have been recently revisited by Girolami & Risso (2020) in the aim of properly describing such complex phenomena in which two distinct processes are expected to behave independently, thus requiring two separate descriptions : (1) a vertical Stokes flow, governed by particles sedimentation ; (2) a slightly dissipative potential dam-break flow, characterized by a high Reynolds number $\mathcal{R}e = \mathcal{O}(10^4)$ and governed by the sedimentation processes. The present study aims at first presenting novel experiments of the dam-break flows of liquid-solid suspensions, whilst providing a qualitative description of the flow and deposition that may possibly help for the description of hyperpycnal currents and lahars inferred, until now, only from field observations and measurements [Mulder et al., 1997 ; Lavigne & Thouret, 2000 ; Vallance & Iverson, 2015 ; Thouret et al ;, 2020].

4.2 Experimental methods

4.2.1 The dam-break flume

The experiments were carried out in a linear lock-exchange flume endowed with a 20-cm-long, 30-cm-wide, and 70-cm-high rectangular reservoir in which the material was fluidized and expanded before being released down a 3-m-long and 30-cm-high horizontal channel. For this study, the reservoir was separated into two compartments, each of 10 *cm*-long, in order to allow the use of a spillway, located at 27 *cm* above the filter cloth that delimits the porous medium, to ensure the instantaneous expel of water from the suspension surface and generate a free-surface homogeneous suspension. During the preparation of experiments, the particles were first poured into the reservoir, then fluidized and progressively defluidized in order to flatten the bed surface and being able to correctly measure the solid volume fraction at packing which also requires the measurement of the bed mass and particles density. Once characterized, the bed is thus fluidized and expanded at a given rate. Varying the initial expansion rate of the mixture, from one experiment to another, amounts to vary the ratio ϕ_s/ϕ_{pack}. The incoming fluid rate is measured in

aid of a magnetic flowmeter with an accuracy of 0.01 $L.min^{-1}$, whilst its temperature is measured at the beginning and the end of each experiment in order to properly determine the fluid viscosity. Once the mixture is homogeneously fluidized and uniformly expanded, the sliding gate is opened thanks to a hydraulic cylinder, which ensures a constant and sufficient aperture velocity that does not disturb the column release, and simultaneously to the stop of fluidization. The mixture is thus released down the impermeable flume, in the manner of a dam break. This forms a fast-moving, but short-lived, slightly sheared free-surface flow that defluidizes progressively until motion ceases (Figure 5.2a). At the end of experiment, the deposit morphology is measured every 5 cm from the lock gate. As the flow are reproducible, the experiment was first recorded with a semi-fast camera in order to get a global view of the flow of around 3-m-wide ; then repeated, using a high-speed video camera, to get a series of viewing windows of 50-cm-wide in order to study the internal flow structures and dynamics in more details, such as the velocity fields and profiles, as well as the aggradation velocities of the basal deposits formed during propagation.

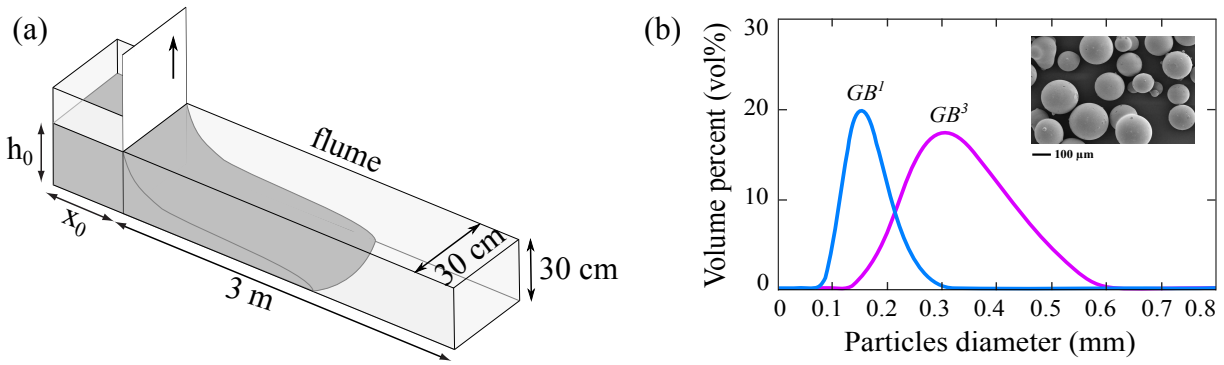

Figure 4.2

(a) Illustration of the free-surface flows reproduced in this configuration. (b) Grain-size distribution of the glass-beads used in these experiments.

4.2.2 The synthetical materials

In these experiments, two different types of glass beads were used, those termed GB^1 and GB^3 in the previous studies (Table 4.1). As exposed in Figure 5.2b, the materials

have a quasi-spherical shape. With the aim of ensuring the formation of homogenous suspensions associated with a uniform expansion, the two materials were sieved in order to reduce their granulometric distribution and prevent the development of segregation. A first sieving was performed to discard the dusts, whilst a second one allows to discard the particle clusters, In this way, no size-segregation was develop in experiments. Once sieved, a representative sample of the material batch used in experiments was obtained in aid of a splitter. Ten samples of dried materials were then analyzed with a laser granulometer and allowed us to obtain the grain size distribution (Figure 5.2b) as well as the particle equivalent diameter for each material, as reported in Table 4.1. As the height of the spillway was fixed and located at $27cm$ from the base, the mixture expansion height was fixed and maintained constant from one experiment to another ($h_0 = 27cm$), while the particles height h_p was chosen inferior to h_0 and decreased with increasing expansions (Table 4.1).

$Materials$	d_{50} (μm)	ρ $(kg.m^{-3})$	ϕ_{pack}	h_p (cm)	h_0 (cm)	ϕ_s/ϕ_{pack}
GB^1	163	2496	0.60	$24-27$	27	$0.85-1$
GB^3	337	2496	0.58	$19-27$	27	$0.70-1$

Table 4.1

Mean features of the materials used in the dam-break flow experiments.

As the idealized materials expose the same sedimentation behavior than the natural ones, the results obtained here may be extrapolated to other natural non-colloidal materials. In order to ensure a satisfying contrast in the viewing windows made with the high-speed camera, around 20% of glass beads used were tinted with a permanent black paint and used as passive tracers.

4.2.3 The reproducibility of experiments

To ensure the realization of viewing windows for the study of sedimentation processes without disturbing the recording of the global flow, from which the frontal position of the flow is measured, the experiments were carefully repeated 5 times taking similar initial conditions. The repetition of the experiments allowed us to determine the error bars for each measurement presented in the global description, such as the runout length and time, the mean velocity, as well as the deposit morphology. Figure 5.3 exposes the mean deposit morphology obtained from 8 experiments, thus including the error bar deduced from the results. From one experiment to another, we have considered that the reproducibility of the experiments was reliable enough to ensure a measurement of quality associated with a satisfying measurement uncertainty.

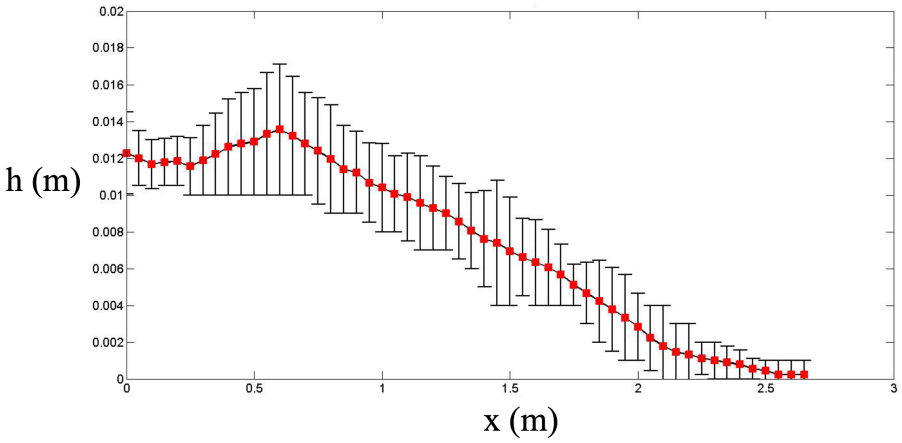

Figure 4.3

Illustration of the mean deposit morphology obtained from 5 repeated experiments, thus including the error bar. This example corresponds to the deposits of GB^3 when $\phi_s/\phi_{pack} = 0.775$.

4.3 The general flow behavior

When released, the homogeneous suspension of glass beads flows down the flume at speeds of up to 2 m.s^{-1} and defluidizes progressively until motion ceases (Figure 5.4a). During travel, the suspension initially homogeneous develops internal flow structures that allow us to distinguish three vertical layers (Figure 5.4b) : (1) a basal deposit that aggrades progressively during the flow, (2) a flowing suspension that thins progressively by expelling water upwards and particles downwards, and (3) an upper water layer formed progressively during the flow from the mixture sedimentation, as observed during the purely vertical collapse-tests performed in the reservoir. During propagation, the sedimentation takes place progressively, as well as the expel of water, while the motion ceases first at the front, then at the rear.

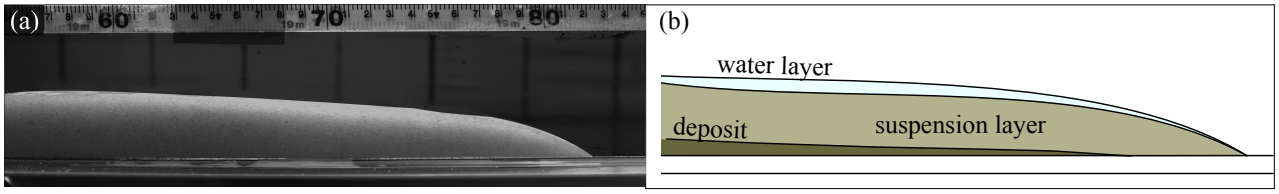

Figure 4.4

(a) Picture of a free-surface flow made with glass beads and water. (b) Illustration of the internal flow structures developed during propagation.

As commonly observed in classical dam-break flows, the propagation of the flow front takes place in three phases : (1) a brief initial acceleration phase that lasts around $0.25s$; (2) a dominant constant-velocity phase that lasts around $0.5 - 1s$; and (3) a short stopping phase that lasts around $0.2 - 0.3s$ (Figure 5.5). While the duration of the initial gravitational collapse is approximately similar from one experiment to another and independent of the initial mixture concentration ϕ_s/ϕ_{pack}, the duration of the phases 2 and 3 increases with decreasing values of ϕ_s/ϕ_{pack}. Note that the sedimentation processes are not initiated immediately after the passage of the flow front at a given position, but

after a time delay probably longer than the duration of the phase 1, and that may be increased with increasing mixture concentration ϕ_s/ϕ_{pack}.

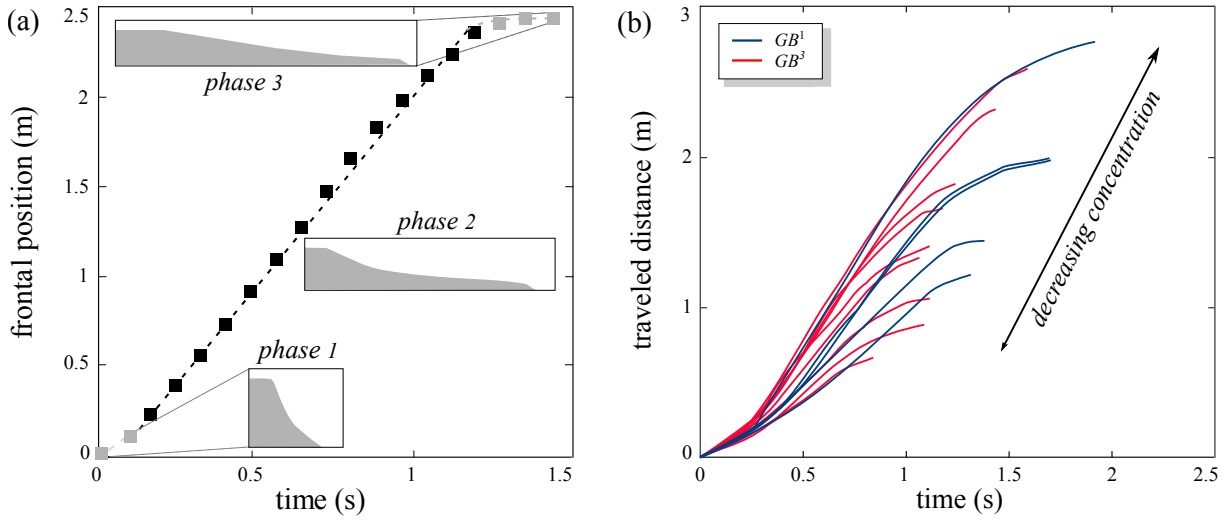

Figure 4.5

Position of the flow front with time. (a) Illustration of the three-phases of transport observed in classical dam-break flows. (b) Distance traveled by the flow front with time for all experiments involving GB^1 and GB^3.

As commonly observed in similar experiments performed with particles and gas [Girolami, 2008], the mobility of such flows increases with decreasing mixture concentration, characterized by the ratio ϕ_s/ϕ_{pack}. The final distance L traveled by the flows as well as the flow duration T both increase, almost linearly, with ϕ_s/ϕ_{pack} (Figure 4.6), pointing a simple and systematic behavior that solely depends on the intrinsic properties of the mixture, through ϕ_s/ϕ_{pack}, that controls the sedimentation processes. For each material, the final length reached by the flow front approaches $L \simeq 3m$, in around $T \simeq 2s$, for the lowest initial values of ϕ_s/ϕ_{pack}, while L decreases to $1m$ in around $1.1s$ at higher initial values of ϕ_s/ϕ_{pack}.

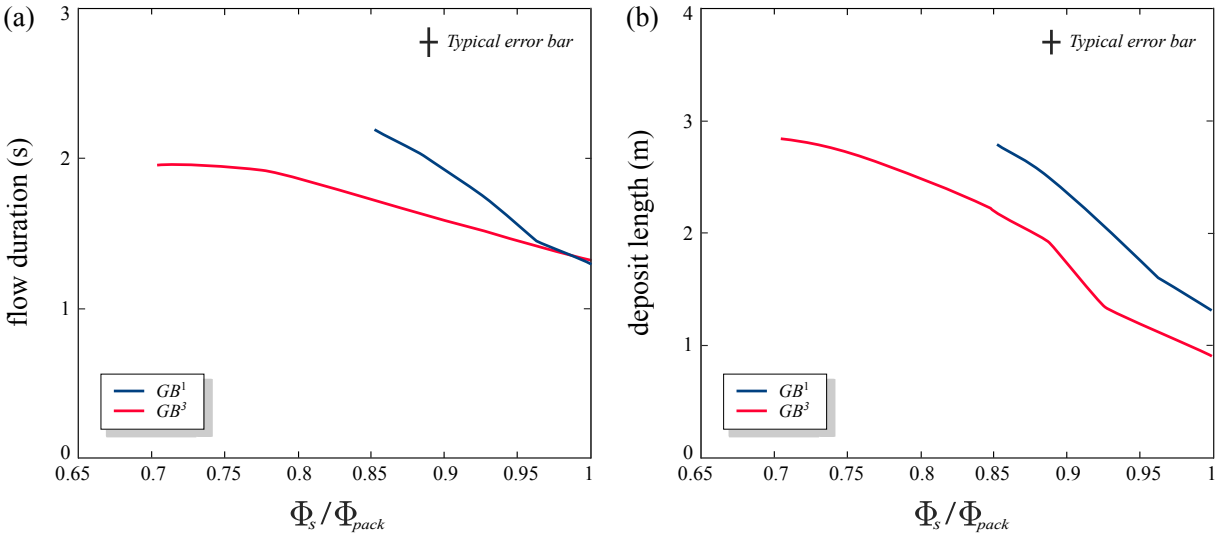

Figure 4.6

(a) Flow duration and (b) runout distance presented as a function of the initial mixture concentration ϕ_s/ϕ_{pack} for all experiments made with GB^1 and GB^3.

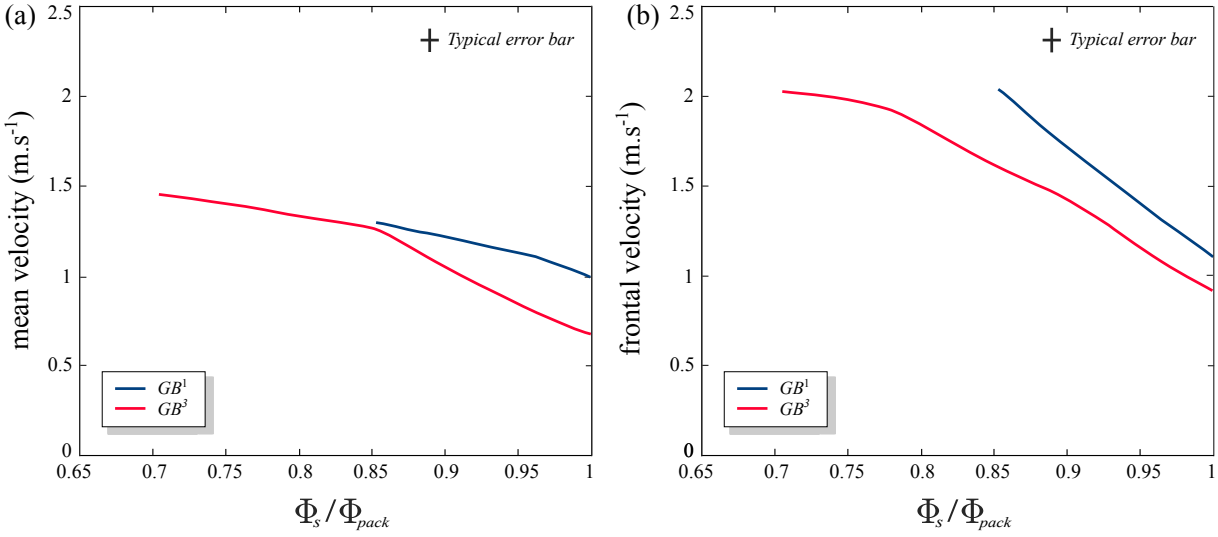

Figure 4.7

(a) Mean velocity and (b) frontal velocity presented as a function of the initial mixture concentration ϕ_s/ϕ_{pack} for all experiments made with GB^1 and GB^3. The frontal velocity corresponds to the phase-2 velocity.

The mean flow velocity U, determined as the ratio between L and T, $U = L/T$, as well as the frontal velocity, determined from the approximately constant-velocity phase of transport, both increase with decreasing values of ϕ_s/ϕ_{pack}. For each material, the frontal velocity is around $1m.s^{-1}$ when $\phi_s/\phi_{pack} = 1$, while reaching around $2m.s^{-1}$ for the lowest values of ϕ_s/ϕ_{pack} (Figure 4.7).

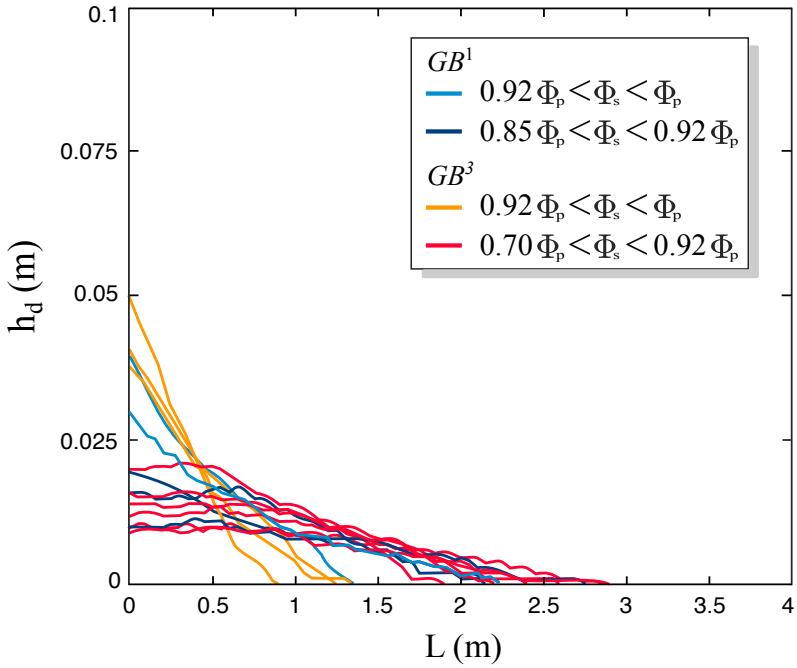

Figure 4.8

Morphology of the deposits let by each flow performed with GB^1 and GB^3.

At the end of each experiment, the deposit let by the flow is not totally defluidized since the bed is made with particles and a little quantity of water. The shape of the deposits depends on the initial conditions. When $\phi_s/\phi_{pack} \geq 0.85$, the deposits have a triangular shape (as represented in light blue and orange in Figure 5.7 for GB^1 and GB^3 respectively), which suggests that the flows are dominated by the gravitational collapse. When $\phi_s/\phi_{pack} \leq 0.85$, the deposits have a trapezoidal shape (as represented in dark blue and red in Figure 5.7 for GB^1 and GB^3 respectively), which suggests that the mobility is enhanced by the reduction of friction such as the flows are thus dominated by the hindered

settling processes. In any cases, the deposits are elongated with thicknesses less than $5cm$ for lengths of few meters (from $1.5m$ to $3m$ from the lock gate ; Figure 5.7).

4.4 The internal flow structures

In order to explore the flow dynamics, the velocity fields were first calculated within the viewing windows, which require four different steps reminded here :

1. **a geometric mask :** a rectangular area, focused on the passage of the flow, was delimited to discard us from the background in the calculations. This mask helps to reduce the computation time.
2. **a time filter :** a time filter was then applied to the studied area in order to remove some static points or objects which affect the measurement. This filter aims at vanishing the noise associated with the presence of these objects.
3. **the PIV processes :** the calculation of the velocity fields was done by dividing the studied area into a square mesh of 96 pixels, and then into a circular mesh of 32 pixels. This repetition aims at reducing the noise and the measurement error.
4. **the post processing step :** the post-processing step aims at correlating some unconsistent vectors with those located around them.

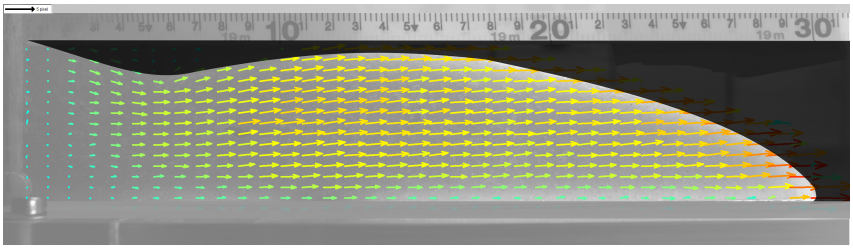

Figure 4.9

Illustration of the velocity fields measured in a flow made with GB^3 and water, during the constant-velocity phase, at the vicinity of the lock gate, and for a moderate concentration.

The particle velocity fields measured in the different flows, made with GB^3 and water for different initial concentrations, reveal that the deposition processes were initiated during the constant-velocity phase, where particles follow a linear trajectory (Figures 4.9), and were delayed with decreasing initial concentrations. The sedimentation was developed behind the flow front, while the deposit took the shape of a wedge that thickens with time until reaching the surface of the suspension overlaid by a layer of water that is not taken into account in the calculations. The surface deposit was gently inclined during the flow and remains approximately constant with time, as exposes the morphology of the final deposit. The flow fronts were typically rounded during propagation while it became progressively more triangular at the end of the flow.

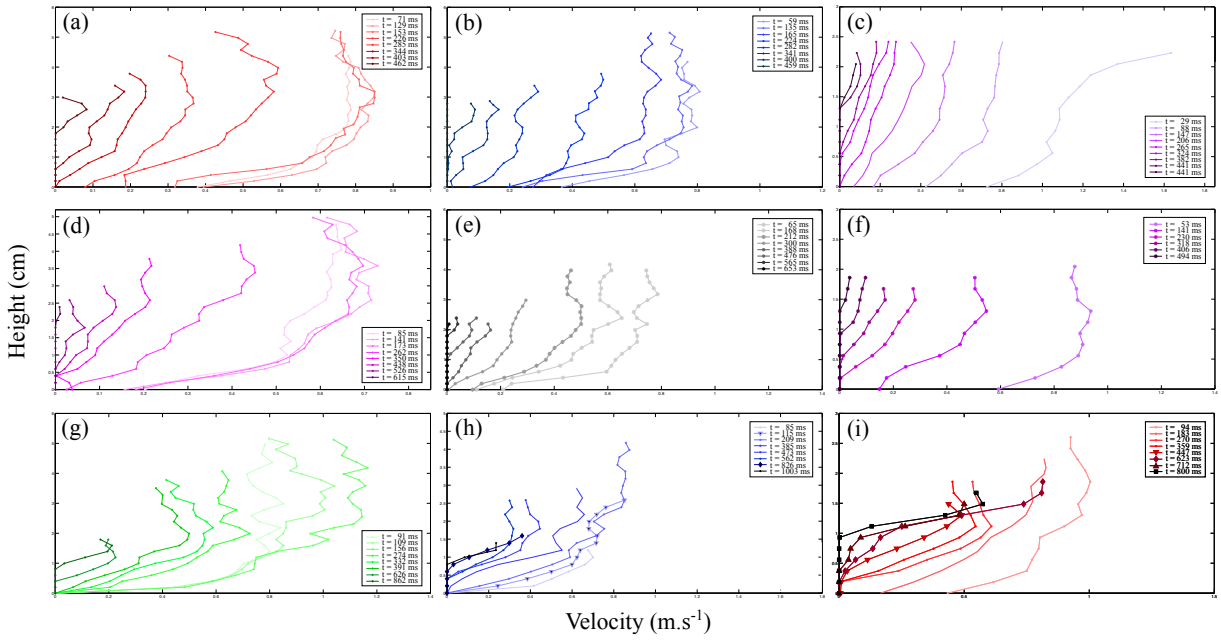

Figure 4.10

Velocity profiles measured in a flow made with GB^3 and water for an initial concentration of : (a), (b), (c) $\phi_s/\phi_{pack} = 0.92$ at $10cm$, $20cm$, and $65cm$ from the lock gate respectively ; (d), (e), (f) $\phi_s/\phi_{pack} = 0.85$ at $10cm$, $20cm$, and $65cm$ from the lock gate respectively ; (g), (h), (i) $\phi_s/\phi_{pack} = 0.70$ at $10cm$, $20cm$, and $65cm$ from the lock gate respectively.

Particle velocity profiles reveal the same flow behavior whatever the initial mixture concentration (Figure 5.9). Before deposition, the profile exhibits a thin basal layer of few millimetres thick where the shear is significant, and overlaid by a thick, slightly sheared, layer in which the velocity is approximately constant. After deposition, the profile evolves with time and thus exhibits a basal deposit layer with no particle motion, overlaid by a moderately- or highly-sheared layer. As the sedimentation is initiated late during the flow, the shear rate remains globally uniform along the flow thickness and weak during the most duration of the flow.

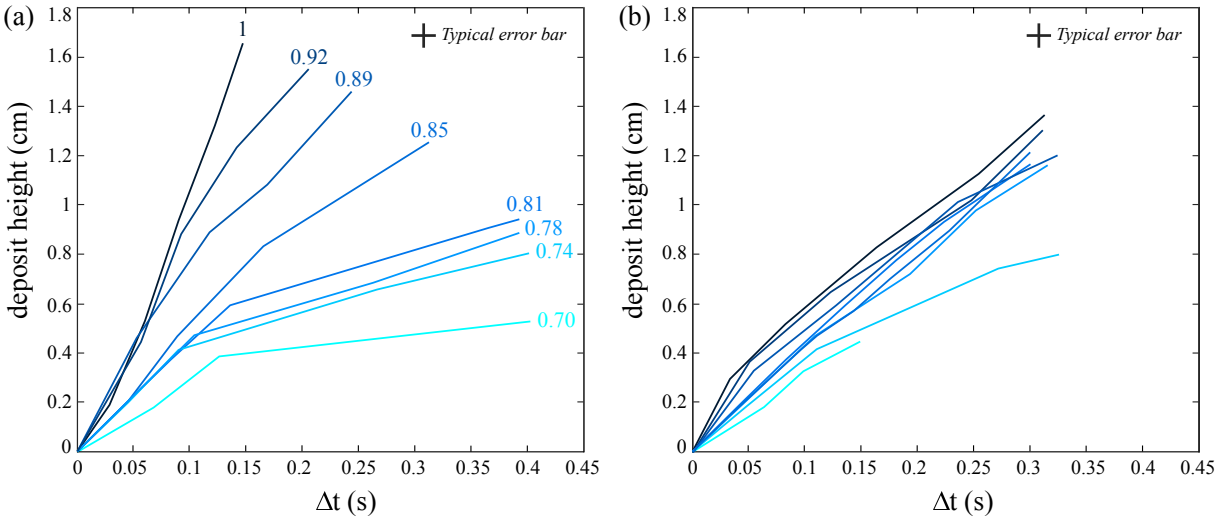

Figure 4.11

Evolution of the deposit thickness, formed at the base of the flows made with GB^3, with time (whose origin corresponds to the onset of sedimentation) for different initial concentrations ϕ_s/ϕ_{pack} indicated by the different values above each curves. Measurements are made (a) at 20 *cm* from the lock-gate and (b) at 70 *cm* from the lock-gate. The dark color represents the flow made at packing while the clear one represents the more dilute flow.

The aggradation processes of the basal deposits were then studied in details, from the viewing windows made with the high-speed video camera located at different distances from the lock gate. Measurements of the bed thickness with time reveal different sedimentation behaviors that evolve with space and time. Here, the time interval $\Delta t = t_{\mathcal{F}} - t_{s0}$

corresponds to the time delay between the passage of the flow front $t_{\mathcal{F}}$ (at the given location) and that of the onset of sedimentation t_{s0}. This representation allows to better compare the aggradation velocities measured from one experiment to another. When measured in the proximal areas (at $20cm$ from the sliding gate), the mean aggradation velocities decrease with decreasing initial concentrations. Only the flow, performed from a packed bed ($\phi_s/\phi_{pack} = 1$), exposes a maximum aggradation velocity that remains constant with time (Figure 5.10a) while decreasing in the distal areas (at $70cm$ from the sliding gate ; Figure 5.10b). For the flows performed from expanded mixtures, characterized by various concentrations, the mean aggradation velocity exposes two phases in the proximal areas. The first one, associated with a high constant rate, is dominant when $\phi_s/\phi_{pack} \geq 0.85$. The second one, associated with a weaker constant rate, is dominant when $\phi_s/\phi_{pack} \leq 0.85$ (Figure 5.10a). In the distal areas, the mean aggradation velocity becomes approximately constant with time and weakly depends on the initial mixture concentration ϕ_s/ϕ_{pack}.

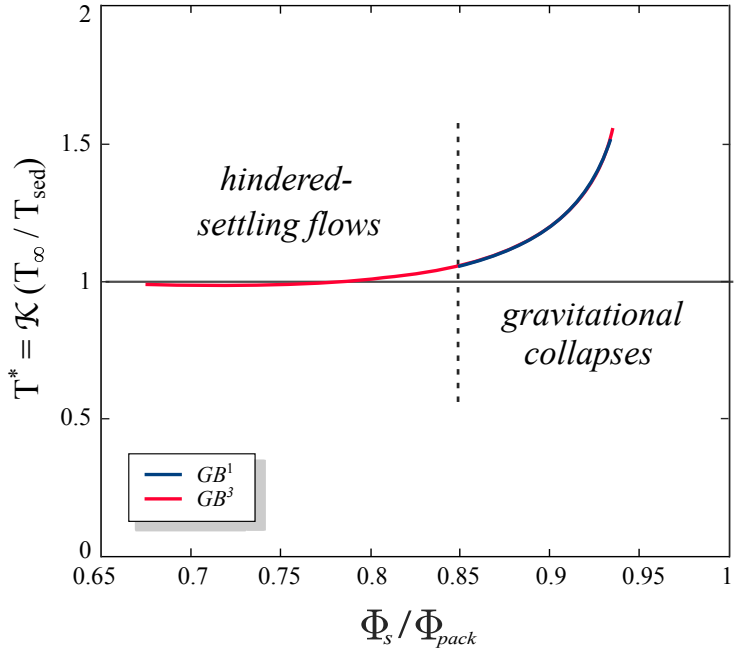

Figure 4.12

Non-dimensional runout time ($T^* = \mathcal{K}T_\infty/T_{sed}$) as a function of ϕ_s/ϕ_{pack}.

Such moving experiments may behave, to a first approximation, as static, slightly horizontally sheared sedimenting suspensions. Plotting the ratio between the runout time T_∞ and the hindered settling time T_{sed}, defined as the ratio between the sedimentation thickness $h_f = h_0 - h_p$ (where h_0 represents the expanded height and h_p : the particles height) and the sedimentation velocity U determined in Chapter 2, also equivalent to the fluidization velocity, allows us to highlight the two different flow regimes (Figure 4.12). When $\phi_s/\phi_{pack} \leq 0.85$, the non-dimensional time tends to unity and means that the flow duration is controled by the sedimentation processes, such as :

$$T_\infty = \mathcal{K}T_{sed} \tag{4.1}$$

where $\mathcal{K} = 0.054$ for GB^1 ; $\mathcal{K} = 0.21$ for GB^3 and represents a coefficient which depends on the properties of the material and the fluid involved in the experiments. When $\phi_s/\phi_{pack} \geq 0.85$, the flow duration may be controled by other parameters, that can be related to the initial gravitational collapse (Figure 4.12).

4.5 Conclusion

We carried out novel dam-break flow experiments of particulate suspensions made with glass beads and water and studied at different initial concentrations ($0.70 < \phi_s/\phi_{pack} < 1$). This work extends that previously developed by Girolami et al. (2008) which consisted in performing similar experiments with gas-solid suspensions. As observed in common dam-break flow experiments, the mixture travels down the flume by defluidizing progressively until motion ceases. The flow front exposes three phases of transport : (1) a brief phase of gravitational acceleration associated with the mixture collapse ; (2) a dominant constant-velocity phase during which the suspension forms progressively a deposit at the base whilst expelling water that forms an upper fluid layer at the surface ; (3) a brief stopping phase. The decrease of the initial mixture concentration ϕ_s/ϕ_{pack} acts in promoting the flow mobility, thus increasing the runout distance and time, as well as forming more elongated and thinner final deposits. The mean flow velocity as well as the frontal velocity both increase with decreasing initial concentrations. This enhanced mobility may be explained by the delay of the particles sedimentation during the flow and the reduced deposit aggradation velocity with decreasing ϕ_s/ϕ_{pack}. In the proximal areas, the deposit thickness, measured within the flow from the high-speed video camera, appears to thicken first rapidly, then more slowly, except at packing where the aggradation velocity is constant and maximum. The duration of the rapid aggradation phase is however shortened with decreasing initial values of ϕ_s/ϕ_{pack}. In distal areas, i.e. far from the lock gate, the aggradation velocity becomes approximately constant with time and almost independent of the initial mixture concentration. Velocity profiles, measured in the flows at different times and locations, reveal the presence of a thin basal sheared layer overlaid by a thick and rapid weakly sheared suspension in the absence of sedimentation, i.e. during the early stages of the flow. Otherwise, when the sedimentation is initiated, the static deposit is overlaid by a moderately sheared suspension. As the velocity profile may be translated upwards, as the deposit aggrades, the results may suggest a time-invariant flow

dynamics. The final deposit shapes suggest two different flow regimes distinguishing the highly concentrated mixtures ($\phi_s/\phi_{pack} \geq 0.85$), with a triangular deposit shape, characterized by a limited mobility dominated by the gravitational collapse and a high expansion rate ; from the less concentrated mixtures ($\phi_s/\phi_{pack} \leq 0.85$) with a trapezoidal deposit shape, characterized by a promoted mobility dominated by hindered settling associated with a weak expansion rate. As previously observed in such dam-break flow experiments, the runout duration of the less concentrated flows ($\phi_s/\phi_{pack} \leq 0.85$) is proportional to the sedimentation time and reveals that their dynamics is principally controled by the sedimentation processes which solely depends on the mixture properties through the initial concentration ϕ_s/ϕ_{pack}. Moreover, such moving experiments may behave, to a first approximation, as static, slightly horizontally sheared sedimenting suspensions.

Bibliographie

Amin A., Girolami L., and F. Risso (2020) On the fluidization/sedimentation velocity of a homogeneous suspension in a low-inertia fluid, Powder Tech., 391, 1-10, doi :10.1016/j.powtec.2021.05.073.

Bougouin A. (2017) Étude expérimentale de l'effondrement d'une colonne fluide-grains, PhD dissertation, Université de Toulouse, Institut National Polytechnique de Toulouse.

Bougouin A., Paris R., Roche O. (2019) Impact of fluidized granular flows into water : implications for tsunamis generated by pyroclastic flows, J. Geophys. Res., doi :10.1029/2019JB018954.

Brooks G.R. and D.E. Lawrence (1999) The drainage of Lake Ha !Ha ! reservoir and downstream geomorphic impacts along Ha !Ha ! River, Saguenay area, Quebec, Canada, Geomorphology, 28, 141-168.

Brooks G.R. (2003) The July 1996 floods in the Saguenay Valley, Quebec, Canada : a case study of the effects of extreme flooding, In : EC Contract EVG1-CT-2001-00037

IMPACT Investigation of Extreme Flood Processes and Uncertainty, Proceedings 3rd Project Workshop, Louvain-la-Neuve, Belgium, 6-7 November 2003 (CD-ROM).

Cantero M.I., J. Lee, S. Balachandar, M.H. Garcia (2007) On the front velocity of gravity currents, J. Fluid. Mech., 586 :1-39, doi :10.1017/S0022112007005769.

Capart H. (2000) Dam-break induced geomorphic flows, PhD thesis, UniversitÈ catholique de Louvain, Louvain-la-Neuve, Belgium.

Capart H., Young D.L. (2002) Two-layer shallow water computations of torrential geomorphic flows, Proceedings of River Flow, Louvain-la-Neuve, Belgium.

Charru F., H. Mouilleron and O. Eiff (2004) Erosion and deposition of particles on a bed sheared by a viscous flow, Journal of Fluid Mechanics, 550, 111-121.

Charru, F. (2006) Selection of the ripple length on a granular bed sheared by a liquid flow, Physics of Fluids, 18, 121508, doi : 10.1063/1.2397005.

Chauchat J. (2007) Contribution à la modélisation diphasique du transport sédimentaire en milieu côtiers et estuariens, PhD dissertation, Université de Caen.

Courrech du Pont S., P. Gondret, B. Perrin., and M. Rabaud (2003) Granular Avalanches in Fluids, Phys. Rev. Let., 90(4), DOI : 10.1103/PhysRevLett.90.044301.

Devauchelle O., L. Malverti, E. Lajeunesse, C. Josserand, P.-Y. LagrÈe, F. MÈtivier (2010) Rhomboid beach pattern : a laboratory investigation (2010), Journal of Geophysical Research : Earth Surface, 115, F2.

Eames I., and M. Gilbertson (2000) Aerated granular flow over a rigid horizontal surface, J. Fluid Mech., 424, 169 ?195.

Fourrière A. (2009) : Morphodynamique des rivières : Sélection de largeur, rides et dunes, PhD thesis, Université Denis Diderot (Paris 7).

Foda M., D. Hill, P. DeNeale, and P.C. Huang (1997) Fluidization response of sediment bed to rapidly falling water surface, Journal of Waterway, Port, Coastal, Ocean Engineering, 123(5), 261-265.

Fraccarollo L. and H. Capart (2002) Riemann wave description of erosional dam-break flows, Journal of Fluid Mechanics, 461, 183-228, doi :10.1017/S0022112002008455.

Girolami L., T.H. Druitt, O. Roche, and Z. Khrabrykh (2008) Propagation and hindered settling of laboratory ash flows, J. Geophys. Res., 113(B2).

Girolami L., Dynamique et sédimentation des écoulements pyroclastiques reproduits en laboratoire, PhD dissertation, Université Clermont-Auvergne, 2008.

Girolami L., O. Roche and T. H. Druitt (2015) Towards a quantitative understanding of pyroclastic flows : Effects of expansion on the dynamics of laboratory fluidized granular flows, J. Volc. Geoth. Res., 296, 31-39, doi :10.1016/j.jvolgeores.2015.03.008.

Girolami L., and F. Risso (2018) Rheological behaviour and runout of short-lived, fast-moving flows of hot dense suspensions, Journal of Energy Challenges and Mechanics, 5(1), 17-23.†

Girolami L., and F. Risso (2019) Sedimentation of gas-fluidized particles with random shape and size, Physical Review, 4, 074301, DOI : 10.1103/PhysRevFluids.4.074301.

Girolami L., and F. Risso (2020) Physical modeling of the dam-break flow of sedimenting suspensions, Physical Review, 5, 084306, DOI : 10.1103/PhysRevFluids.5.084306.

Hogg A. J. (2006) Lock-release gravity currents and dam-break flows, J. Fluid Mech., 569, 61-87.

Hogg A.J., and D. Pritchard (2004) The effects of hydraulic resistance on dam-break and other shallow inertial flows, J. Fluid Mech., 501, 179-212.

Lajeunesse E., J. B. Monnier, and M. Homsy (2005) Granular slumping on a horizontal surface, Phys. Fluids, 17, 1-15, 103302.

Lajeunesse E., Malverti L. and F. Charru (2010) : Bedload transport in turbulent flow at the grain scale : experiments and modeling, Journal of Geophysical Research, 115, F04001.

Lavigne, F. and J. C. Thouret (2000) Les lahars ; depots, origines et dynamique. Bulletin de la Société géologique de France, 171(5), 545-557.

Mulder T., B. Savoye, J. P. M. Syvitski and O. Parize (1997) Des courants de turbidité hyperpycnaux dans la tête du canyon du Var ?, Oceanologica Acta, 20(4), 607-626.

Pailha M. (2009) Dynamique des avalanches granulaires immergées : rôle de la fraction

volumique initiale, PhD dissertation, Université Aix-Marseille, 2009.

Robbe-Saule M., C. Morize, R. Henaff, Y. Bertho, A. Sauret, and P. Gondret (2020) Experimental investigation of tsunami waves generated by granular collapse into water, J. Fluid Mech. 907, 1-23, doi :10.1017/jfm.2020.807.

Roche O., M. A. Gilbertson, J. C. Phillips, and R. S. J. Sparks (2004) Experimental study of gas-fluidized granular flows with implications for pyroclastic flows emplacement, J. Geophys. Res., 109, B10201, doi :10.1029/2003JB002916.

Rondon L., O. Pouliquen and P. Aussillous (2011) Granular collapse in a fluid : role of the initial volume fraction, Phys. Fluids, 23, 073301, doi. : 10.1063/1.3594200.

Rottman J. W. and J.E. Simpson (1983) Gravity currents produced by instantaneous releases of a heavy fluid in a rectangular channel, Journal of Fluid Mechanics, 135, 95-110.

Shimizu H. A., T. Koyaguchi, and Y.J. Suzuki (2017) A numerical shallow-water model for gravity currents for a wide range of density differences, Prog. Earth Planet. Science, 4 :8, doi :10.1186/s40645-017-0120-2.

Shimizu H. A., T. Koyaguchi, and Y.J. Suzuki (2019) The run-out distance of large-scale pyroclastic density currents : A two-layer depth-averaged model, J. Volc. Geoth. Res., 381 (2019) 168 ?184.

Simpson J.E. (1997) Gravity Currents in the Environment and the Laboratory, 2^{nd} ed., Cambridge Univ. Press, New York.

Thouret, J. C., S. Antoine, C. Magill, and C. Ollier (2020) Lahars and debris flows : Characteristics and impacts, Earth-Science Reviews, 201, 103003.

Vallance, J. W. and R. M. Iverson (2015) Lahars and their deposits, In The encyclopedia of volcanoes, Academic Press, pp. 649-664.

Zech Y., S. Soares-Frazao, B. Spinewine and N. Le Grelle (2010) Dam-break induced sediment movement, Journal of Hydraulic Research, 46(2), 176-190.

Chapitre 5

Transport and deposition of immersed suspension-flows

Abstract

We carried out novel experiments of turbidity currents involving particulate suspensions made with glass beads and water at different concentrations ($0.48 < \phi_s/\phi_{pack} < 1$). When released, the mixture rapidly develops a basal suspension that progressively forms a deposit at the base, overlaid by a dilute wake in which the incorporation of water drives to the formation of large-scale eddies that erode particles from the underflow. The kinematics of the front exposes three phases of transport independently of the initial conditions : (1) a brief phase of gravitational acceleration ; (2) a dominant constant-velocity phase ; (3) a final stopping phase. As a result, the mean flow velocity is of the same order of magnitude for the two layers ($\simeq 0.33\ m.s^{-1}$) and remains quasi-independent of the initial conditions. The decrease of the initial values of ϕ_s/ϕ_{pack} acts in promoting the flow mobility, slightly increasing the runout distance and duration of the suspension ; more significantly that of the wake until $\phi_s/\phi_{pack} \geq 0.65$. Aggradation velocities, measured in the suspensions, decrease with decreasing values of ϕ_s/ϕ_{pack} and traveled distances, while

those measured from the wake remain quasi-independent of the initial conditions. Velocity profiles, measured in the flows at different times and locations, reveal the presence of a thin basal sheared layer overlaid by a thicker one whose shear has an opposite sign. After deposition, the profiles evolve with time and space, exposing a thicker basal layer and a thinner upper one in which both positive and negative gradients reflect the development of smaller coherent structures of mixing, that finally tend to homogenize the flow at the end of experiment. The trapezoidal deposits highlight the rapid sedimentation of the suspension followed by the progressive deposition of the dilute wake. As previously observed in such dam-break flow experiments, the runout duration of the less concentrated suspensions ($\phi_s/\phi_{pack} < 0.85$) is proportional to the sedimentation time and reveals that their dynamics is principally controled by the hindered settling processes, while that of the wake may be controled by the time taken by a particle to sediment in a pure, static fluid from an initial height h_0 reduced by a factor of water ingestion.

5.1 Introduction

The formation of hyperpycnal currents is mainly observed in medium-sized rivers (i.e. with a mean flow rate less than 460 $m^3.s^{-1}$) following a significant, rapid increase of the solid discharge (i.e. clay sediments) during a series of flash floods or a dam-failures. These concentrated flows turn out to be the origin of long-lived (from several days to several weeks) turbidity currents once immersed into the sea [Mulder et al., 1997]. Such highly-erosive currents can explain the occurence of submarine thalwegs that sharply incise the deltaic shelfs and the formation of large meandering channel-levee systems. By flowing down continental slopes, they rapidly transform into highly-stratified currents composed of a basal debris-flow which is commonly guided by the topography and an upper dilute surge which can detach from its base and adopt a highly unpredictible behavior [Migeon et al., 2012] similarly to the processes observed in pyroclastic density currents during volcanic eruptions [Doyle et al., 2007 ; Girolami et al., 2008]. Such

extreme events involving a large-volume of sediments (i.e. from tens to hundreds of km^3) can damage communication cables and pipelines as well as generating tsunamis able to affect the coastal and offshore infrastructures [Migeon et al., 2011]. As a result, the human toll can be particularly heavy whilst the destructive effects including ecological consequences can continue many decades after the disaster itself such as the financial costs associated with such catastrophes become ultimately invaluable. The case of the Nice harbour catastrophe (France), occurred on October 16^{th} 1979, is one of the most striking examples (Figure 5.1). During land filling operations, a part of the new harbour located at the edge of the international airport collapsed into the sea (Figure 5.1a), involving a significant volume (around 8.7 10^6 m^3) of sediments located at the vicinity of the Var outlet which previously experienced exceptional heavy rainfall events. The turbidity current, transported over hundreds of kilometers, caused the formation of a tsunami (up to 3-m-high) which swept the city of Antibes (Figure 5.1b) while the nearby Monaco Observatory did not register any earthquake (which could have triggered the failure) at that time [Dan et al., 2007]. This event caused the death of ten people and the destruction of two communication cables located at hundreds of kilometers far from the coastal line [Yang et al., 2001]. Thereafter, many scientific efforts (principally based on field observations and measurements) focused on the Var turbiditic system which became a natural laboratory particularly well suited for the investigation of problems of slope instability [Migeon et al., 2012 and references therein] where three types of flows can be distinguished [Mulder et al., 1997] :

- hyperpycnal currents (few km^3) which ensure the direct transfer of a large volume of clay sediments from anthropized rivers to sedimentary basins with a return period of 2-20 years [Mulder et al., 1997] ;

- small-volume avalanches ($<$ hundreds of m^3) which ensure the transfer of coarser sediments down the slope through low-density turbidites. They represent common phenomenon inducing more subtle morphological changes

with a return period of 7 years [Kelner et al., 2014] ;

- large-volume collapses (> hundreds of km^3) which ensure the transfer of polydisperse sediments from the shelf to sedimentary basins through varying-density turbidites. They represent rare events able to drastically change the margin morphology with a return period of thousands of years [Migeon et al., 2012].

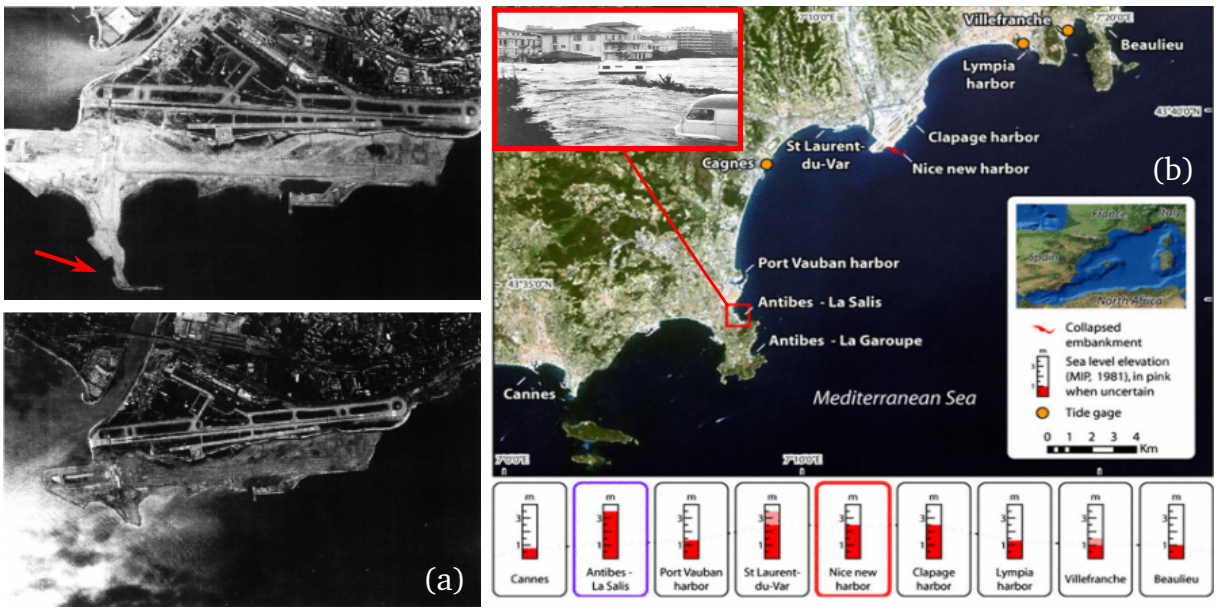

Figure 5.1

Pictures of (a) the harbour-airport complex before and after the 1979 catastrophe ; (b) Records of the sea level elevation at different locations pointing the tsunami that swept the city of Antibes. The pictures are modified from Silva Jacinto et al. [2014].

Sultan et al. [2004] first focused on the origin of the second type of flows which represent the dominant process of sediments transfer in passive margins (i.e. where the seismic activity is significantly reduced). From geotechnical analysis made on a series of

turbidite samples, they inferred that the failure initiation can be explained by a modification of the mechanical properties (i.e. material compacity, fluidization) associated with the accumulation of poorly consolidated sediments after flash floods near the river outlet or the in-depth recirculation of freshwater.

Iverson [2005] first explored the role of the volumic fraction of sediments on the dynamics of debris flows using a large-scale dam-break flume (i.e. of few hundred meters long built at the Geological Survey of United-States USGS) in order to get reliable measurements of the fluid pore-pressures during propagation. However, the difficulty and costs of such operations strongly limited the number of experiments. Pailha et al. [2008] thus pursued this study using less expensive small-scale analog experiments in order to get a more detailed analysis. They observed that loose packed sediments may collapse instantaneously while dense packed ones systematically record a delay corresponding to the time necessary for the material dilatance (i.e. up to 25 vol %) and the development of a pore pressure in the fluid phase. While the problems of slope stability played by the sediments compacity has been recently explored, those related to the fluidization effects inferred from field observations and measurements [Dan et al., 2007 ; Kelner et al., 2014] received less attention. Recent laboratory experiments have however pointed their crucial role in aerian avalanches (i.e. pyroclastic flows and surges that propagate down valleys [Girolami et al., 2008 ; 2010]) which may yet look like to debris flows and turbidity currents that propagate down submarine canyons. Despite a large literature devoted to experimental turbidity currents [Meiburg & Kneller, 2010 and references therein ; and more recently Rondon et al., 2011 ; Bougouin, 2017 ; Bougouin et al., 2019 ; Robbe-Saule et al., 2021], no laboratory experiments have been proposed until now to properly identify the role of the initial mixture concentration, varied in a wide range of values thanks to the fluidization technics, on the dynamics of immersed avalanches. Moreover, recent field analysis have also highlighted the role of the mixture rheology on the flow transformation [Migeon et al., 2013] and its resulting hazardous nature as well as the coupling between the immersed avalanche and dynamics of the wave that impede the improvement of large-scale

simulations [Ioualalen et al., 2010]. Such issues may help in significantly improve the predictions of both small- and large-volume avalanches that are frequently recorded in the Nice continental slope as well as their tsunamigenic potential.

5.2 Experimental methods

5.2.1 The dam-break flume

The experiments were carried out in the dam-break flume previously used for the realization of the free-surface flows. The experimental procedures and methods were similar to those described in the previous chapter. The material was first poured into the rectangular reservoir of 10-cm-long, 30-cm-wide, and 70-cm-high, thus fluidized and uniformly expanded before being released. Even if the spillway was no more useful here, the height of the expanded mixture was maintained to $h_0 = 31\ cm$ above the porous medium in each experiment, while henceforth overlaid by a column of water, high enough to discard from the free-surface effects. Similarly, the channel was entirely filled with water. During the preparation of the experiments, the solid volume fraction of the bed at packing was first measured by repeating fluidization and defluidization procedures, as well as measuring the bed mass and particles density. Once characterized, the bed was expanded to a given rate that varied from one experiment to another by modifying the height of particles introduced initially. Increasing the initial expansion rate, by decreasing the particle height h_p, amounts to decrease the mixture concentration ϕ_s/ϕ_{pack}. The incoming fluid rate was measured with the magnetic flowmeter with an accuracy of 0.01 $L.min^{-1}$, whilst its temperature was measured at the beginning and the end of each experiment in order to properly determine the fluid viscosity. The opening of the sliding gate was made thanks to the hydraulic cylinder, and simultaneously to the stop of fluidization. The mixture was then released down the flume and formed a fast-moving, but short-lived, turbidity current that defluidized progressively until motion ceased (Figure 5.2a). At the end of the

experiment, the deposit morphology was measured every $5cm$ from the lock-gate.

As the experiments were also reproducible, the flow was first recorded with the semi-fast camera to get a global view of around 1.5-m-wide ; then repeated, using a high-speed video camera, to get a series of viewing windows of 50-cm-wide in order to study the internal flow structures and determine the velocity profiles, as well as the aggradation velocities of the basal deposit formed during travel.

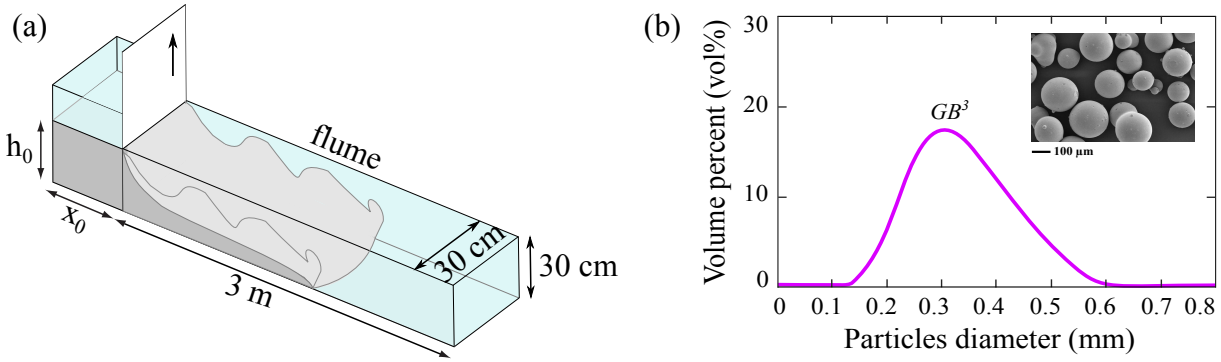

Figure 5.2

(a) Illustration of the immersed flows reproduced in this configuration. (b) Grain-size distribution of the glass-beads used in these experiments.

5.2.2 The synthetical materials

In these experiments, one sample of glass beads, termed GB^3 in the previous studies, was used (Table 5.1).

$Materials$	d_{50} (μm)	ρ $(kg.m^{-3})$	ϕ_{pack}	h_p (cm)	h_0 (cm)	ϕ_s/ϕ_{pack}
GB^3	337	2496	0.58	$15-31$	31	$0.48-1$

Table 5.1

Mean features of the material and suspensions involved in the dam-break flow experiments.

This selection was motivated by the observation step, made from the high-speed video recordings, that is greatly improved with the coarsest particles. To ensure a satisfying

contrast, around 20% of glass beads were also tinted with a permanent black paint and used as passive tracers. As exposed previously, glass beads have a quasi-spherical shape (Figure 5.2b). The material was initially sieved to reduce its granulometric distribution and prevent the development of segregation during experiments. A first sieving was performed to discard the dusts, while a second one allowed to discard the particle clusters. In this way, no size-segregation was develop during the fluidization and propagation. Once sieved, a representative sample of the material batch was prepared with a splitter, then dried, and analyzed with a laser granulometer to get the grain-size distribution (Figure 5.2b) as well as the particle equivalent diameter d_{50}, as reported in Table 5.1.

5.2.3 The reproducibility of experiments

To ensure the realization of viewing windows for the study of sedimentation processes without disturbing the recording of the global flow, from which the frontal position is measured, the experiments were carefully repeated 5 times taking similar initial conditions.

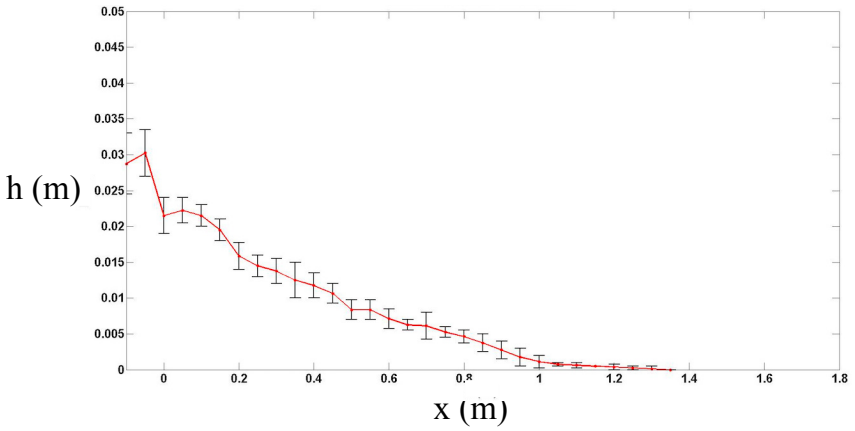

Figure 5.3

Illustration of the mean deposit morphology obtained from 5 repeated experiments, thus including the error bar. This example corresponds to the deposits of GB^3 when $\phi_s/\phi_{pack} = 0.55$.

The repetition of the experiments allowed us to determine the error bars for each

measurement presented in the global description, such as the runout length and time, the mean velocity, as well as the deposit morphology. Figure 5.3 exposes the mean deposit morphology obtained from 5 experiments, thus including the error bar deduced from the results. From one experiment to another, we have considered that the reproducibility of the experiments was reliable enough to ensure a measurement of quality associated with a satisfying measurement uncertainty.

5.3 The general flow behavior

When released, the suspension of glass beads flows down the flume by forming a turbidity current that travels at speeds of up to 0.35 $m.s^{-1}$ and defluidizes progressively until motion ceases (Figure 5.4a). During travel, the suspension instantaneously develops internal structures that divides the flow into three vertical layers (Figure 5.4b) : (1) a basal deposit that aggrades progressively during the flow, (2) a short-lived flowing suspension that thins rapidly from upwards and downwards, and (3) a long-lived dilute layer, termed *wake*, in which particles are entrained from the underlying suspension and mixed as eddies by the water incorporation from above.

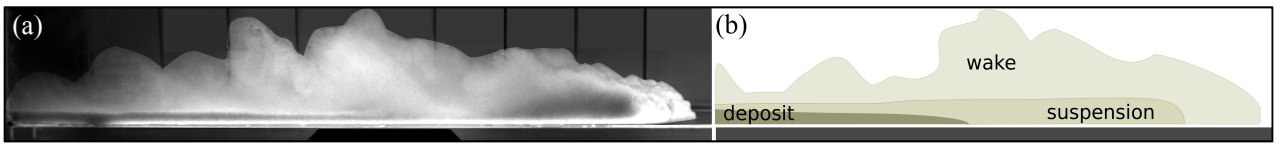

Figure 5.4

(a) Picture of the immersed turbidity current made with glass beads and water. (b) Illustration of the internal structures instantaneously developed during propagation.

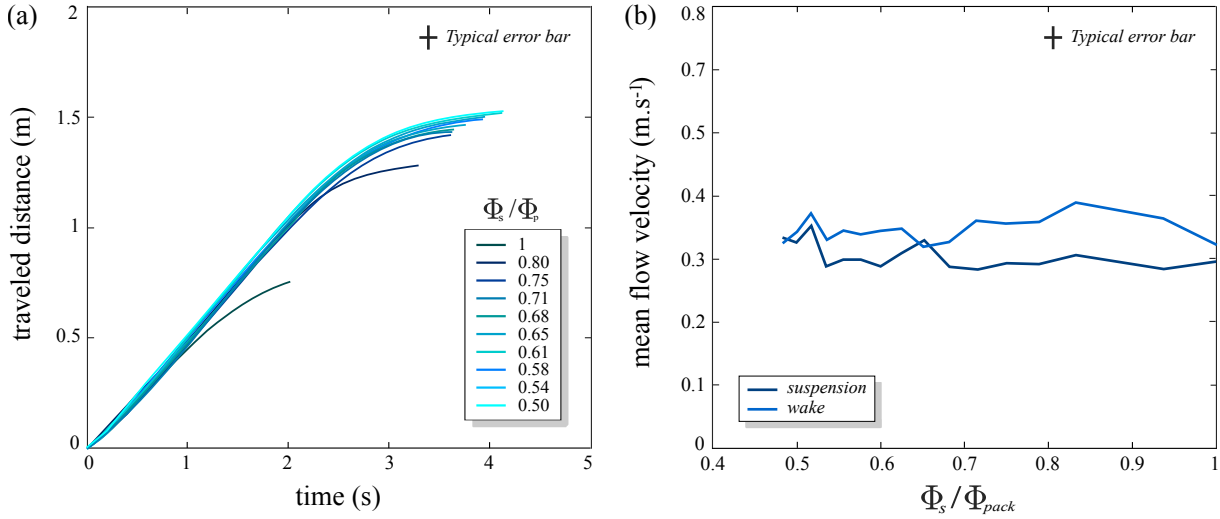

Figure 5.5

(a) Position of the flow front with time ; (b) mean flow velocity measured in all experiments involving GB^3.

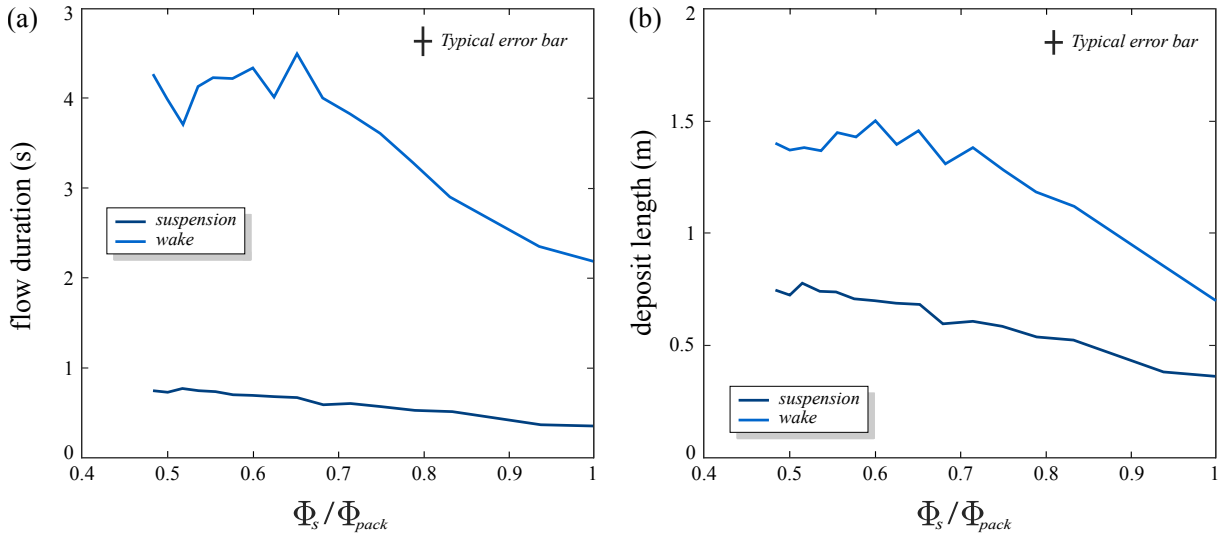

Figure 5.6

(a) Flow duration and (b) runout distance as a function of the initial mixture concentration ϕ_s/ϕ_{pack} for all experiments made with GB^3.

As observed in analog free-surface flows, sedimentation processes take place during

transport, but in a more rapid manner, such as the motion ceases first at the rear of the flow, then at the front. The runout time and length are principally controled by the wake propagation. The frontal position also exposes three phases of transport : (1) a brief initial acceleration phase that lasts around 0.2 s ; (2) a dominant constant-velocity phase that lasts around $1-2$ s ; and (3) a stopping phase that lasts around $0.5-1s$ (Figure 5.5). Surprisingly, the duration of the different phases as well as the kinematics are almost independent of the initial mixture concentration ϕ_s/ϕ_{pack}, when $\phi_s/\phi_{pack} \geq 0.80$. The mean flow velocity, both measured for the dense suspension and the dilute wake, is slightly upper for the wake but of the same order of magnitude (around 0.35 $m.s^{-1}$ for the wake against 0.30 $m.s^{-1}$ for the suspension), while remaining quasi-independent of ϕ_s/ϕ_{pack}.

As previously observed in free-surface flows, the mixture mobility increases with decreasing values of ϕ_s/ϕ_{pack}. The total duration T and the final distance traveled by the suspension L both slightly increase, and quasi-linearly, with decreasing concentrations, while greatly increase for the wake until a threshold fixed at $\phi_s/\phi_{pack} \simeq 0.65$ above which the mobility becomes independent of the initial conditions (Figure 5.6).

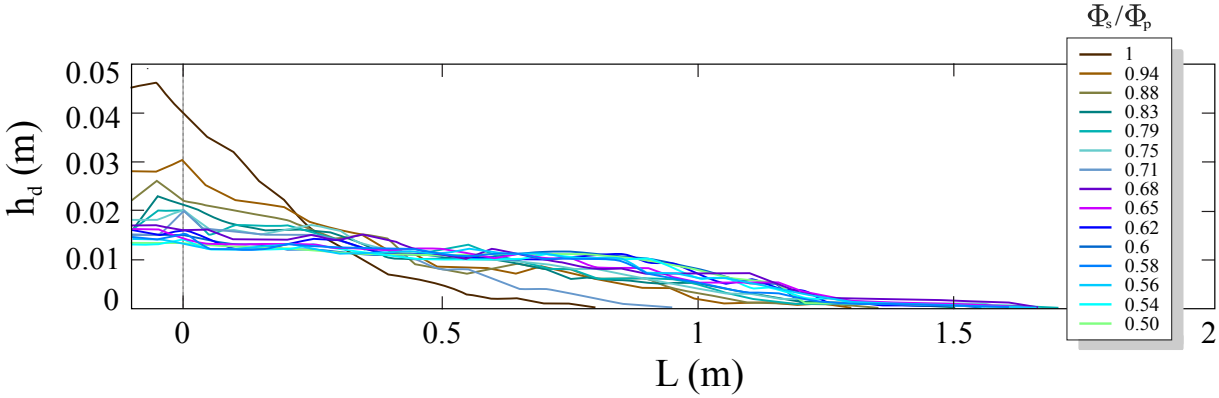

Figure 5.7

Morphology of the deposits let by each turbidity current performed with GB^3.

At the end of each experiment, the deposit let by the flow has a trapezoidal shape which is more elongated at low initial values of ϕ_s/ϕ_{pack} (Figure 5.7). When $\phi_s/\phi_{pack} \geq$

0.65, the deposits take the shape of a troncated cone or a mexican hat, as observed in dry granular avalanches [Lajeunesse et al., 2005], which may be principally guided by the suspension sedimentation, while slightly sprinkled by the wake deposition. Otherwise, when $\phi_s/\phi_{pack} \leq 0.65$, the deposits take the shape of a spread-out heap, almost triangular, which may be guided by the wake deposition and whose morphology does not depend anymore on the initial conditions.

5.4 The internal flow structures

The flow dynamics was thus explored by determining the velocity fields and profiles, as well as the aggradation velocities from the viewing windows performed at 20 *cm* and 60 *cm* from the lock gate. As exposed previously, the calculation of the velocity fields require the four different steps reminded here :

1. **a geometric mask :** focused on the passage of the flow and allowed to discard us from the background in the calculations.
2. **a time filter :** a time filter was applied to the studied area in order to remove some static points or objects which affect the measurement.
3. **the PIV processes :** the calculation of the velocity fields was done by dividing the studied area into a square mesh of 96 pixels, and then into a circular mesh of 32 pixels.
4. **the post processing step :** the post-processing step aims at correlating some unconsistent vectors with those located around them.

The particle velocity fields measured in the flows, made with GB^3 and water for different initial concentrations, reveal a quasi-linear trajectory in the suspension part that introduces a topography within the flow that guide particles located above to travel around it, while the upper mixture layer develops large-scale eddies (Figures 5.8).

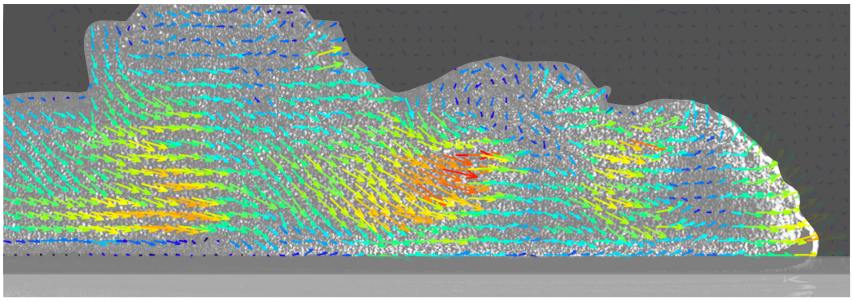

Figure 5.8

Illustration of the velocity fields measured in a turbidity current made with GB^3 during the constant-velocity phase, at the vicinity of the lock gate, and for a moderate concentration.

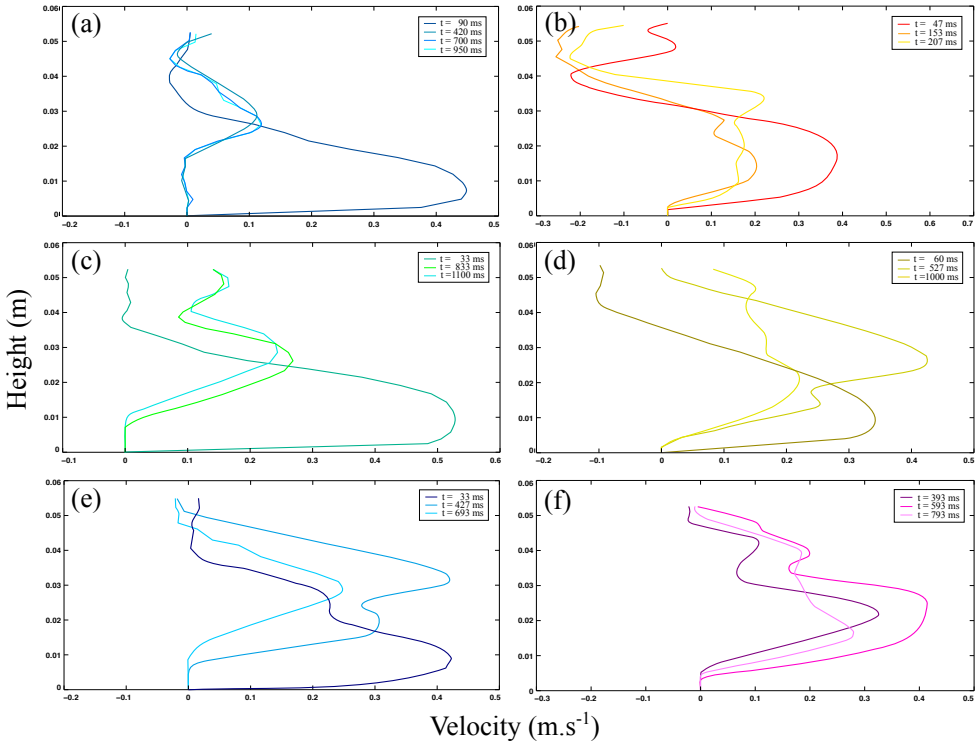

Figure 5.9

Velocity profiles measured in turbidity currents made with GB^3 for an initial concentration of : (a), (b) $\phi_s/\phi_{pack} = 0.87$ at 20 cm and 60 cm from the lock gate respectively ; (c), (d) $\phi_s/\phi_{pack} = 0.77$ at 20 cm and 60 cm from the lock gate respectively ; (e), (f) $\phi_s/\phi_{pack} = 0.58$ at 20 cm and 60 cm from the lock-gate respectively.

Once the suspension has sedimented, the flow is limited to the propagation of the wake whose deposition is delayed by the incorporation of water at a velocity that may be described as an entrainment velocity, as introduced in the modeling of volcanic plumes which incorporate a significant quantity of ambient air during ascent [Kaminski et al., 2005].

Particle velocity profiles were measured at different times in turbidity currents for $\phi_s/\phi_{pack} = 0.87; 0.77; 0.58$, at the vicinity of the gate (20 cm) or at midway to the final distance traveled by the flow (60 cm). At the early times of propagation, the velocity profile exposes a classical shape, with a inner (near-wall) region characterized by a positive velocity gradient which looks like to a turbulent boundary layer, and an outer region (sheared layer), generally 5-10 times thicker than the inner one and characterized by a negative velocity gradient and shear of opposite sign, as exposed in the literature [Meiburg & Kneller, 2010]. After deposition, the profile evolves with time and exhibits a thicker inner region and a thinner outer layer in which both positive and negative gradients reflect the development of smaller coherent structures of mixing and eddies. In distal areas, the profile still exhibits a well defined inner and outer region before sedimentation, while becoming a superposition of small eddies after deposition that finally tend to homogenize the layer at the end of experiment.

The mean aggradation velocity U_{agg} of the basal deposit was then determined from the viewing windows made with the high-speed video camera, both for the suspension (at 20 cm and 60 cm from the lock-gate) and for the wake (at 60 cm from the lock-gate). As observed in the reservoir, the aggradation velocity of the suspension linearly decreases with decreasing mixture concentration, from 4.7 $cm.s^{-1}$ when $\phi_s/\phi_{pack} = 0.94$ to 2.3 $cm.s^{-1}$ when $\phi_s/\phi_{pack} = 0.48$ (Figure 5.10). The velocity U_{agg} also decreases with distance from reservoir, from 3.4 $cm.s^{-1}$ near the gate to 1.8 $cm.s^{-1}$ at 60 cm away when $\phi_s/\phi_{pack} = 0.75$; and from 2.3 $cm.s^{-1}$ near the gate to 1 $cm.s^{-1}$ at 60 cm away when $\phi_s/\phi_{pack} = 0.48$. As expected, the wake deposit aggrades more slowly than the suspension ($U_{agg} \simeq 0.5$ $cm.s^{-1}$) and at a velocity independent of ϕ_s/ϕ_{pack} (Figure 5.10).

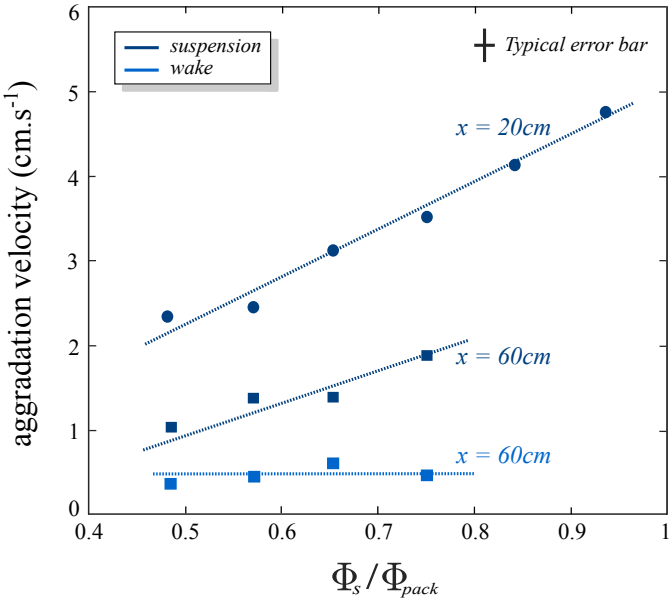

Figure 5.10

Aggradation velocities of the basal deposit with different mixture concentrations ϕ_s/ϕ_{pack}. Measurements are made at both 20 cm and 60 cm from the lock-gate.

The flow duration is then studied by plotting the ratio between the runout time T_∞ and the sedimentation time T_{sed} as a function of the initial mixture concentration ϕ_s/ϕ_{pack} that tends to unity (Figure 5.11). For the suspension, T_{sed} is defined as the ratio between the sedimentation thickness $h_f = h_0 - h_p$ (where h_0 represents the expanded height and h_p : the particles height) and the hindered settling velocity U_f, also equivalent to the fluidization velocity, which means that :

$$T_\infty = \mathcal{K} T_{sed} \tag{5.1}$$

where $\mathcal{K} = 0.21$ represents a coefficient which depends on the properties of the material and the fluid involved in the experiments. As observed in free-surface flows, the flow duration is principally controled by the hindered settling processes for the suspension, when $\phi_s/\phi_{pack} \leq 0.85$; otherwise the duration may be controled by the gravitational collapse (Figure 5.11a).

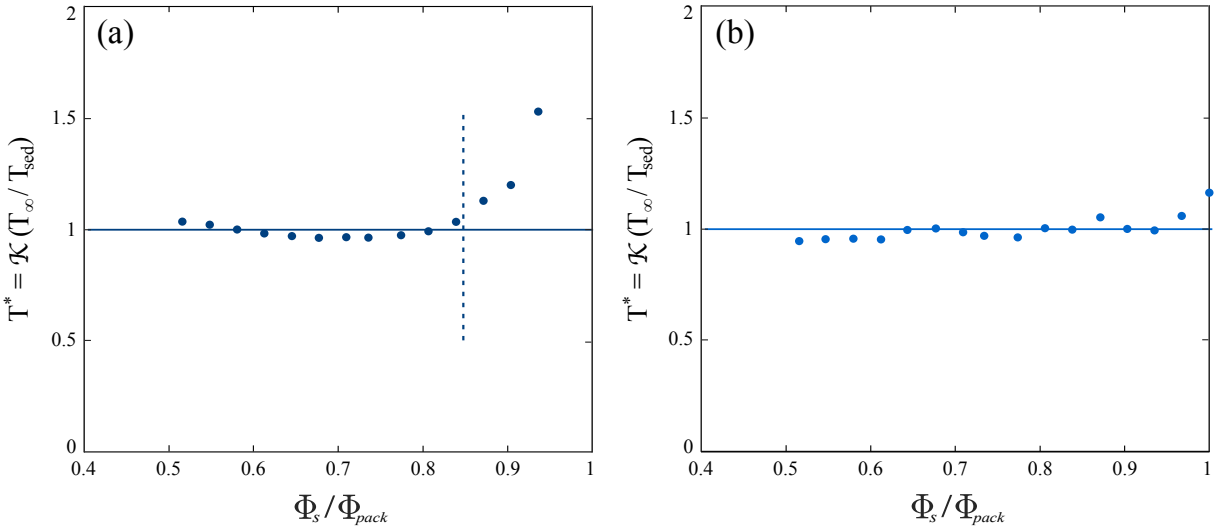

Figure 5.11

Non-dimensional runout time ($T^* = \mathcal{K}T_\infty/T_{sed}$) as a function of ϕ_s/ϕ_{pack} for (a) the suspension and (b) the wake.

For the wake, $T_{sed} = T_0$ is defined as the ratio between the fall height h_0 and the Stokes velocity $U_0 = \frac{g(\rho_p - \rho_f)d_p^2}{18\mu_f}$, which means that :

$$T_\infty = \alpha_e T_0 \tag{5.2}$$

where $\alpha_e = 0.123$ may correspond to the entrainment coefficient introduced to describe the water incorporation in experimental plumes made with particles and water [Papanicolaou & List, 1988 ; Wang & Law, 2002]. As exposed in Figure 5.11b, the wake duration is thus principally controled by the particles deposition that may be balanced by the effect of water ingestion through the entrainment coefficient.

5.5 Conclusion

We carried out novel experiments of turbidity currents made from homogenous particulate suspensions of glass beads and water and studied at different initial concentrations ($0.48 < \phi_s/\phi_{pack} < 1$). When immersed into water, the dam-break avalanches travel in a

different way than their analog free-surface flows. During propagation, the mixture rapidly develops internal structures : an inner region made with a dense suspension that progressively forms a deposit at the base, overlaid by an outer sheared layer made with some particles entrained by the formation of large-scale eddies due to the water incorporation and mixing during travel. As the suspension, located at the rear of the flow, sediments rapidly, the flow runouts are principally governed by the wake propagation which forms the frontal region and the upper body. Similarly to the dam-break experiments, the flow front exposes three phases of transport : (1) a brief initial acceleration phase ; (2) a dominant constant-velocity phase ; and (3) a final stopping phase. Surprisingly, the duration of these different phases as well as the flow kinematics are almost independent of the initial mixture concentration. The mean velocity of both the suspension and the wake remains of the same order of magnitude (around $0.33m.s^{-1}$ and quasi-independent of ϕ_s/ϕ_{pack}. As previously observed in free-surface flows, the suspension mobility linearly increases with decreasing values of ϕ_s/ϕ_{pack}, but in a quite slighter manner ; while that of the wake significantly increases until a threshold value of $\phi_s/\phi_{pack} \geq 0.65$ above which the mobility becomes independent of the initial conditions. Aggradation velocities of the suspension both decrease with decreasing values of ϕ_s/ϕ_{pack} and with increasing traveled distance ; while remaining approximately constant for the wake, whatever the initial conditions. At the early stage of the flow, particle velocity profiles expose a classical shape with a positive velocity gradient in the near-wall layer (as in a turbulent boundary layer) overlaid by a thicker layer with a negative velocity gradient and shear of opposite sign. After deposition, the profiles evolve with time and space and exhibit a thicker inner region and a thinner outer layer in which both positive and negative gradients reflect the development of smaller coherent structures of mixing, that finally tend to homogenize at the end of experiment. The deposits morphology reveal two different flow regimes. Above $\phi_s/\phi_{pack} \geq 0.65$, deposits have the shape of a troncated cone which may be principally guided by the sedimentation of the suspension. Under $\phi_s/\phi_{pack} \leq 0.65$, deposits have a triangular shape, with gentle slope, and may be principally guided by the wake deposition.

As previously observed in such dam-break flow experiments, the runout duration of the less concentrated suspensions ($\phi_s/\phi_{pack} \leq 0.85$) is proportional to the sedimentation time and reveals that their dynamics is principally controled by the hindered settling processes which solely depends on the mixture properties, while that of the wake may be controled by the time taken by a particle to sediment in a pure static fluid from an initial height h_0, but delayed by a coefficient that includes the water incorporation effects.

Bibliographie

Bougouin A. (2017) Étude expérimentale de l'effondrement d'une colonne fluide-grains, PhD dissertation, Université de Toulouse, Institut National Polytechnique de Toulouse.

Bougouin A., Paris R., Roche O. (2019) Impact of fluidized granular flows into water : implications for tsunamis generated by pyroclastic flows, J. Geophys. Res., doi :10.1029/2019JB018954.

Dan G., N. Sultan and B. Savoye (2007) The 1979 Nice harbour catastrophe revisited : Trigger mechanism inferred from geotechnical measurements and numerical modelling, Marine Geology, 245, 40-64.

Doyle E. E. (2007) Analogue and numerical modelling of gravity currents and pyroclastic flows, PhD thesis, University of Bristol.

Girolami L., T.H. Druitt, O. Roche, and Z. Khrabrykh (2008) Propagation and hindered settling of laboratory ash flows, J. Geophys. Res., 113(B2), doi :10.1029/2007JB005074.

Ioualalen M., S. Migeon and O. Sardou (2010) Landslide tsunami vulnerability in the Ligurian Sea : Case study of the October 16th 1979 Nice airport submarine landslide and of identified geological mass failures, Geophysical Journal International, 181(2), 724-740.

Iverson R. M. (2005) Regulation of landslide motion by dilatancy and pore-pressure feedback, J. Geophys. Research, 110, F2015.

Kaminski, E., S. Tait, S., and G. Carazzo (2005) Turbulent entrainment in jets with arbitrary buoyancy. J. Fluid Mechanics, 526, 361-376.

Kelner M., S. Migeon, E. Tric, F. Couboulex, A. Dano, T. Lebourg and A. Taboada (2014) Recent Morphological Changes of the Nice Continental Slope, Engineering Geology for Society and Territory, 4, 221-225.

Lajeunesse E., J. B. Monnier, and M. Homsy (2005) Granular slumping on a horizontal surface, Phys. Fluids, 17, 1-15, 103302.

Meiburg E. and B. Kneller (2010) Turbidity currents and their deposits, Annual Review of Fluid Mechanics, 42, 135-156.

Migeon S., A. Cattaneo, V. Hassoun, C. Larroque, N. Corradi, F. Fanucci, A. Dano, B. Mercier de Lepinay, F. Sage and C. Gorini (2011) Morphology, distribution and origin of recent submarine landslides of the Ligurian Margin (North-western Mediterranean) : Some insights into geohazard assessment, Marine Geophysical Research, DOI 10.1007/s11001-011-9123-3.

Migeon S., A. Cattaneo, V. Hassoun, A. Dano, A. Casedevant and E. Ruellan (2012) Failure Processes and Gravity-Flow Transformation Revealed by High-Resolution AUV Swath Bathymetry on the Nice Continental Slope (Ligurian Sea), Submarine Mass Movements and Their Consequences : Advances in Natural and Technological Hazards Research, 31, 451-461.

Mulder T., B. Savoye, J. P. M. Syvitski and O. Parize (1997) Des courants de turbidité hyperpycnaux dans la tête du canyon du Var ?, Oceanologica Acta, 20(4), 607-626.

Pailha M., M. Nicolas and O. Pouliquen (2008) Initiation of underwater granular avalanches : Influence of the initial volume fraction, Physics of Fluids, 20 (11).

Papanicolaou P. N. and E. J. List (1988) Investigations of round vertical turbulent buoyant jets, J. Fluid Mech. 195, 341-391.

Robbe-Saule M., C. Morize, R. Henaff, Y. Bertho, A. Sauret, and P. Gondret (2020) Experimental investigation of tsunami waves generated by granular collapse into water, J. Fluid Mech. 907, 1-23, doi :10.1017/jfm.2020.807.

Rondon L., O. Pouliquen and P. Aussillous (2011) Granular collapse in a fluid : role of the initial volume fraction, Phys. Fluids, 23, 073301, doi. : 10.1063/1.3594200.

Silva Jacinto R., S. Garziglia and N. Sultan (2014) L'étude des glissements sous-marins et la génération de tsunami, cas du glissement de Nice en 1979, Workshop on Littoral Risks and Tsunamis, CFGI-Ifremer.

Sultan N., P. Cochonat, J-P Foucher and J. Mienert (2004) Triggering mechanisms of slope instability processes and sediment failures on continental margins, Marine Geology, 213, 291-321.

Wachs A., L. Girolami, G. Vinay and G. Ferrer (2012) GRAINS3D, a flexible DEM approach for particles of arbitrary convex shape, Powder Technology, DOI :10.1016/j.powtec.2012.03.023.

Yang F., J. Barral, T. Prevost, P.-Y. Laligand, N. Massart, V. Schmitt, E. Ollinger (2001) Génération de tsunamis : Nice, 16 Octobre 1979, Projet Scientifique, Ecole Polytechnique.

Wang H. and A. W. K. Law (2002) Second-order integral model for a round turbulent buoyant jet, J. Fluid Mech., 459, 397-428.

Conclusion générale.

Ce travail de thèse a été élaboré dans le but de comprendre le rôle de la concentration en particules, décrite à travers la fraction volumique solide normalisée par sa valeur au packing, dans les processus de sédimentation des suspensions liquide-solides statiques ou soumises à un écoulement de type 'rupture de barrage'. L'une des spécificités de ce travail était d'utiliser les techniques de fluidisation pour générer des suspensions homogènes dans un régime de fluidisation stable qui nous a permis de pouvoir caractériser précisément le mélange en début d'expérience et de faire varier ce paramètre ϕ_s/ϕ_{pack} sur une large gamme de valeurs pouvant s'étendre du régime quasi-dilué, obtenu avec les particules de PMMA pour lequel $\phi_s/\phi_{pack} = 0.05$, au régime le plus dense caractérisé par la valeur au packing pour lequel $\phi_s/\phi_{pack} = 1$. L'objectif principal de ce travail consistait à reproduire en laboratoire des expériences inédites de coulées de boues (non-colloïdales) en fin de course, c'est-à-dire se propageant au bord du littoral sur pentes douces et dominées par les processus de sédimentation ; et de courants de turbidité qui se déposent dans les bassins océaniques ou sur les plaines abyssales, c'est-à-dire dans un milieu marin profond pour lequel l'effet de la surface libre devient alors négligeable. Dans ces différents types d'expériences, seules les conditions aux limites se sont distinguées afin de reproduire des écoulements à surface libre (se propageant dans un canal rempli d'air) ou pleinement immergés (dits *en charge*) dans un canal rempli d'eau.

Le dispositif expérimental avait été conçu et construit au préalable à cet effet, tandis que ce travail nous a permis de réaliser les expériences souhaitées, à l'échelle du laboratoire, en utilisant différents types de matériaux synthétiques (billes de verre de différentes tailles, billes de PMMA de différente densité) et des matériaux naturels (sable fin) de distribution granulométrique variable et de forme différente. La sélection de ces différents matériaux nous a permis de faire principalement varier le diamètre des grains d_p et leur densité ρ_p. Dans les expériences, les propriétés du fluide (sa densité ρ_f et sa viscosité μ_f) ont également été étudiées, mais sur une gamme de valeurs restreinte, simplement en doublant sa température, ce qui nous a poussé à comparer certaines données expérimentales (réalisées sur les suspensions statiques) avec des expériences similaires

réalisées avec différents matériaux (cendres volcaniques, catalyseurs chimiques FCCs) et de l'air (dont la masse volumique et la viscosité sont respectivement de trois et deux ordres de grandeur plus faible que celle de l'eau), issues de travaux antérieurs (Girolami, 2008). Les suspensions de particules reproduites dans les expériences présentées dans ce manuscrit sont considérées comme homogènes, c'est-à-dire associées au régime de fluidisation particulaire obtenu pour une vitesse de fluidisation comprise entre U_{mf} et U_{mb}, ce qui permet de décrire le comportement global des suspensions à partir de grandeurs moyennes caractérisant le mélange (ρ_m, μ_m). Après analyse dimensionnelle, nous avons montré que la sédimentation des suspensions dépend de quatre groupes adimensionnels : ϕ_s, ϕ_s/ϕ_{pack}, $\mathcal{R}e$, $\mathcal{S}t_0$. Lorsque le nombre de Reynolds est faible ($\mathcal{R}e \simeq 1$), ce qui est le cas pour les processus de sédimentation étudiés dans les suspensions statiques ou en écoulement, le problème ne dépend plus que de ϕ_s, ϕ_s/ϕ_{pack}, et $\mathcal{S}t_0$.

En faisant varier ces trois groupes adimensionnels sur une large gamme de valeurs (aussi large que possible), nous avons pu obtenir une loi de comportement unique permettant de décrire l'ensemble des expériences routinières de fluidisation et de sédimentation réalisées avec les différents types de matériaux et de fluide (liquide et gaz) faisant intervenir ces trois paramètres sous forme de trois fonctions indépendantes. L'analyse physique des résultats nous indique que la vitesse moyenne de sédimentation des particules (ou de fluidisation) dans une suspension homogène peut être obtenue à partir de la vitesse théorique d'une particule isolée se déposant dans un fluide pur au repos, à laquelle on doit appliquer une correction en densité (qui affecte la force de flottabilité agissant sur la particule) et une correction en viscosité (qui affecte la force de trainée agissant sur la particule ainsi que sur son agitation locale par rapport à celle du fluide). Ce modèle physique revient à décrire la chute d'une particule dans un fluide équivalent homogène, dont les propriétés sont semblables à celle du mélange.

À l'aide d'expériences consistant à relâcher une sphère macroscopique de diamètre D variable dans une suspension composée de particules microscopiques de diamètre d variable, nous avons souhaité savoir si la viscosité du mélange décrite à partir de la vitesse

de fluidisation/sédimentation déterminée précédemment (qui représente la viscosité vue par les particules composant la phase dispersée) pouvait s'extrapoler à l'échelle de la suspension. Les résultats obtenus n'ont finalement pas apporté d'information pertinente sur la rhéologie du mélange mais nous ont permis de montrer que la force de trainée exercée sur la sphère plongeante (déduite des mesures du coefficient) s'exprime par le produit de la surface de la sphère avec la viscosité du mélange telle que nous l'avons définie à l'échelle d et son taux de déformation proportionnel à U/d. En d'autres termes, même si l'écoulement du mélange autour de la sphère se développe à l'échelle D, seule une fine couche d'épaisseur d (coincée entre la surface de la sphère et la particule la plus proche), fortement cisalllée, est responsable de la trainée exercée sur la sphère qui est contrôlée par la viscosité locale du mélange.

Après avoir décrit en détail les propriétés des suspensions statiques générées dans le réservoir, nous avons exploré leur comportement de transport et de sédimentation lorsque celles-ci sont relâchées dans un canal horizontal sur lequel elles s'écoulent et sédimentent progressivement jusqu'à leur arrêt. En fonction des conditions aux limites choisies dans les expériences, les écoulements générés sont dits à surface libre ou pleinement immergés et ont pour objectif d'obtenir une meilleure compréhension de certains événements naturels extrêmes, comme les coulées de boue et les avalanches sous-marines en fin de course. Pour cette étape, le dispositif a du être adapté et équipé d'un déversoir capable d'expulser instantannément la colonne d'eau formée à la surface de la suspension, notamment pour le cas des écoulements à surface libre. Ces expériences inédites ont pu être décrites en détail et ont montré que la concentration en particules tend à diminuer la mobilité du mélange, en diminuant notamment la distance parcourue, le temps de parcours, la vitesse moyenne du mélange. Le dépôt laissé par l'écoulement est plus épais et plus court lorsque la concentration en particules est élevée, ce qui peut s'expliquer notamment par une sédimentation plus rapide du mélange. Comme pour les écoulements analogues générés avec des particules solides et de l'air, le temps de runout est contrôlé par le temps de fluidisation/sédimentation décrit à partir d'une vitesse et d'une longueur de sédimentation

caractéristique. Dans le cas des écoulements immergés, une couche de mélange diluée se forme à la surface de la suspension et devient rapidement indépendante de l'écoulement sous-jacent. Son temps de propagation est contrôlé par le temps de chute des particules dans le fluide au repos. L'analyse des expériences devront néanmoins être approfondies afin d'en extraire un modèle quantitatif.